SPATIALLY COHERENT SPECTRAL LOCALIZATION

AND

QUANTITATIVE PROBABILISTIC PETROLEUM SYSTEM ANALYSIS

A Dissertation

by

ADEWALE MOROOF AMOSU

Submitted to the Graduate and Professional School of
Texas A&M University
in partial fulfillment of the requirements for the degree of

DOCTOR OF PHILOSOPHY

Chair of Committee,	Yuefeng Sun
Committee Members,	Mark Everett
	Michael Pope
	Eduardo Gildin
Head of Department,	Julie Newman

December 2021

Major Subject: Geology

ABSTRACT

The Fourier transform generates a time-averaged amplitude spectrum of time series; seismic data however is non-stationary, i.e., the frequency content of seismic data changes with time and depth. Spectral decomposition is an essential tool in seismic exploration for analyzing seismic data. Modern spectral decomposition methods such as the Short-Time Fourier Transform, the Continuous Wavelet Transform, and the S-transform address the non-stationary nature of seismic data. The above-mentioned common spectral decomposition methods are however inadequate for certain high-resolution seismic interpretation purposes. In addition, the above methods are performed on individual traces and do not take into account the continuous nature of geological structures or significant events of interest.

The first part of this dissertation presents and describes a new method called the Auxiliary S-transform. The Auxiliary S-transform is an invertible spectral decomposition method designed to significantly improve on the resolution of the S-transform by making use of the multi-dimensional nature of seismic data as well as the separation of seismic events in slowness coordinates. Multi-trace information is utilized with seismic processing techniques such as the linear Radon transform and the parabolic Radon transform. The linear Radon transform and the parabolic Radon transform are ideal for separating seismic events and extracting coherency information because they intrinsically take into account the velocity and curvature of seismic events. The workflow transforms data into the time-frequency-slowness or time-frequency-curvature domain where seismic events are better separated and the coherency attribute is more easily accessible. A filter can be applied in this domain to remove unwanted noise and further enhance the separation between events, to improve the temporal resolution of the method.

The Auxiliary S-transform is applied to synthetic data and its performance is compared to that of the S-transform. It is also applied to real seismic data for a shallow hydrocarbon environment. The results demonstrate that the Auxiliary S-transform has superior temporal resolution at all frequencies compared to the S-transform. The results also demonstrate that the Auxiliary S-transform

is suitable for imaging the lateral continuity of seismic events and geological structures compared to the S-transform.

The second part of this dissertation presents a new quantitative approach for estimating the critical moment in a petroleum system. The petroleum system concept spans the spatial and temporal extent of all elements and processes required for the generation and preservation of petroleum. The critical moment of a petroleum system is the moment with the highest probability for the generation–migration–accumulation of hydrocarbons. It is an important concept in petroleum exploration risk assessment because the stratigraphic and geographic extents of a petroleum system are determined at the critical moment. In petroleum systems, thermal history data, burial history data, and vitrinite reflectance data may be unavailable, unreliable, or incomplete; this introduces significant uncertainty in the choice of the critical moment. This study presents a quantitative probabilistic framework for estimating the critical moment and quantifying the associated uncertainty in such cases. The quantitative probabilistic framework defines a probabilistic early bound and late bound for the critical moment (which, combined together, is termed the critical range) and then estimates the moment with the highest numerical probability of generation–migration–accumulation. It defines the uncertainty associated with the critical moment as half the absolute value of the critical range. In cases with little ambiguity or duplicity in the timing of petroleum system elements and processes, the critical range converges to one point, which is also the critical moment. The quantitative probabilistic framework introduces consistency to the critical moment estimation problem and quantifies the level of uncertainty in the estimation. This significantly reduces the risk involved in petroleum exploration assessment.

DEDICATION

To my parents, Professor Ademola Amosu and Mrs Iyabode Amosu.

To my son, Adebola Amosu.

ACKNOWLEDGMENTS

My profound gratitude goes to God for his gift of life, health, and the grace to complete this program.

My special thanks go to my advisor and the chairman of my advising committee, Dr. Yuefeng Sun for his thoughtful direction, constant advice, and financial and material support throughout the PhD program. His depth of thought, perspective, and vast scientific knowledge are inspiring. I will like to thank the members of my advising committee members, Dr. Mark Everett, Dr. Michael Pope, and Dr. Eduardo Gildin, for giving valuable direction and suggestions, and recommendations to improve this work.

I am grateful to the Texas A&M Berg-Hughes center for financial and research support. I will like to thank the United States Geological Survey, Ikon Geoscience, dGB Earth Sciences and the Netherlands government for providing various software and data. I am indebted to all past and current members of the Reservoir Geophysics Program at Texas A&M University who have all provided priceless assistance to me in many aspects of my studies and life.

Finally, I want to thank my wife and my family for their unending love and support.

NOMENCLATURE

AST	Auxiliary S-transform
AU	Assessment Unit
CWT	Continuous Wavelet Transform
DFT	Discrete Fourier Transform
FFT	Fast Fourier Transform
FWHM	Full Temporal Width at Half Maximum
LFS	Low-Frequency Shadow
LRT	Linear Radon Transform
PCF	Percentile Coherency Filter
PRT	Parabolic Radon Transform
ST	S-transform
STFT	Short Time Fourier transform
TPS	Total Petroleum System

The abbreviations are primarily used in figure labeling.

TABLE OF CONTENTS

Page

LIST OF FIGURES

FIGURE Page

LIST OF TABLES

TABLE Page

1. INTRODUCTION TO SPECTRAL ANALYSIS

Seismic data contains more information than is directly observable in the time/depth domain. To obtain a better understanding of the Earth's subsurface it is necessary to simultaneously examine the temporal and frequency content of seismic data using spectral decomposition. Spectral decomposition transforms seismic data into the time-frequency domain to reveal geophysical responses and structural and stratigraphic details of subsurface rocks, which preferentially appear at specific frequencies. Commonly used spectral decomposition methods such as the Continuous Wavelet Transform and the S-transform are inadequate for some high-resolution seismic interpretation purposes such as tracking thin lateral hydrocarbon layers, and stratigraphic interpretation. Coherency-based spectral decomposition methods represent a novel approach in addressing this problem. These methods simultaneously utilize information from multiple traces in the spectral decomposition process. The objective of the first part of this dissertation is to introduce and present such a new method: the Auxiliary S-transform, examine its properties, evaluate its effectiveness and demonstrate its improved resolution as compared to conventional methods.

1.1 Statement and Significance of Problem

The Fourier transform generates a time-averaged amplitude spectrum of a time series in the frequency domain. The time-averaged amplitude spectrum, however, is inadequate for tracking changes in non-stationary time series. Non-stationary time series are those for which the frequency content changes with time. Fourier analysis decomposes signals into terms of sines and cosine at predetermined frequencies. It can also be viewed as a projection of infinite sinusoidal bases on the signal i.e. it changes the delta bases function of the signal in the time domain to infinite sinusoidal bases in the frequency domain.

There are some intrinsic problems with the Fourier transform:

1. The Fourier transform cannot estimate fractional frequencies instead, it spreads the spectrum to other frequencies.

2. The time averaging nature of the Fourier transform makes it inadequate for analyzing non-stationary signals and lastly.

3. Short-duration signals do not appear noticeable in the amplitude spectrum of a superimposed signal.

Figure 1.1 illustrates examples of (a) stationary and (c) non-stationary signals and their amplitude spectra (b and d respectively). The time series in Figure 1.1a is constructed by superimposing a 10 Hz time series and a 16 Hz time series. The frequency of the time series in Figure 1.1b on the other hand, changes from 10 Hz for the first half of the time series to 16 Hz in the second half, hence it is non-stationary. It is difficult to deduce information about a particular frequency component from the Fourier amplitude spectrum of the non-stationary signal. Figures 1.1e and f show a short duration 40 Hz signal superimposed on a longer duration 10 Hz signal and the corresponding Fourier spectrum. The short duration high-frequency signal is barely visible in the frequency domain and does not have good energy concentration. Time-frequency analysis addresses these problems.

To adequately capture the time variation of non-stationary signals and to address other inadequacies of the Fourier transform, time-frequency analysis was introduced. The Short Time Fourier Transform (STFT) is one of the earlier developed time-frequency analysis methods. In the STFT process, the time series is multiplied with a series of shifted time windows of constant window size, and then the Fourier transform of the multiplied signal is calculated. The choice of window size ensures that the windowed signal segment behaves as if it were stationary. The localizing window is shifted along the entire length of the time series and the localized spectrum is calculated. The resulting time-frequency map is called a spectrogram (Cohen, 1995). The problem with this approach is that the choice of window size significantly affects the resulting decomposed spectrum. The window has to be short enough to effectively isolate temporal signals from a specific layer without impinging on nearby signals. At the same time, shortening the windows reduces the frequency resolution and can distort the spectral characteristics. A wrong window size could result in frequency smearing. This is a fundamental problem in time-frequency analysis affecting methods

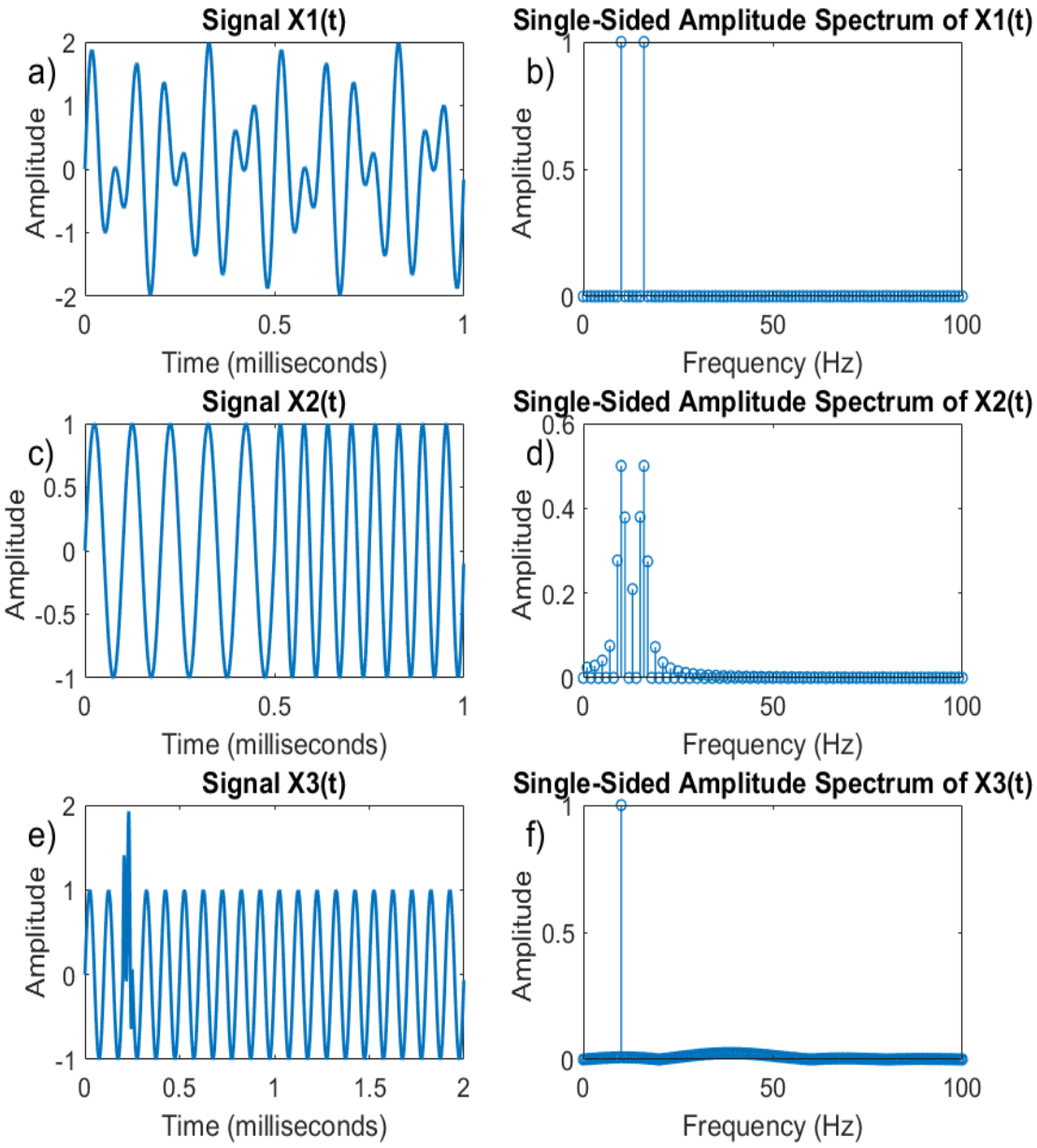

Figure 1.1: a) A time series generated by summing a 10 Hz time series with a 20 Hz time series, c) A time series with a frequency of 10Hz for the first 500 sample points and a frequency of 20 Hz for the next 500 sample points. e) A time series of a short duration 40 Hz signal superimposed on a longer duration 10 Hz signal. b), d) and f) show the respective Fourier transforms of the three signals in a), c) and e) .

that utilize windowing; the trade off between temporal resolution and frequency resolution. This relationship is described by the Heisenberg-Gabor uncertainty principle and is expressed as:

$$\Delta t \cdot \Delta f > C_w \tag{1.1}$$

In equation 1.1, Δt is the time resolution, Δf is the frequency resolution and C_w is a constant that depends on the type of window used. Figure 1.2 illustrates the Heisenberg-Gabor uncertainty principle. Figure 1.3 illustrates the effect of window size on the Short Time Fourier Transform. Temporal resolution refers to how well a transform can capture the rapid variations in a time series in the time domain and frequency resolution refers to how well the changes in the frequencies of a signal can be tracked. Both temporal and frequency resolutions are directly controlled by the choice of window width in Fourier-based time-frequency analysis methods. The temporal resolution is proportional to the length of the windowing function while the frequency resolution is proportional to the frequency range of the windowing function. Hence a short window results in better temporal resolution whereas a wider window results in better frequency resolution.

Some commonly used time-frequency analysis methods focus on modifying the shape of the window or wavelet used. Two of these methods that attempt to capture the time variation are the continuous wavelet transform (CWT) and the S-transform. The continuous wavelet transform is defined as the sum over all time of the time series multiplied by a scaled and shifted version of an analyzing wavelet function. Mathematically, it is defined as the inner product of a family of wavelets with the time series. The continuous wavelet transform is represented as a time scale plot, which is often converted to a time-frequency plot since the scale is inversely related to frequency. The main purpose of using the mother wavelet is to provide a source function to generate the daughter wavelets (Miao and Cheadle, 1998) which are simply the translated and scaled versions of the mother wavelet (Miao and Moon, 1994). The S-transform can conceptually be viewed as a hybrid of short time Fourier analysis and wavelet analysis. The S-transform uses a frequency-dependent window; the standard deviation in S-transform is a function of frequency. As the width of the window is dictated by the frequency, it is apparent that the window is wider in the time

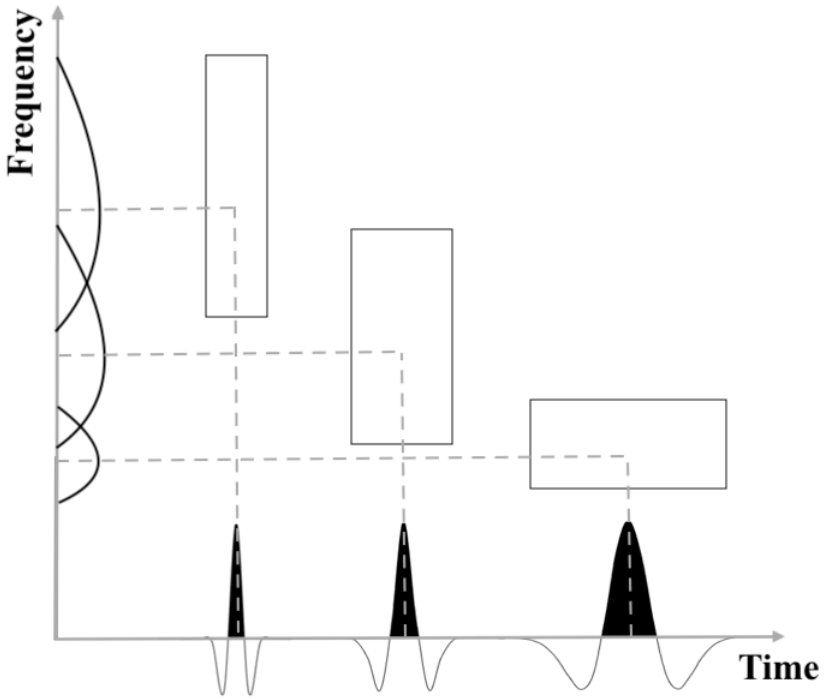

Figure 1.2: The Heisenberg-Gabor uncertainty principle of time and frequency resolution.

domain at lower frequencies which means the window provides good localization in the frequency domain for low frequencies (Stockwell et al., 1996; Stockwell, 2007).

However, despite better performance than the STFT and the CWT, the S-transform may not have sufficient resolution for certain applications and situations. Figure 1.4 shows a synthetic seismic section generated from a stratigraphic impedance model by convolving it with a 50Hz wavelet. The synthetic seismic section contains a thin layer between two thick layers. The spectrally decomposed panel is obtained using the S-transform. It shows that that the S-transform cannot sufficiently temporally resolve the thin layer. The Auxiliary S-transform is designed to be able to address problems of this nature and improve on the temporal localization of seismic events. The resolution provided by the Auxiliary S-transform improves on the resolution of the S-transform for coherent signals. The coherency is defined using multi-trace techniques such as the slant-stack transform and the parabolic Radon transform. The result is that signals that are more coherent are preferentially resolved in the spectrally-decomposed seismic data. The Auxiliary S-transform also

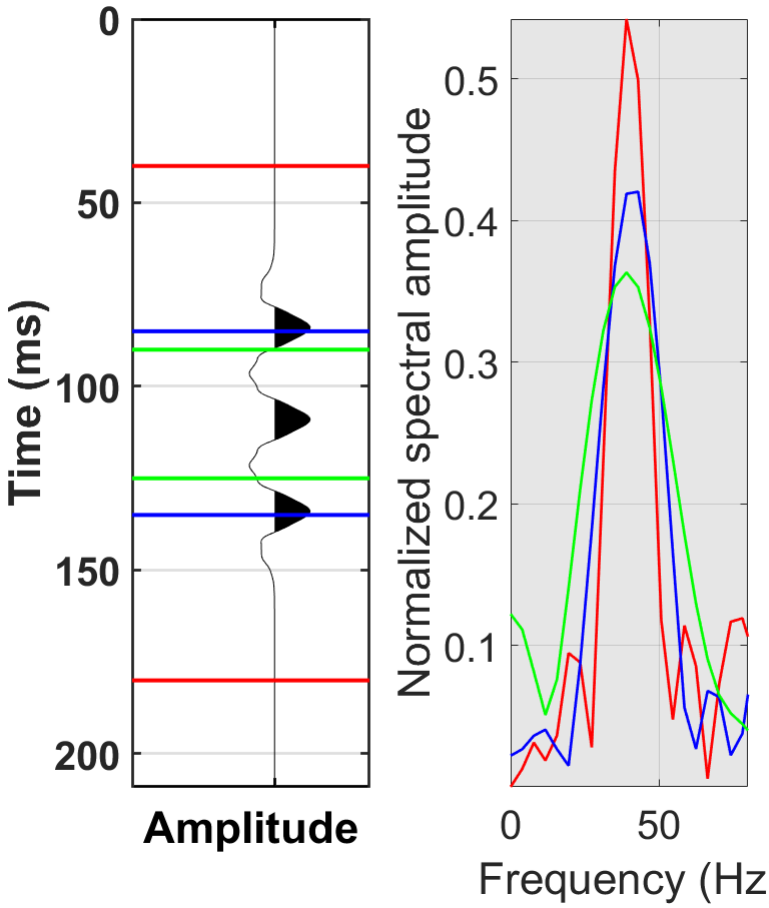

Figure 1.3: Effect of window size on the Short Time Fourier Transform. The wider the window in time, the narrower the frequency width. The STFT is also affected by truncation effects which cause sharp edges.

improves the temporal localization of coherent signals hence it is suitable for high lateral resolution seismic interpretation studies.

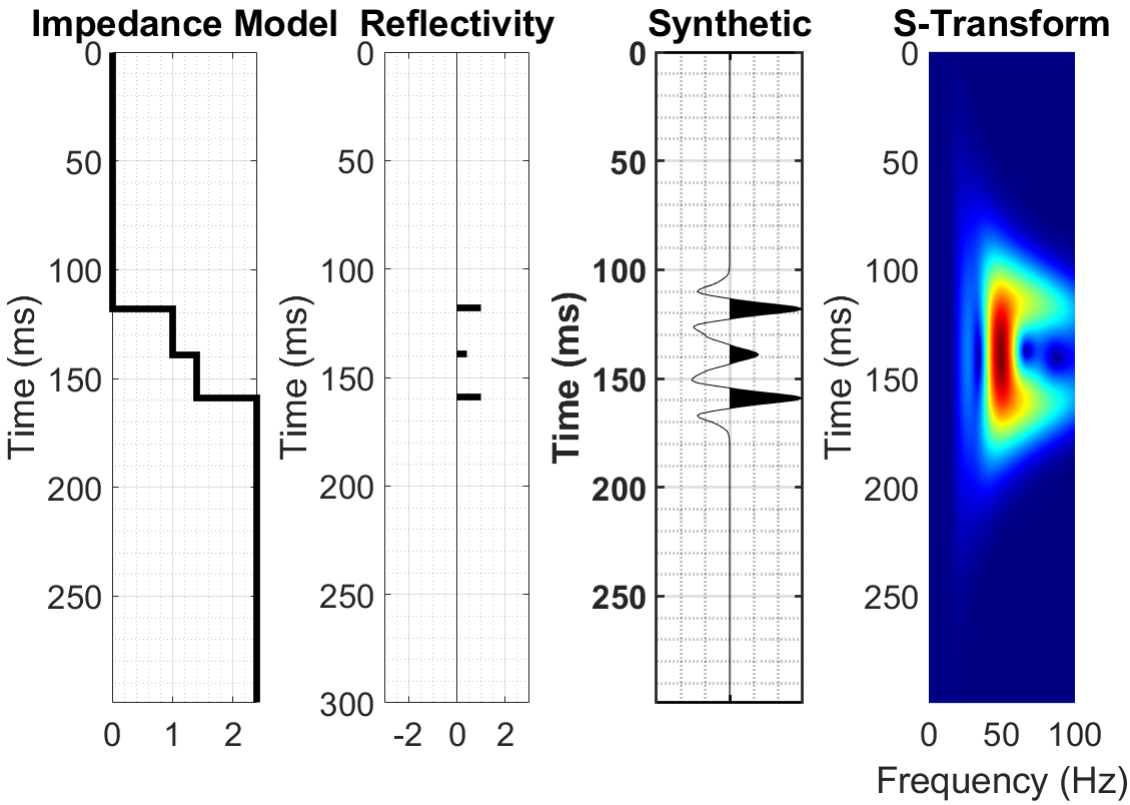

Figure 1.4: S-transform of a thin layer contained within a thicker even layer pair. The S-transform is unable to resolve the thin layer.

1.2 A Compact History of Spectral Analysis

The early history of spectral theory can be traced back to the Greek philosopher, Pythagoras (about 570 – 495 B.C.), who studied wave phenomena using strings in an attempt to establish the laws of musical harmony (Dampier, 1961). In 1672, Sir Isaac Newton (1642-1727) conducted a famous experiment where he split light from the sun into a band of colors using a prism (Newton, 1704). In the 19th century, Robert Wilhelm Bunsen (1811-1899) repeated Newton's experiment using a burning rag soaked in a sodium chloride solution (Bunsen and Roscoe, 1863). The spectrum revealed narrow lines including a bright yellow one which is the spectrum of table salt. Together with Gustav Robert Kirchhoff (1824-1887), Bunsen determined that every chemical element has a characteristic spectrum, however, the spectral theory of the elements could not be explained by classical physics. The theory would later be explained by developments in quantum physics.

In the 17th century, it was assumed that any mathematical function describing physical phenomena was differentiable. Brook Taylor (1685-1731) introduced the concept of the analytic function and developed the Taylor series (Taylor, 1715). The Taylor series, given in equation (1.2), expands analytic functions as an infinite summation of the successive derivatives of the function at a point and makes it possible to uniquely determine the shape of a function at a finite distance from the point around which the function is expanded.

$$f(a+h) = f(a) + \frac{1}{1!}f^{'}(a)h + \frac{1}{2!}f^{''}(a)h^2 + ... \tag{1.2}$$

Taylor's series was in discordance with the work of Daniel Bernoulli (1700-1782). Bernoulli along with other scientists, Jean le Rond d'Alembert (1717-1783), Leonhard Euler(1707-1783), and Joseph-Louis Lagrange (1736-1813) worked on the solution to the wave equation (d'Alembert, 1747; Euler, 1755; Lagrange, 1759; Euler, 1766). The development of the wave equation was inspired by the Pythagoras' above-mentioned studies. The wave equation is given as:

$$\frac{\partial^2 u}{\partial^2 x} - \frac{1}{c^2}\frac{\partial^2 u}{\partial^2 t} = 0 \tag{1.3}$$

where u is the displacement, x is the horizontal coordinate, t is time and c is the velocity of the traveling waves on a string.

Bernoulli introduced the method of separation of variables and claimed that the general solution to the wave equation was an infinite sum of sine and cosine functions i.e. an arbitrary non-analytic function could be expressed as an infinite sum of analytic functions (Bernoulli, 1738). In 1807, Jean Baptiste Joseph de Fourier (1768-1830) proposed the Fourier series to the French Academy (Fourier, 1822). He made the claim that an arbitrary function defined over a finite interval by a rough or even discontinuous graph could be represented by an infinite sum of cosine and sine functions. The Fourier series was also at odds with the Taylor series at the time.

It is worthy of note that in 1891, Albert Abraham Michelson (1852-1931) developed an interferometer, a device that merges two or more sources of light to create an interference pattern, which can be measured and analyzed (Michelson, 1891). He conducted a series of experiments and was able to calculate the autocovariance of the original signal and with a mechanical harmonic analyzer, the Fourier transform of the visibility curve.

The discrepancy between the Bernoulli's solution, the Fourier series, and Taylor series is bridged by the z-transform, the fundamental theory of digital signal processing. The z-transform (Ragazzini and Zadeh, 1952), expands an analytic function $f(z)$ around the point $z^{-1} = 0$ as given by equation (1.4).

$$f(z) = \sum_{n=0}^{\infty} a_n z^{-n} \tag{1.4}$$

For points on a unit circle the Taylor expansion for $f(z)$ is:

$$f(z) = f(e^{i\theta}) = \sum_{n=0}^{\infty} a_n (cosn\theta - isin\theta) \tag{1.5}$$

which is the form of the complex Fourier series in the angle θ. The convergence of the Taylor series on the unit circle is exactly the convergence of the Fourier series; hence the z-transform reconciles the two theories (Robinson, 1967).

Following the success of the Fourier series, its properties were further developed and consequently, any expansion in terms of orthogonal functions is referred to as a Fourier series. Other theories were developed. Charles Sturm (1803-1855) and Joseph Liouville (1809-1882) developed the Sturm-Liouville theory of differential equations (Sturm, 1836; Liouville, 1838). The Sturm-Liouville theory is the foundation of the spectral theory of differential equations; it reveals the eigenfunctions of the Helmholtz equation (the time-independent form of the wave equation) as sines and cosines corresponding to the Fourier series.

In an important breakthrough in quantum physics, Erwin Schrödinger (1887-1961), developed the Schrödinger spectral theory of atoms in which he demonstrated the connection between vibrations in atoms and the Sturm-Liouville theory (Schrödinger, 1926; Schrödinger, 1928). The theory explained the discrete spectra observed by Bunsen and Kirchoff. An equivalent matrix mechanics formulation was developed in 1925 by Werner Heisenberg (1907-1976) (Heisenberg, 1930). Quantum mechanics represents the electron by a probability density function and successfully explained the energy state and transition of electrons and the generation of photons.

The next stage in the development of spectral theory was the application of general operators in Hilbert space. Following the work of Heisenberg and Schrödinger, quantum physics briefly faced an abstract mathematical crisis because the quantum mechanics needed could not be adequately formulated within the existing mathematical framework (Robinson, 1967). John von Neumann established the spectral representation of the Hermitian operator and reformulated the eigenvalue problem (the spectrum corresponds to different eigenvalues) into the spectral representation problem with the additional advantage that his solution could be extended to Hilbert space (Neuman, 1929). The Hilbert space (an infinitely dimensional space) was named after David Hilbert (1862-1943). The development was mathematical in nature, but it laid the foundation for further advancement.

In 1827, A botanist, Robert Brown (1773-1858) described a kinetic phenomenon known as Brownian motion (Brown, 1827). He found that minute particles of solid matter when suspended in pure water exhibit irregular zigzag movement. Marian von Smoluchoski (1872-1917) and Albert

Einstein (1879-1955) developed the physical theory of Brownian motion (Einstein, 1906; Smoluchowski, 1914) while Norbert Wiener (1894-1964) developed its mathematical theory (Wiener, 1923). Their studies showed that the Fourier transform of a white noise process in time was a white noise process in frequency.

In 1898, Sir Arthur Schuster (1851-1934) introduced the periodogram for spectrum analysis of empirical time series (Schuster, 1898). Many empirical time series observed in nature, however, did not yield periodograms with dominant peaks. George Udny Yule (1871-1951) introduced the autoregressive spectrum estimation method which gives the power spectrum, amplitude, and phase spectrum of a time series (Yule, 1927). Wiener in 1930 published "Generalized Harmonic Analysis" (Wiener, 1930). He obtained the precise relationship between the autocovariance function and the power spectrum. He showed how to take the Fourier transform of a stationary random process. Wiener's spectral theories and von Neumann's spectral theories find common ground in the Hilbert space by the Cayley transform (Cayley, 1846). Wiener also contributed to the Weiner-Levinson prediction theory for predicting the future value of a stationary discrete-time stochastic process (Levinson, 1947; Wiener, 1949).

John Wilder Tukey (1915-2000) in a symposium paper in 1949 showed how to compute the power spectra from empirical data and laid the statistical foundation for the analysis of a short-time series. In 1951, Tukey's spectra was computed for various sections of Mobil seismic records by Enders Robinson (Robinson, 1967). A seismic analysis method based on Wiener's prediction theory was then successfully used in digital deconvolution for the first time. This success led to the establishment of the MIT Geophysical Analysis Group with ties to the oil industry, in 1952. From 1952 to 1957 the MIT Whirlwind digital computer (Figure 1.5) was used to analyze seismic records. Tukey's method for estimating coherence (sometimes called semblance) is vital in the estimation of seismic velocity as in other multi-trace methods. In 1965, James William Cooley (1926–2016) and Tukey published the Fast Fourier Transform (FFT; Cooley and Tukey, 1965). Their paper described an algorithm for the discrete Fourier transform. The algorithm meant spectral quantities could be computed an order of magnitude faster. The Fast Fourier Transform (FFT)

is a fast algorithm for calculating the discrete Fourier transform. Evaluating the discrete Fourier transform directly requires operations of order (N^2), however, an FFT can compute the same results in operations of order $(NlogN)$. The FFT function automatically places some restrictions on the time series to be evaluated in order to generate a meaningful, accurate frequency response. Because the FFT function uses a base 2 logarithm by definition, it requires that the range or length of the time series to be evaluated contains a total number of data points precisely equal to a 2-to-the-nth-power number (e.g., 512, 1024, 2048, etc.). The existence of the FFT meant that spectral analysis could be performed rapidly.

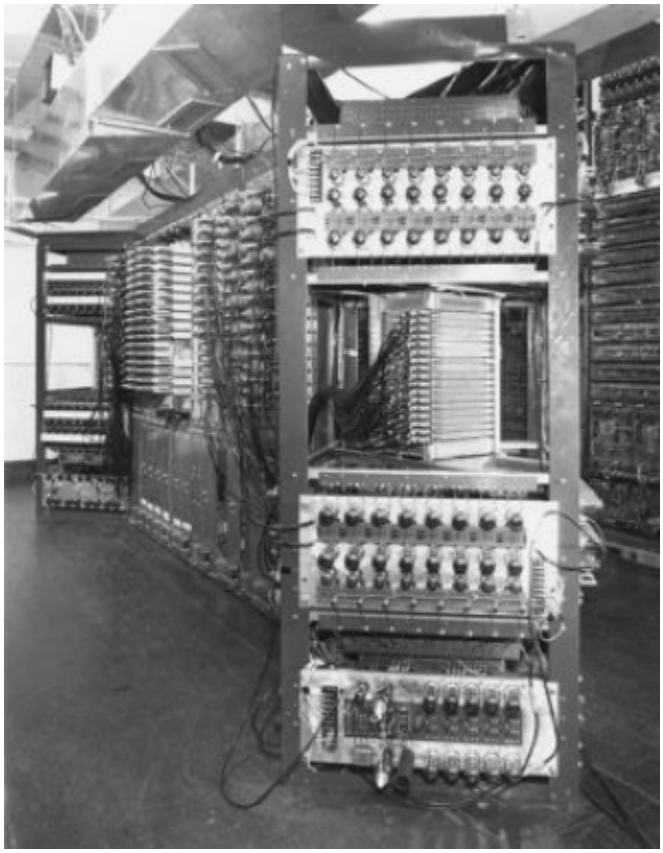

Figure 1.5: Memory bank in the MIT Whirlwind computer (1953). Banks of magnetic-core assemblies replace electrostatic tube memory. The Whirlwind was the first computer used for digital seismic analysis. Picture reproduced with the permission of The MITRE Corporation.

In the late 1950s, transistors were introduced to replace bulky vacuum tubes in digital computers; this led to a digital revolution. The Whirlwind computer, developed at MIT, was the first real-time high-speed digital computer using random-access magnetic-core memory which replaced electrostatic storage tubes. The success of this computer led to the United States Air Force's Semi Automatic Ground Environment (SAGE) system, which centralized the control of multiple radar stations. On September 12, 1958, Jack Kilby (1923-2005) at Texas Instruments demonstrated the first working example of a hybrid integrated circuit germanium chip; he submitted a patent application of the device on February 6, 1959 (Kilby, 1964). Jack Kilby won the 2000 Nobel prize in physics for his contribution to the invention (Alferov et al., 2000). The first monolithic integrated circuit silicon chip was invented by Robert Noyce at Fairchild Semiconductor (Noyce, 1977). The number of transistors per unit area in integrated circuits doubled every 2 years over several decades. This is known as Moore's Law, named after Gordon Moore (Moore, 1965; Moore, 1975). Intel released the first microprocessor, the Intel P4004 microprocessor, in 1969. The development of the microprocessor meant thousands of integrated circuits could be placed onto a single silicon chip and a single chip could now contain all of the components of a computer. The invention of the integrated circuit and microprocessor led to a universal digital revolution of epic proportions including the development of home computers from the mid-1970s.

The seismic industry converted to digital technology in the early 1960s. Since then nearly every seismic record in oil and gas exploration has been digitally processed. This led to the discovery of giant oil fields including offshore discoveries like the North Sea, the Gulf of Mexico, the Persian Gulf, and onshore discoveries in Alaska, Asia, Africa, South America, and the Middle East (which would not otherwise have been found by analog methods); in 1951, it took a whole summer to process 32 traces (Robinson, 1982). Today with improved microprocessors and new computing developments like parallel processing, millions of traces can now be processed in a few seconds.

Several studies had considered the classical problem of estimating time series from limited information about its autocovariance function. In 1967, John Parker Burg introduced the maximum entropy spectral analysis method that obtained power spectrum from a measured autocovariance

function using nonzero estimates at all lags (Burg, 1967). The method obtains an estimate of the power spectrum by maximizing the spectral entropy with the known autocorrelation values as constraints. It requires the computation of the minimum phase deconvolution operator or prediction error filter. The power spectrum is then obtained as the square inverse of the Fourier transform of the operator, which mathematically, is the inverse of a finite trigonometric series.

Following the work of Burg, other important developments occurred in spectral analysis. Itakura and Saito (1968) introduced maximum likelihood in spectrum estimation. Parzen (1974) introduced the Parzen window for spectral analysis. Parzen (1974) and Akaike (1969, 1974) further developed autoregressive spectrum estimation and autoregressive order-determining criteria which made possible the widespread application of autoregressive spectrum estimation in diverse fields (Robinson, 1982).

1.3 Modern Spectral Analysis

In recent years, developments in spectral analysis have focused on addressing the non-stationary nature of some time series. The short-time Fourier transform (STFT) where time-frequency resolution is fixed over the entire time-frequency space by preselecting a window length, initially introduced by Gabor (1946) was discussed by Cohen (1995). The continuous wavelet transform (CWT) which produces a time-scale map called a scalogram instead of a time-frequency spectrum was discussed by Daubechies (1992). The scalogram was converted to a time-frequency map by taking the scale to be inversely proportional to the center frequency of the wavelet by Hlawatsch and Boudreaux-Bartels (1992). The S-transform was introduced by Stockwell et al. (1996). The S-transform is an invertible time-frequency spectral localization technique that combines elements of wavelet transforms and the STFT. Time-frequency is discussed in more detail in the second chapter. Table (1.1) gives a summary of the major events in the timeline of spectral analysis.

Table 1.1: Major Events in the Timeline of Spectral Theory

Year and Scientist	**Work**
Circa 570 B.C. Pythagoras of Samos (570-495 BC)	Development of the calendar and the clock; studied the laws of musical harmony.
1704 Isaac Newton (1642-1727)	Empirical discovery of spectra using the glass prism to split rays of the sun.
1715 Brook Taylor (1685-1731)	Introduced the concept of the analytical function. Taylor series expanded an analytical function into an infinite summation of component functions.
1738 Daniel Bernoulli (1700-1782)	Demonstrated that non analytic function can be expressed as a sum of analytic functions.
1746 Jean le Rond d'Almbert (1717-1783)	1D Wave Equation.
1755 Leonhard Euler (1707-1783)	3D Wave Equation. Solved for coefficients of the analytic functions that sum to create non analytical functions.
1755 Joseph Louis Lagrange (1736-1813)	Solved for coefficients of the analytic functions that sum to create non analytical functions.
1828 George Green (1793-1841)	Green's function which exhibits impulse response function of a linear system in terms of its spectrum.
1807 John Baptist Joseph de Fourier (1768-1830)	Proposed the Fourier series: any arbitrary function defined over a finite interval by a rough and even discontinuous graph could be represented as an infinite summation of sines and cosines.

continued on the next page

Table 1.1: Major Events in the Timeline of Spectral Theory (continued)

Year and Scientist	**Work**
1830 Charles Sturm (1803-1855) Joseph Liouville (1809-1882)	Spectral theory of differential equations: vibration of infinitely long right circular cylinder can be described as second order differential equation.
1859 Robert Wilhelm Bunsen (1811-1899) Gustav Robert Kirchoff (1824-1887)	Repeated Newton's experiment using a burning rag as a light source. The spectrum exhibited narrow lines, one bright yellow corresponding to sodium.
1896 John Willian Strutt (1842-1919)	Applications of the expansion of functions in terms of orthogonal functions.
1926 Erwin Schroedinger (1887-1961)	Showed vibrations occurring within atoms can understood by means of the Sturm-Liouville theory.
1929 Von Neumann (1903-1957)	Reformulated the Eigen value problem as the spectral representation problem and extended it to Hilbert space (an infinitely dimensional space named after David Hilbert (1862-1943).
1946 Dennis Gabor (1900-1949)	Development of the Short Time Fourier Transform.
1947 John Ralph Ragazzini (1912-1988) Lotfi Aliasker Zadeh (1921-2017)	Z-transform: bridges the gap between Taylor series and Fourier series.
1950 Jack Kilby (1923-2005)	Development of the transistor and integrated circuits.
1951 Enders Robinson	First ever digital analysis of a seismic record on the MIT Whirlwind computer.

continued on the next page

Table 1.1: Major Events in the Timeline of Spectral Theory (continued)

Year and Scientist	**Work**
1969 Intel Corporation	Development of the microprocessor.
1965 John Wilder Tukey (1915-2000) James William Cooley (1926-2016)	Discovery of Fast Fourier Transform, Radix-2 FFT program.
1992 Ingrid Daubechies	Development of the Continuous Wavelet Transform.
1996 Robert Glenn Stockwell	Development of the S-transform.

2. CONVENTIONAL SPECTRAL DECOMPOSITION AND INTEGRAL GEOMETRY TRANSFORMS

2.1 Seismic Interpretation and Spectral Decomposition

The goal of seismic interpretation is to retrieve all subsurface information from the seismic volume. It aims to establish the subsurface rock properties, discover the depositional history, delineate structure and fault networks, establish a stratigraphic framework and identify reservoirs and other features of interest. Seismic waves probe the Earth's internal structure and the energy reflected from subsurface layers gives insight into the subsurface rock properties. Consider a source and a receiver at the same location above a layered Earth model where the layers had different velocities, seismic waves propagating downward will be reflected back to the surface at each interface and recorded by the receiver at specific arrival times as a series of peaks. By repeating this at different closely spaced points along the surface and plotting the peaks as a function of time and distance an image of the subsurface interfaces is produced. This type of seismic image is called a zero-offset section (no source-receiver offset). In reality, the data are recorded at a variety of source-receiver offsets, but the data are processed and combined in a way that removes the offset dependence. This ensures the lateral variability in reflector depth can be properly imaged.

Seismic amplitudes are generated from the interaction of band-limited signals with the local distribution of impedance contrasts. Conventional seismic interpretation relies wholly on the difference in full-bandwidth amplitudes for the interpretation of continuous structures and signals of interest; in doing so, it disregards the narrow band information that is available. The interaction of band-limited signals with local impedance contrasts makes geological features tune in at some frequencies and tune out at other frequencies (Brown, 2011). Spectral decomposition is therefore necessary and effective because it reveals the frequencies at which geological features stand out. It provides greater resolution and detection of layer heterogeneity, layer terminations, and thickness variability than are possible with traditional seismic interpretation.

Spectral analysis was applied in steam-based recovery of bitumen at Cold Lake, Alberta, Canada by Dilay and Eastwood (1995). Peyton et al. (1998) studied an incised valley system by applying spectral decomposition and coherency on 3D seismic data. Spectral decomposition (SD) was used as a seismic interpretation tool by Partyka (1999). The study introduced the use of spectral decomposition in estimating layer thickness. He related the frequency of occurrence of notched spectra to the thickness of certain layers and concluded that the notched spectral could be sometimes be used to infer layer thickness and geological discontinuities. Gabor (1946) introduced the Short Time Fourier Transform (STFT). The STFT, time-frequency resolution is fixed using pre-selected window length. The continuous wavelet transform (CWT) produces a time-scale map called a scalogram (Daubechies, 1992). The scale can be converted to frequency by taking scale as inversely proportional to the center frequency of the wavelet (Hlawatsch and Boudreaux-Bartels, 1992). Stockwell et al. (1996) introduced an invertible time-frequency spectral localization technique called the S-transform as a tool for optimal time-frequency analysis of geophysical signals.

There are numerous geological applications of spectral decomposition. Instantaneous spectral analysis (ISA) was used by Castagna et al. (2003) and Castagna and Sun (2006) in detecting hydrocarbons. They indicated that low-frequency shadows were more apparent in spectrally decomposed data than in seismic sections. Deng et al. (2007) used spectral decomposition techniques to stack seismic sections from a deepwater reservoir. The study showed that gas-associated spectral anomalies occur at both low and high-frequency iso-frequency sections. Reine et al. (2009) used spectral decomposition techniques in measuring seismic attenuation. The study compared several time-frequency transforms and showed that the choice of a fixed or variable window affects the robustness and accuracy of the resulting attenuation measurements. Zhang et al. (2009) propose using multiple spectral components to delineate architectural elements that fall at or below seismic resolution and address depositional patterns. They showed that the peak frequency and mean frequency are stratigraphically sensitive attributes that can characterize vertical changes in sequence packages. Liu et al. (2011) proposed a new method for seismic noise attenuation measurement by applying non-stationary polynomial fitting. They showed that compared with conventional meth-

ods the proposed method can efficiently suppress seismic noise and improve the signal-to-noise ratio. Cichostępski et al. (2019) demonstrated that spectral decomposition can be used for the verification of bright spots in the presence of thin beds. Spectral decomposition is routinely used in identifying channels in seismic data (Gridley and Partyka, 1997; Xiao et al., 2008; Verma et al., 2009; Li et al., 2010; Yoon and Farfour, 2012).

Conventional seismic interpretation is also typically carried out by studying patterns across multiple traces. By studying the overall shape or pattern from multiple traces in vertical or horizontal slices, characteristic shapes and patterns may emerge and be interpreted as a feature of geological significance (Broussard, 1975). For example, Broussard (1975) and Klein (1985) have provided depositional models for interpreting observed depositional features. Mitchum et al. (1977) studied seismic sequences, reflector termination patterns, and characteristic seismic facies which correspond to varied depositional environments. The observed patterns span multiple traces and are used for geological interpretation. The goal of this work is to employ multi-trace interpretation techniques in improving spectral decomposition results.

2.2 Conventional Spectral Decomposition Methods

Fourier analysis decomposes signals into terms of sines and cosine at predetermined frequencies. It can also be viewed as a projection of infinite sinusoidal bases on the signal i.e. it changes the delta bases function of the signal in the time domain to infinite sinusoidal bases in the frequency domain.

The Fourier transform $S(f)$ of a signal $d(t)$ is given as:

$$S(f) = \int_{-\infty}^{\infty} d(t) e^{-i2\pi ft} dt \tag{2.1}$$

The inverse Fourier transform is:

$$d(t) = \int_{-\infty}^{\infty} S(f) e^{i2\pi ft} df \tag{2.2}$$

where t is time, f is frequency, $s(t)$ is the continuous time signal, and $S(f)$ is the continuous complex spectrum.

2.2.1 Short Time Fourier Transform

The Short Time Fourier transform (STFT) derived by Gabor (1946) adds time dependence to the Fourier transform by windowing the signal and then performing the Fourier transform on the windowed data to obtain localized frequency information. The resulting time-frequency map is called a spectrogram (Cohen, 1995). The STFT is given by the inner product of the signal $d(t)$ with a time-shifted window function $\omega(t)$ The STFT is given as:

$$S(\tau, f) = \int_{-\infty}^{\infty} d(t)\omega(t-\tau)e^{-i2\pi ft}dt \tag{2.3}$$

(Gabor, 1946)

The inverse STFT is:

$$d(t) = \int_{-\infty}^{\infty}\int_{-\infty}^{\infty} S(\tau, f)e^{i2\pi ft}d\tau df \tag{2.4}$$

2.2.2 Continuous Wavelet Transform

The continuous wavelet transform (CWT) is defined as the sum over all time of the signal $d(t)$ multiplied by a scaled and shifted version of the analyzing wavelet function. Mathematically, it is defined as the inner product of a family of wavelets with signal $s(t)$. The CWT is defined by Cohen (1995) as;

$$S(a,b) = \int_{-\infty}^{\infty} d(t)\frac{1}{\sqrt{|a|}}W\left(\frac{t-b}{a}\right)dt \tag{2.5}$$

where a is called the dilation parameter or scale and b is called the translation parameter. The main purpose of using the mother wavelet is to provide a source function to generate the daughter wavelets which are simply the translated and scaled versions of the mother wavelet (Mia and Moon, 1994). The wavelet is localized in both time and frequency.

The inverse CWT is:

$$d(t) = \frac{1}{c_W} \int_0^\infty \int_{-\infty}^\infty S(a,b) \frac{1}{\sqrt{a}} W(\frac{t-b}{a}) db \frac{da}{a^2} \tag{2.6}$$

where

$$c_W = \int_0^\infty \frac{|W(\omega)|^2}{\omega} d\omega < \infty$$

CWT is represented as a time scale plot, where scale is the inverse of frequency. At a low scale (high frequency), CWT offers high time resolution and at higher scales (lower frequencies) CWT gives high-frequency resolution.

2.2.3 S-transform

The S-transform (ST) can be viewed as a hybrid of short-time Fourier analysis and wavelet analysis or an extension to the Gabor and Wavelet transforms (Stockwell et al., 1996) and is based on a moving and scalable localizing gaussian window. It is defined as:

$$S(\tau, f) = \int_{-\infty}^\infty d(t) W(\tau - t, \sigma(f)) e^{-i2\pi ft} dt \tag{2.7}$$

where t is time, f is frequency, τ is a parameter that controls the position of the Gaussian window along the time axis and $\int_{-\infty}^\infty W(\tau - t, \sigma(f))dt = 1$

$W(\tau, \sigma(f))$ is the Gaussian window defined as:

$$W(\tau, \sigma(f)) = \frac{1}{\sqrt{2\pi}\sigma(f)} e^{\left(-\frac{\tau^2}{2\sigma^2(f)}\right)}$$

and

$$\sigma(f) = \frac{1}{f}$$

The inverse S-Transform is defined as:

$$d(t) = \int_{-\infty}^{\infty} \left[\int_{-\infty}^{\infty} S(\tau, f) d\tau \right] e^{i2\pi f t} df \tag{2.8}$$

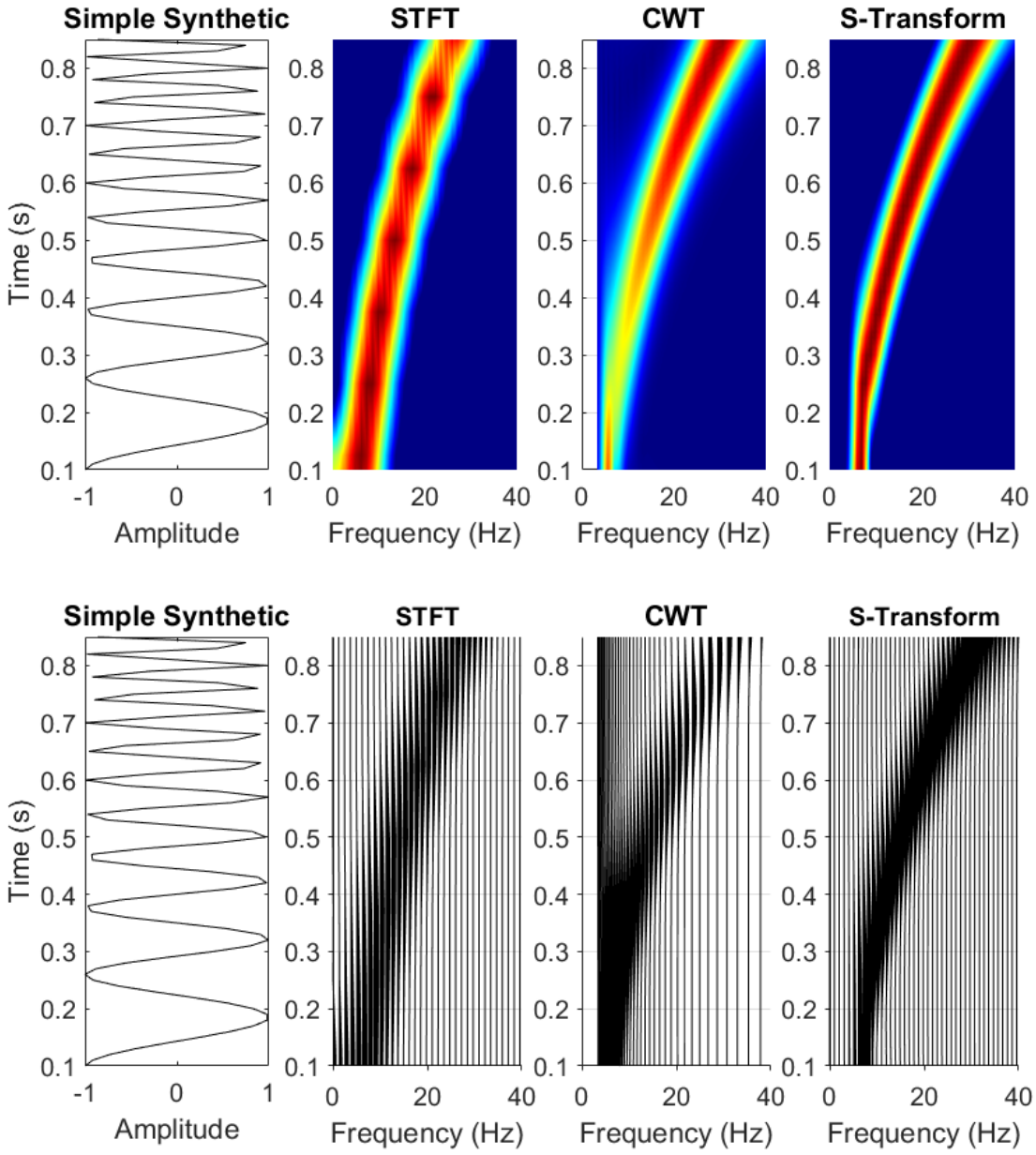

Figure 2.1: Comparison of STFT, CWT, and S-transform for a single simple synthetic chirp with increasing frequency from 5 Hz to 40 Hz.

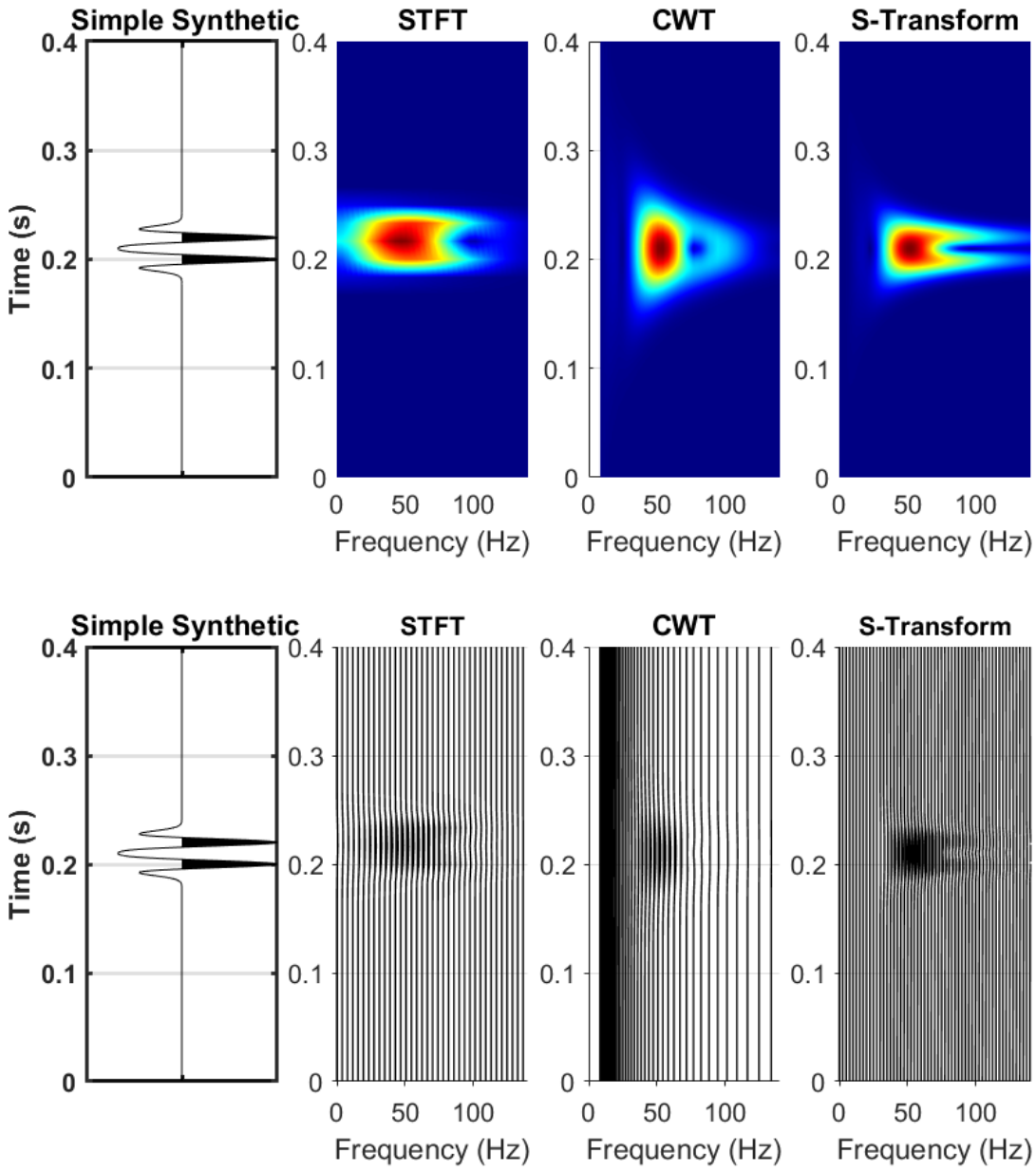

Figure 2.2: Comparison of STFT, CWT, and S-transform for a single simple synthetic trace.

Figures 2.1 and 2.2 compare the performance of the STFT, CWT, and S-transform for a synthetic chirp and a simple synthetic trace with two peaks. In Figure 2.1 both the ST and CWT image widths change as the frequency changes. The ST image is better resolved (narrower) than that of the CWT at low frequencies. Figure 2.2 illustrates the resolution limitations of all three methods. Figure 2.3 demonstrates the forward and inverse S-transform and Figure 2.4 shows single

frequency panels obtained from the S-transform. The S-transform performs better than the STFT and CWT at low frequencies. The S-transform and STFT are both derived from the Fourier transform of the time series multiplied by a time-shift window (Stockwell, 1996). Unlike the STFT, the standard deviation $\sigma(f)$ in the S-transform is a function of frequency making the window function a function of time and frequency. The frequency controls the window width, hence at low frequencies, the window is wide in the time domain and well localized in the frequency domain (Stockwell, 2007).

In both S-transform and CWT, the window size changes with both time and frequency, however, the shapes of the real and imaginary parts of the S-transform wavelet change when the Gaussian window translates in time while the shape of wavelet of CWT is consistent. Consequently, the S-transform combines progressive resolution with absolutely referenced phase information (Stockwell, 2007), hence it could estimate the local amplitude spectrum and the local phase spectrum. The S-transform window is divided into two parts, the slowly varying envelope, the Gaussian function which localizes in time, and the oscillatory exponential kernel $e^{-2\pi ft}$ which selects the frequency being localized. The time localizing Gaussian envelope is translated while the oscillatory exponential kernel, which is provided by the complex Fourier sinusoid, is stationary (Pinnegar and Mansinha, 2003). As a result, the shapes of the real and imaginary parts of the S-transform wavelet change when the Gaussian window translates in time (Pinnegar and Mansinha, 2003). Thus the S-transform independently localizes the phase spectrum as well as the amplitude spectrum. The S-transform is also sampled at the discrete Fourier transform frequencies (Stockwell, 2007). The S-transform, therefore, performs better than the STFT and the CWT however its resolution may still be inadequate for certain interpretation purposes as shown in Figure 2.2; the S-transform is unable to completely resolve the two peaks in time.

The generalized S-transform which permits greater control on the window behavior was introduced by McFadden et al. (1999) and Pinnegar and Mansinha (2003) by replacing the Gaussian in the S-transform with a generic window. The generalized S-transform is given by:

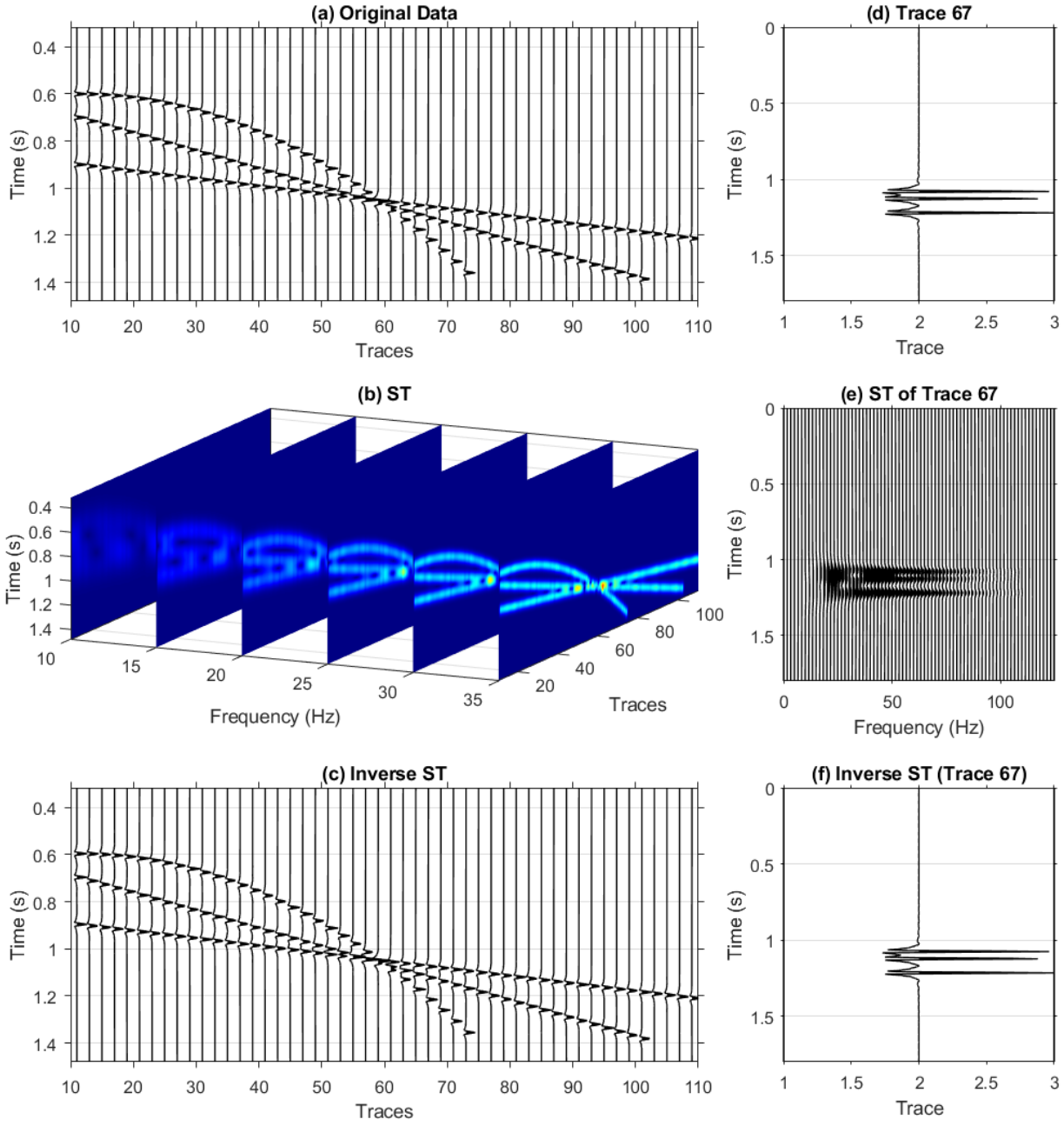

Figure 2.3: Demonstration of the forward and inverse S-transform for three seismic events, one with a parabolic moveout and two with linear moveouts. a) Original data. b) Time-frequency-space volume generated by applying the S-transform. c) Reconstructed data from the inverse S-transform. d) to f) show Traces and sections extracted from a), b) and c).

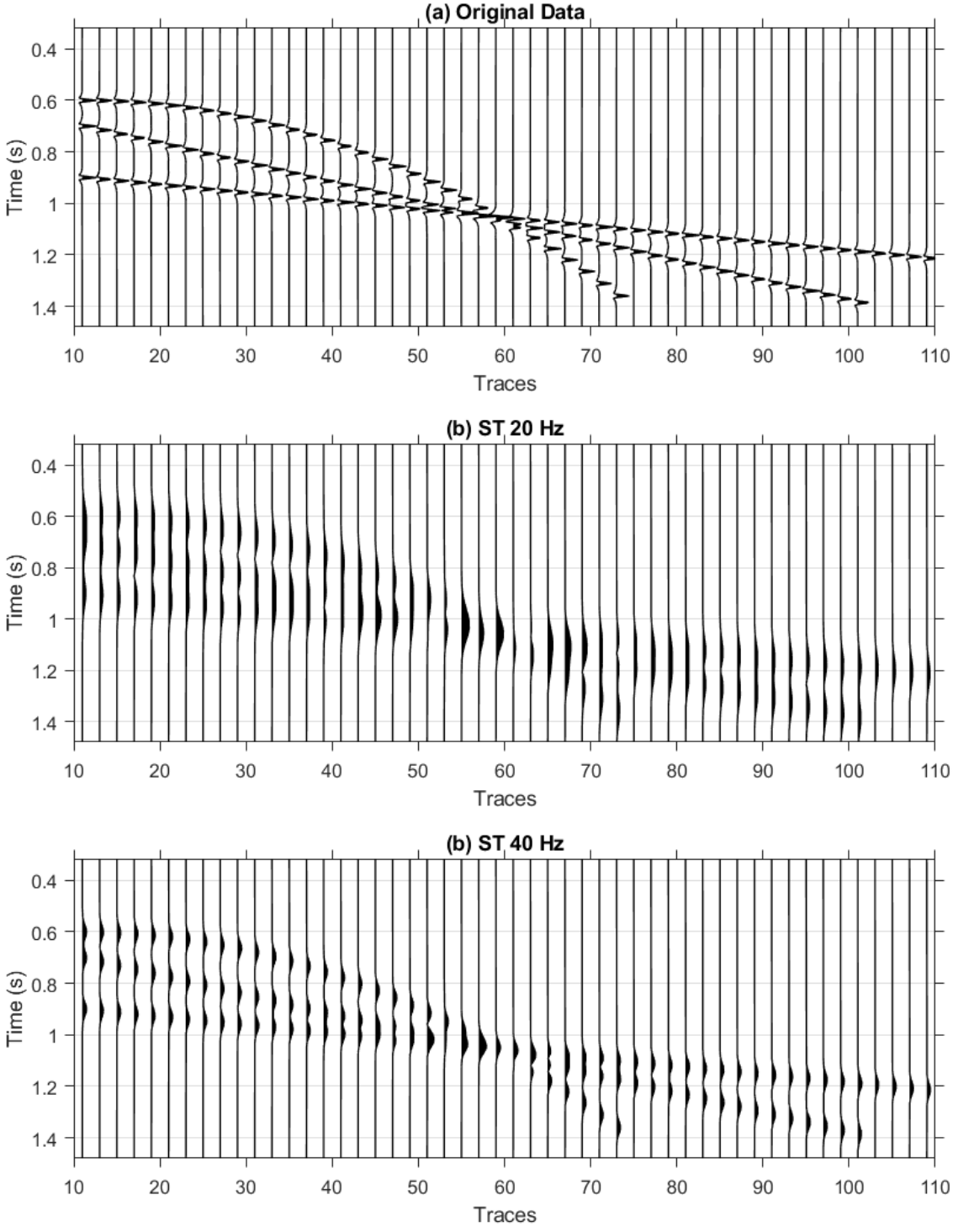

Figure 2.4: Single frequency sections extracted from the ST time-frequency-offset volume for seismic data given in Figure 2.3.

$$S(\tau, f, p) = \int_{-\infty}^{\infty} d(t) w(\tau - t, p) e^{-2\pi i f t} dt \tag{2.9}$$

where w is the window function of the generalized S-transform and p is the set of parameters that determine the shape of the window function.

The window satisfies the condition: $\int_{-\infty}^{\infty} w(\tau - t, f, \beta) d\tau = 1$

2.3 Integral Geometry and the Radon Transform

Integral geometry focuses on the numerical characteristics or measures for sets of points, lines, planes, and other geometrical objects, computed with the aid of integration. The measures must meet the requirements of additivity and invariance to motion. This branch of mathematics was developed to address problems related to geometric probabilities (defined as the ratio of the measure of the set of favorable cases to the measure of the set of all possible cases). The problem is addressed using integral transforms such as the Radon transform and its generalizations . The first and most famous example of this is Buffon's needle problem (Buffon, 1777). The problem seeks to find the probability that a needle of a given length will land on a line, given a floor with equally spaced parallel lines (Buffon, 1777). Applying the Radon transform on the Buffon's needle images at different line densities and calculating the variance for different angles, shows a clear marker for symmetry breaking and loss of randomness (Hart, 2019).

The Radon transform is a natural measure that is invariant to translation, rotation, and scale changes. It maps data to the new domain, where some of its properties can be more easily derived, by integration over hyperplanes (summing elements of the data along selected trajectories). The Radon transform was established in 1917 by Johan Radon (1887-1956) (Radon, 1917). It is a mathematical technique that has been widely used in seismic data processing and image analysis. Deans (1983) and Durrani and Bisset (1984) examined the mathematical theory and fundamental properties of the Radon transform. Many studies have used the Radon transform for multiple attenuation (Hampson, 1986; Bradshaw and Ng, 1987; Kelamis et al.,1990; Kostov, 1990; Foster and Mosher, 1992; Hugonnet and Canadas, 1995; Sacchi and Ulrych, 1995; Cary, 1999; Sacchi

and Porsani, 1999; Trad, 2001; Oppert, 2002).

Three types of Radon transforms have been used in seismic data processing: the slant-stack or $\tau - p$ transform; the parabolic Radon transform and the hyperbolic Radon transform (Trad,2001).

The generalized Radon transform is defined for seismic data as:

$$M(\tau, q) = \int_{-\infty}^{\infty} d(t = \tau + q\phi(q,x), x)dx$$

where $M(\tau, q)$ is the Radon transform; $d(x,t)$ is a seismic section, x is offset, $\phi(x)$ is the curvature for which the transform is defined; q is slope of the curvature; t is two-way travel time and τ is intercept two-way time. The inverse Radon transform is given by Beylkin (1987) and Yilmaz (2001) as:

$$d(t,x) = \int_{-\infty}^{\infty} \rho(\tau) * M(q, \tau = t - \phi(q,x))dq$$

where $*$ is the convolution of $\phi(q,x)$ with the rho filter $\rho(\tau)$. Yilmaz (2001) states that for 2-D data, the rho filter has a Fourier transform of the form $\sqrt{(}\omega)exp(i\pi/4)$, where ω is the temporal frequency (Yilmaz, 2001).

There are many versions, variations, and generalizations of the Radon transform as well as varied nomenclature used to describe different types of Radon transforms. In this study, I focus on the properties of the linear Radon transform or slant stack transform and the parabolic Radon transform.

2.3.1 Slant Stack Transform

The linear Radon transform is also called the slant-tack transform or the $\tau - P$ transform. Given a 2D section of seismic data, it is defined by summing data in the time-offset domain along a linear path:

$$M(\tau, p) = \int_{-\infty}^{\infty} d(t = \tau + px, x)dx$$

The discrete version of the slant stack transform is:

$$M(\tau, p) = \sum_{x} d(t = \tau + px, x)$$

where $M(\tau, p)$ is the slant stack transform; $d(x,t)$ is a common seismic gather; τ is two-way intercept time, t is two way travel time; x is offset; p is the ray parameter.

A seismic signal with a linear moveout in the time-offset domain can be mapped to a point with the slant-stack transform (Treitel et al., 1982).

2.3.2 Parabolic Radon Transform

A parabolic Radon transform can be built by summing the data along the stacking paths defined by the equation $t = \tau + qx^2$ (Hampson, 1986). An exact parabolic curve in the CMP domain can theoretically be mapped to a focused point in the parabolic Radon transform.

$$M(\tau, q) = \int_{-\infty}^{\infty} d(t = \tau + qx^2, x)dx$$

$$M(\tau, q) = \sum_{x} d(t = \tau + qx^2, x)$$

where $d(x,t)$ is a 2D seismic section; x is offset; τ is two way intercept time, t is two way travel time; q is the curvature of the parabola.

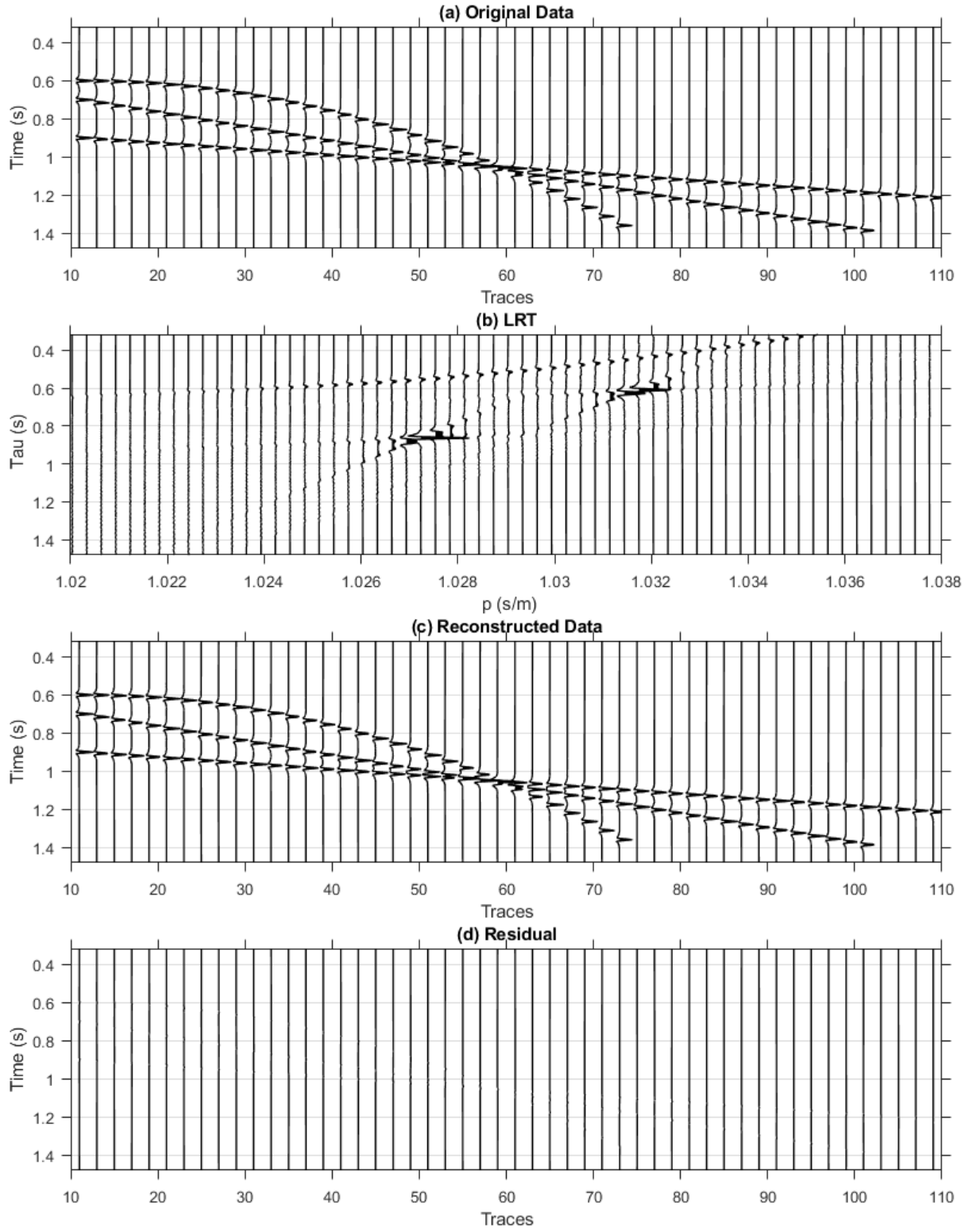

Figure 2.5: Demonstration of the forward and inverse linear Radon transforms for three seismic events, one with a parabolic moveout and two with linear moveouts.

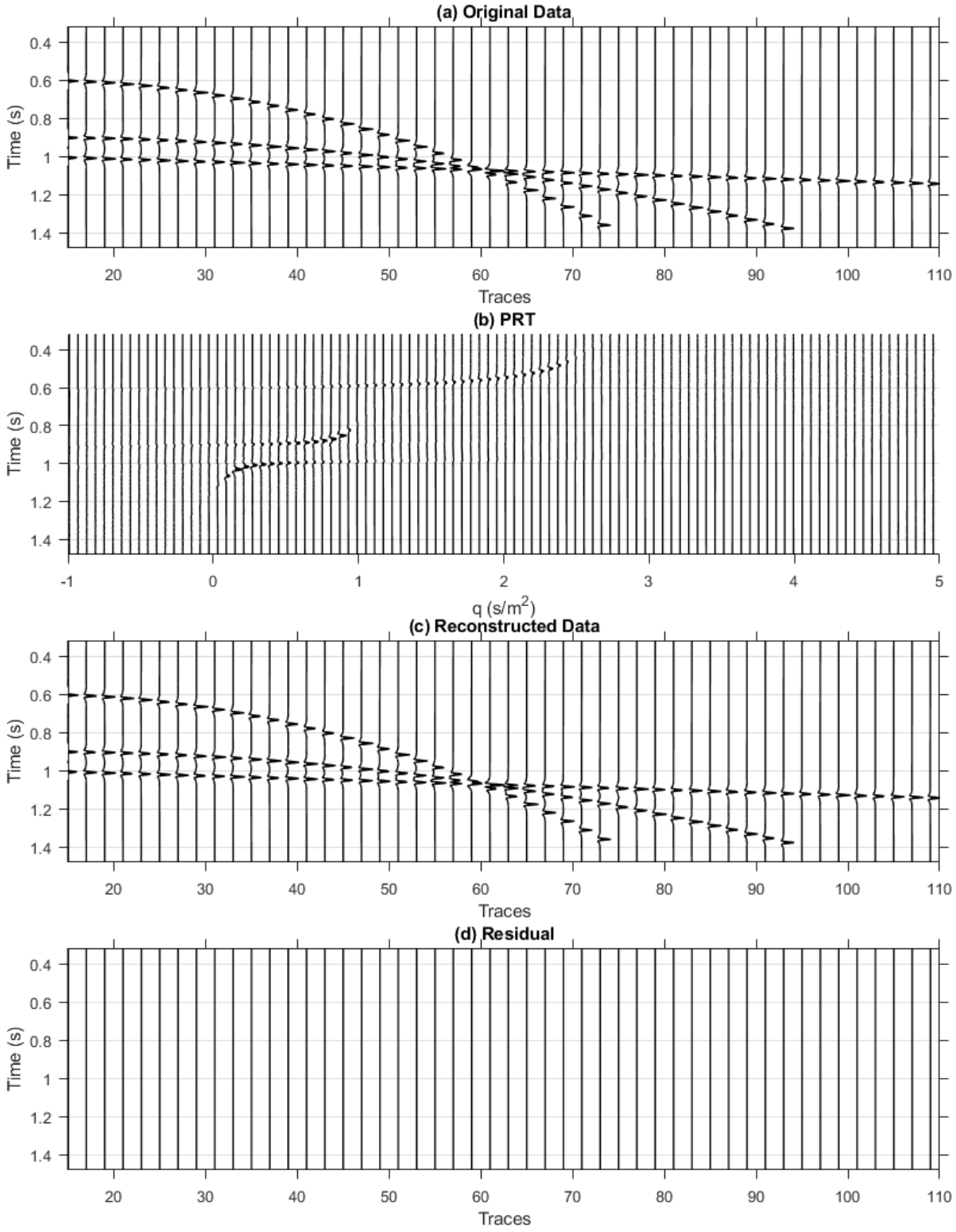

Figure 2.6: Demonstration of the forward and inverse parabolic Radon transforms for three seismic events, one with a parabolic moveout and two with linear moveouts.

Figures 2.5 and 2.6 illustrate the forward and inverse linear and parabolic Radon transforms respectively for two events, one with a parabolic moveout and one with a line moveout. In the slowness domain, the three seismic events are well separated. The linear event sums to a point while the amplitude of the parabolic event is spread over a curve. In the curvature domain, three events are also separated. The parabolic event is spread over a limited curvature range while the amplitudes of the linear events are also spread out around curvature values close to zero.

3. THE AUXILIARY S-TRANSFORM

3.1 Introduction

Conventional time-frequency analysis is applied to seismic data on a trace by trace basis. While this approach is useful, it doesn't make use of all available information since subsurface rocks are three-dimensional. The goal here is to develop a method that utilizes multi-trace coherency information and the separation of seismic events in the slowness or curvature domain in carrying out spectral decomposition and in improving the resolution of spectrally decomposed data. Multi-trace seismic processing techniques include integral transforms, commonly applied in the seismic data processing stage of seismic analysis such as the slant-stack transform or linear Radon transform and the parabolic Radon transform. These methods are generalizations of velocity filtering techniques for determining wave arrival slowness. Slant stacking can be considered as a directional beam-forming technique (Chapman, 1981); it can also be considered as a plane wave decomposition technique (Yilmaz, 2001). Slant stacking replaces the offset with the ray parameter p, which is the inverse of the horizontal phase velocity. It is typically carried out in shot-gather coordinates; seismic processing, however, is carried out in common mid-point coordinates. Each trace in a shot gather represents a plane wave that propagates at a certain angle from the vertical. As long as there is no dip, the travel times in a common-shot and a common-midpoint gather are indistinguishable; however a CMP gather is not from a single wavefield (Yilmaz, 2001). The technique however has also been applied in mid-point coordinates (Taner, 1977).

For post-stack migrated data in the CMP domain, velocity corrections have already been applied, hence at the depth location of the amplitudes of reflectors that line up in these coordinates, the seismic wave had similar ray parameters just before arriving at the interface. The slant stack procedure thus decomposes the data into traces with the same ray parameter p. I use the term ray parameter in the mathematical sense, i.e., it is the invariant in Snell's law and the time/offset-slope of the data; however, the ray parameter concept does not represent ray paths or wavefronts in

CMP coordinates (Ottolini and Claerbout, 1984). For practical purposes, the Radon transform is essentially a summation of amplitudes along a trajectory which represents the inverse of apparent velocity. Thus, applying this procedure to post-stack migrated data serves the purpose of representing the data in a domain where events are better separated and more coherent. For example, reflectors that form a straight line will sum up to separated points in the time-slowness domain. The amplitude in this domain is directly proportional to the coherency of the signal. The procedure emphasizes the energy associated with the events that follow linear trajectories in the CMP gather.

The Auxiliary S-transform integrates the Radon transform into the spectral decomposition process. The Auxiliary S-transform using the linear Radon transform is defined for a seismic section $d(x,t)$, where x is trace number and t is time as follows:

$$A(\eta,f,p)=\int_{-\infty}^{\infty}\int_{-\infty}^{\infty}d(x,t=\tau+px)\frac{|f|}{\sqrt{2\pi}}w(\eta-\tau,f)e^{-i2\pi f\tau}dxd\tau \tag{3.1}$$

where τ is intercept time, η is a parameter that controls the position on the time axis, p is slowness and $w(\eta,f)$ is the Gaussian window defined as:

$$w(\eta,f)=\frac{1}{\sqrt{2\pi}\sigma(f)}e^{-\frac{\eta^2}{2\sigma^2(f)}} \tag{3.2}$$

with the constraint that: $\int_{-\infty}^{\infty}w(\eta-\tau,f)d\tau=1$

The inverse of the Auxiliary S-transform is defined as:

$$d(x,t)=\int_{-\infty}^{\infty}\int_{-\infty}^{\infty}\int_{-\infty}^{\infty}[\rho(\tau)*A(\eta,f,p)]\,e^{i2\pi f\tau}d\eta dfdp \tag{3.3}$$

where $\rho(\tau)$ is the rho filter given as $\rho(\tau)=\frac{|w_o|}{2\pi}=|f_o|$ (Yilmaz, 2001).

A percentile coherency filter can be applied in the time-frequency-slowness domain, in this case, the inverse is given as:

$$d_{Filter}(x,t)=\int_{-\infty}^{\infty}\int_{-\infty}^{\infty}\int_{-\infty}^{\infty}[\rho(\tau)*A(\eta,f,p)]\,F(\eta,p)e^{i2\pi f\tau}d\eta dfdp \tag{3.4}$$

where $\rho(\tau)$ is the rho filter and $F(\eta, p)$ is a percentile coherency filter defined as:

$$F(\eta,p) = \begin{cases} 1, \text{ if } |m(p,\eta)| \geq |m(p,\eta)|_{percentile} \\ 0, \text{ otherwise} \end{cases} \tag{3.5}$$

and

$$m(p,\eta) = \int_{-\infty}^{\infty} d(x, \tau + px)dx \tag{3.6}$$

$m(p,\eta)$ is the linear Radon transform or slant-stack transform (Thorson and Claerbout, 1985) which is obtained by summing the seismic section along the linear trajectory ($\eta = \tau + px$).

3.2 Methodology

The Auxiliary S-transform is applied using the following steps:

1. The Radon transform is applied to a seismic section and the data is transformed to the time-slowness domain.

2. Equation 3.1 is applied to the section to produce a time-frequency-slowness volume.

3. A percentile coherency filter can be derived using the absolute value of the amplitudes in the new domain. Amplitudes below a certain selected threshold are muted. The percentile coherency filter can be applied to preserve the most coherent amplitudes and increase the separation of seismic events in the new domain.

4. Equation 3.3 is applied to the time-frequency-slowness volume to reconstruct the original data.

5. The inverse Radon transform can be applied to the time-frequency-slowness volume to map the data back into the time-frequency-offset domain for comparison with other methods and visualization. A 2D section is picked up based on a specific frequency. The horizontal axis of the 2D section represents trace location and the vertical represents time.

Figure 3.1 is a schematic illustrating the methodology of the Auxiliary S-Transform.

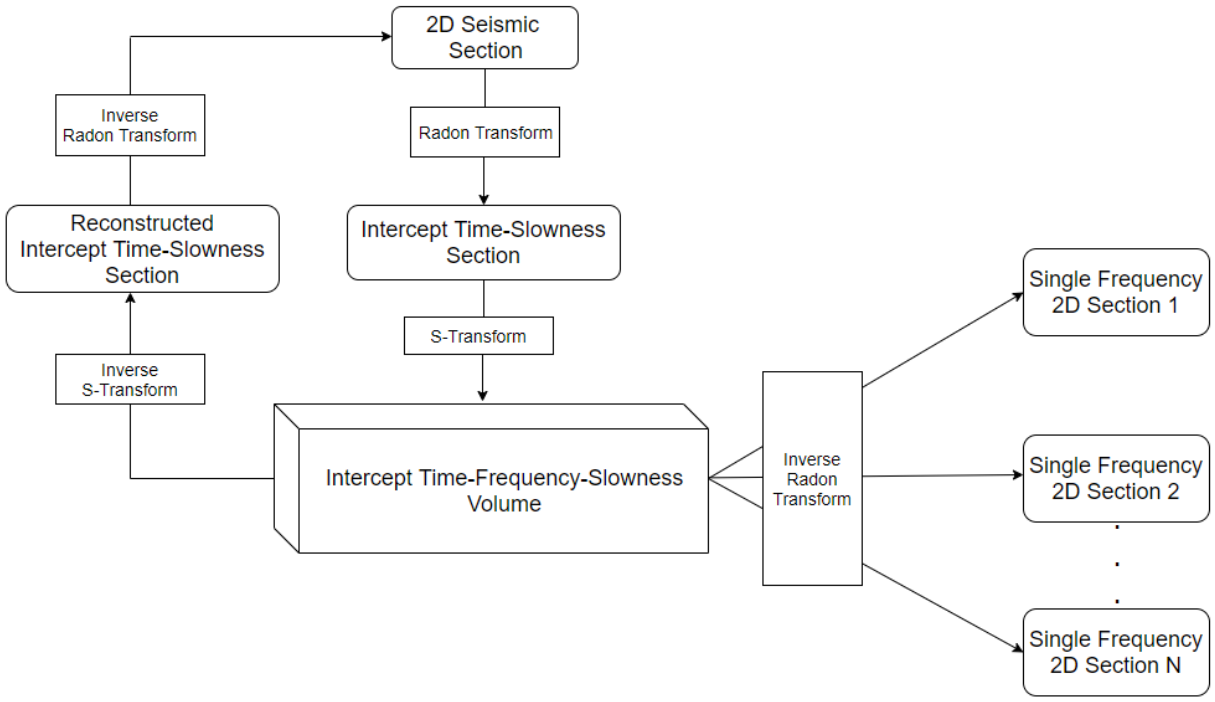

Figure 3.1: Methodology of the Auxiliary S-Transform

Figure 3.2 demonstrates the forward and inverse Auxiliary S-transform. Equation 3.1 is applied to a synthetic section with three events, one with a parabolic moveout and two with linear moveouts. The time-frequency-slowness volume generated is shown in Figure 3.2c. The inverse S-transform is applied to the time-frequency-slowness volume to map the data back into the intercept-time-slowness ($\tau - p$) domain, (Figure 3.2d). The linear Radon transform is then applied to transform the data back into the time-offset domain. The reconstructed data is shown in Figure 3.2e. In practice, it is useful to transform time-frequency-slowness volume into the time-frequency-offset domain. This is done by applying the linear Radon transform directly to the time-frequency-slowness volume (Figure 3.1c) for all frequencies. This is illustrated in Figure 3.3. Figure 3.3a shows the original data while Figure 3.3b shows the linear Radon transform of the data. The ST is applied to the data and LRT where the data is better separated. Figures 3.3c to h show single frequency panels at 20 Hz, 40 Hz, and 60 Hz for the ST and the AST (in Tau-p coordinates). The events are better separated in the AST panels. Figure 3.4 illustrates AST results mapped to

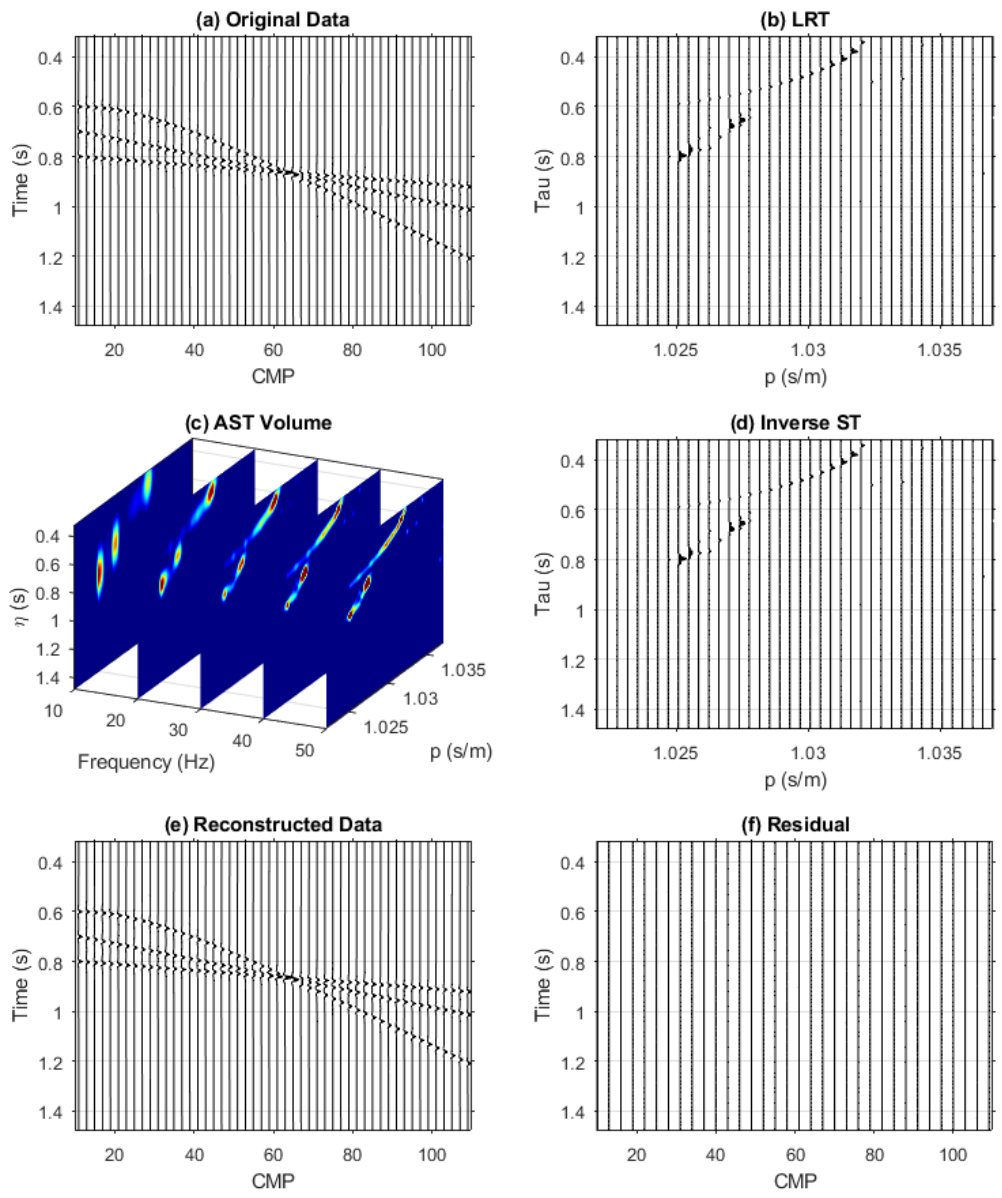

Figure 3.2: Demonstration of the forward and inverse Auxiliary S-transform (AST) for three seismic events, one with a parabolic moveout and two with linear moveouts. a) Original data. b) The linear Radon transform. c) The AST time-frequency-slowness volume. d) The AST inverted to the tau-p domain. e) The AST inverted to the time-offset domain to obtain the reconstructed data. f) The residual is obtained by subtracting the reconstructed data from the original data.

the time-offsets domain and compared to the ST. The temporal resolution of the AST is improved compared to the ST. Figures 3.4e and f show zoomed-in sections of the 60 Hz panel at Trace 71 for the ST and AST respectively and illustrate the improved temporal resolution of the AST.

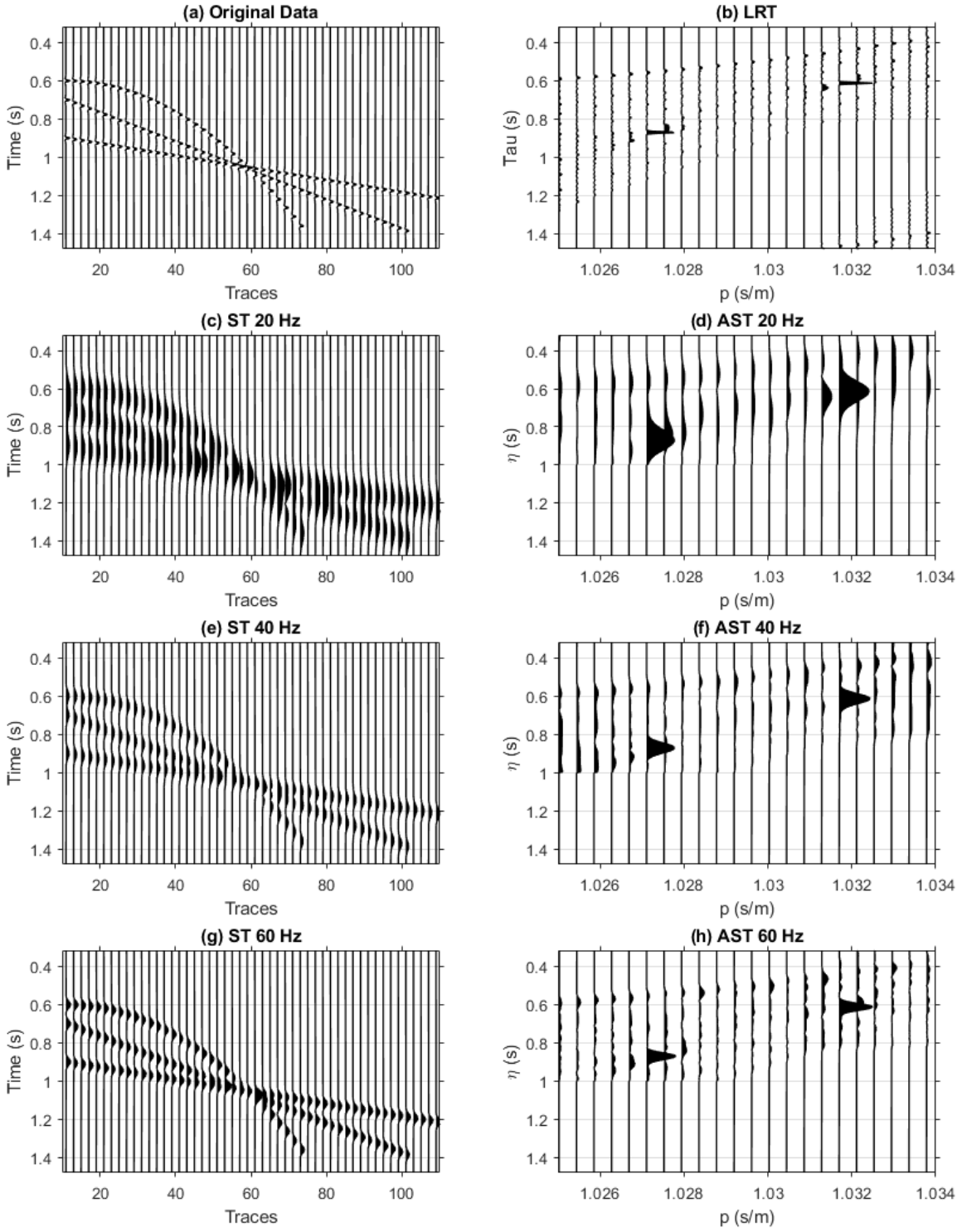

Figure 3.3: Separation of events on single frequency panels for the ST and the AST, for the three seismic events in Figure 3.1. a) The original data b) The linear Radon transform. c), e), and g) show the ST at 20Hz, 40Hz, and 60Hz respectively. d), f), and h) show the AST at 20 Hz, 40 Hz and 60 Hz respectively. Events at better separated in slowness coordinates.

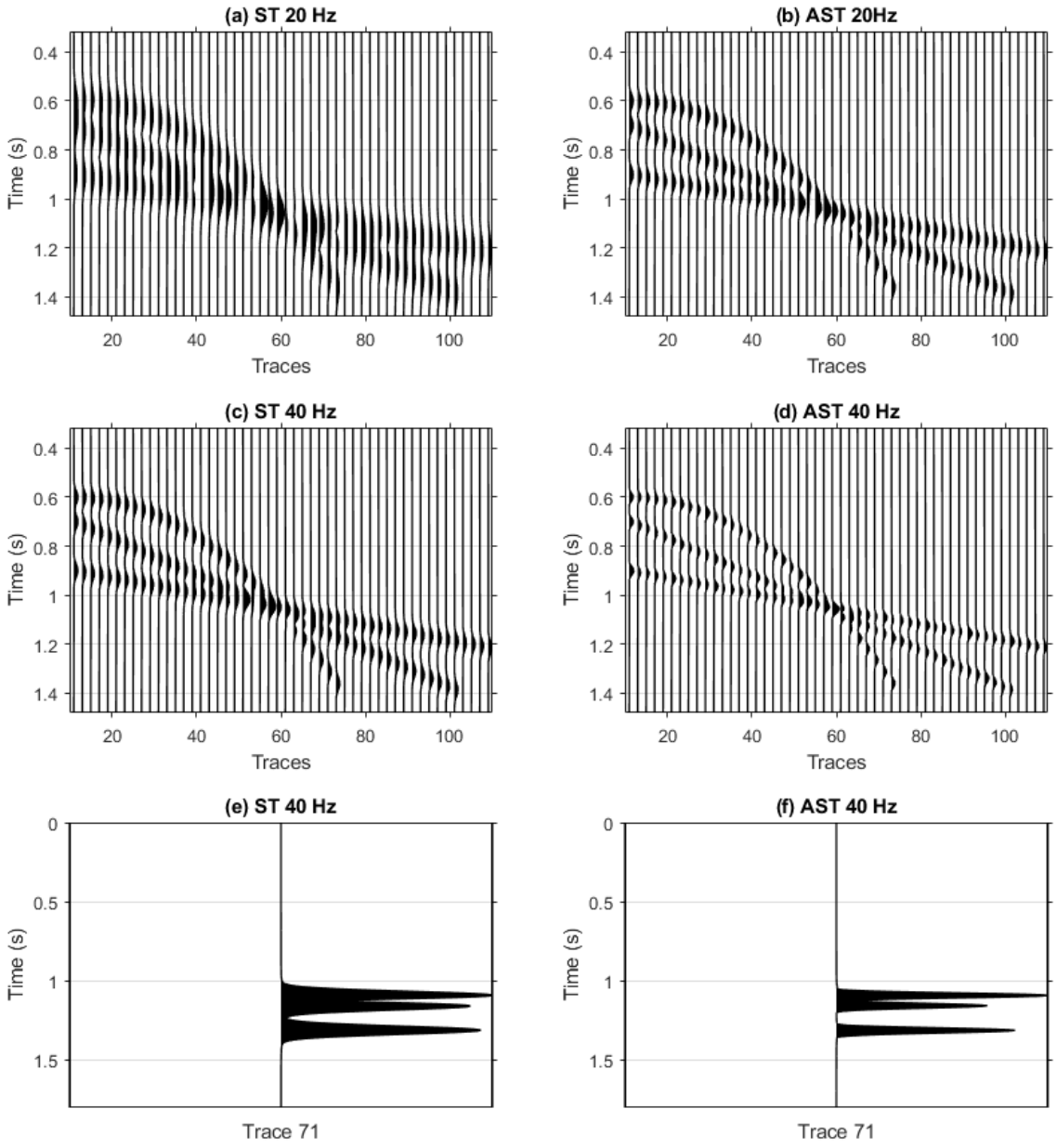

Figure 3.4: Comparison of single frequency panels of the ST and AST in time-offset coordinates inverted from the LRT. e) and f) show improved temporal resolution of the AST for a single trace.

3.3 Derivation of the Auxiliary S-transform

Given seismic section $d(x,t)$. The linear Radon transform is given as:

$$m(p,\tau) = \int_{-\infty}^{\infty} d(x, \tau + px)dx \tag{3.7}$$

Apply the s-transform to the individual traces in the $\tau - p$ domain:

$$A(f,\eta,p) = \int_{-\infty}^{\infty} m(p,\tau)\frac{|f|}{\sqrt{2\pi}}W(\eta-\tau)e^{-2\pi i f\tau}d\tau \tag{3.8}$$

$$A(f,\eta,p) = \int_{-\infty}^{\infty} m(p,\tau)\frac{|f|}{\sqrt{2\pi}}e^{\frac{-(\eta-\tau)^2 f^2}{2}}e^{-2\pi i f\tau}d\tau \tag{3.9}$$

Average over all η:

$$\int_{-\infty}^{\infty} A(f,\eta,p)d\eta = \int_{-\infty}^{\infty}\int_{-\infty}^{\infty} m(p,\tau)\frac{|f|}{\sqrt{2\pi}}e^{\frac{-(\eta-\tau)^2 f^2}{2}}e^{-2\pi i f\tau}d\tau d\eta \tag{3.10}$$

$$\int_{-\infty}^{\infty} A(f,\eta,p)d\eta = \int_{-\infty}^{\infty} m(p,\tau)e^{-2\pi i f\tau}d\tau \int_{-\infty}^{\infty}\frac{|f|}{\sqrt{2\pi}}e^{\left(\frac{-(\eta-\tau)^2 f^2}{2}\right)}d\eta \tag{3.11}$$

I first solve for the second integral:

$$\int_{-\infty}^{\infty}\frac{|f|}{\sqrt{2\pi}}e^{\frac{-(\eta-\tau)^2 f^2}{2}}d\eta \tag{3.12}$$

A curve translation doesn't change the shape under the curve, hence:

$$\int_{-\infty}^{\infty} e^{\frac{-(\eta-\tau)^2 f^2}{2}}d\eta = \int_{-\infty}^{\infty} e^{\frac{-\eta^2 f^2}{2}}d\eta \tag{3.13}$$

By using the integral principle of the Gaussian:

$$\int_{-\infty}^{\infty} e^{-\frac{x^2}{m}}dx = \sqrt{\pi m} \tag{3.14}$$

By applying equations 3.13 and 3.14 to equation 3.11 we obtain:

$$\frac{|f|}{\sqrt{2\pi}} \times \frac{\sqrt{2\pi}}{|f|} = 1 \tag{3.15}$$

Equation 3.11 then becomes:

$$\int_{-\infty}^{\infty} A(f,\eta,p)d\eta = \int_{-\infty}^{\infty} m(p,\tau)e^{-2\pi i f\tau}d\tau = M(p,f) \tag{3.16}$$

Which is the Fourier transform $M(p,f)$ of $m(p,\tau)$.

Hence the $m(p,t)$ can be retrieved from the AST as:

$$M(p,\tau) = \int_{-\infty}^{\infty} \left[\int_{-\infty}^{\infty} A(f,\eta,p)d\eta \right] e^{i2\pi f\tau}df \tag{3.17}$$

The data can be retrieved from $m(p,t)$ as:

$$d(x,t) = \int_{-\infty}^{\infty} |f_o| M(p,\tau = t - px)dp \tag{3.18}$$

which is the inverse of the AST (substitute (3.17) in (3.18)):

$$d(x,t) = \int_{-\infty}^{\infty}\int_{-\infty}^{\infty}\int_{-\infty}^{\infty} A(f,\eta,p)|f_o|e^{i2\pi f\tau}d\eta df dp \tag{3.19}$$

To prove equation (3.18): Recall the following three relations:

$$m(p,\tau) = \int_{-\infty}^{\infty} d(x,\tau + px)dx \tag{3.20}$$

$$M(p,f) = \int_{-\infty}^{\infty} m(p,\tau)e^{-2\pi i f\tau}d\tau \tag{3.21}$$

$$D(x,f) = \int_{-\infty}^{\infty} d(x,t)e^{-2\pi i f t}dt \tag{3.22}$$

Equation 3.20 can be written in the frequency domain using the shift theorem as:

$$M(p,f) = \int_{-\infty}^{\infty} D(x,f) e^{i2\pi f p x} dx \tag{3.23}$$

The standard back projection is:

$$D'(x,f) = \int_{-\infty}^{\infty} M(p,f) e^{-i2\pi f p x} dp \tag{3.24}$$

Substitute equation (3.23).

$$D'(x,f) = \int_{-\infty}^{\infty} \int_{-\infty}^{\infty} D(x',f) e^{-i2\pi f p (x'-x)} dx' dp \tag{3.25}$$

$$D'(x,f) = \int_{-\infty}^{\infty} dx' D(x',f) \int_{-\infty}^{\infty} e^{-i2\pi f p (x-x')} dp \tag{3.26}$$

If the p has an infinite range $(-\infty,\infty)$ we can define the function $\rho(x,f)$ as follows:

$$\rho(x,f) = \int_{-\infty}^{\infty} e^{-i2\pi f p x} dp \tag{3.27}$$

Then:

$$D'(x,f) = \int_{-\infty}^{\infty} D(x',f) \rho(x-x',f) dx' \tag{3.28}$$

$$D'(x,f) = D(x,f) * \rho(x,f) \tag{3.29}$$

Define

$$p' = -2\pi f_o p \tag{3.30}$$

Then:

$$\rho(x,f) = \int_{-\infty}^{\infty} \frac{1}{|2\pi f_o|} e^{ixp'} dp' = \frac{2\pi}{|2\pi f_o|} \delta(x) \tag{3.31}$$

$$D'(x,f) = \frac{2\pi}{|2\pi f_o|} D(x,f) * \delta(x) \tag{3.32}$$

$$D'(x,f) = \frac{1}{|f_o|} D(x,f) \tag{3.33}$$

$$D(x,f) = |f_o| D'(x,f) \tag{3.34}$$

Substitute equation (3.24)

$$D(x,f) = |f_o| \int_{-\infty}^{\infty} M(p,f) e^{-i2\pi fpx} dp \tag{3.35}$$

which is the time domain is:

$$d(x,t) = \int_{-\infty}^{\infty} |f_o| m(p, \tau = t - px) dp \tag{3.36}$$

Note that in the case that p is of a limited range (p_1, p_2) equation (3.27) becomes:

$$\rho(x,f) = \int_{p_1}^{p_2} e^{-i2\pi fpx} dp = \begin{cases} \dfrac{e^{-i2\pi fp_1x} - e^{-i2\pi fp_2x}}{i2\pi fx}, \text{ if } fx \neq 0 \\ p_2 - p_1, \text{ if } fx = 0 \end{cases} \tag{3.37}$$

3.4 Auxiliary S-transform with parabolic trajectory summation

In the above derivation, the multi-trace coherency information is retrieved by summing the data along linear trajectories. It is possible to sum the data along a curved trajectory such as a parabolic trajectory. The Auxiliary S-transform with a parabolic summation trajectory is outlined below.

Given a seismic section $d(x,t)$, where x is trace number and t is time, it is defined as:

$$A(f,\eta,q) = \int_{-\infty}^{\infty}\int_{-\infty}^{\infty} d(x,t=\tau+qx^2)\frac{|f|}{\sqrt{2\pi}}w(\eta-\tau,f)e^{-i2\pi f\tau}dxd\tau \tag{3.38}$$

where τ is intercept time, η is a parameter that controls the position on the time axis, q is the curvature and $w(\eta,f)$ is the Gaussian window defined as:

$$w(\eta,f) = \frac{1}{\sqrt{2\pi}\sigma(f)}e^{-\frac{\eta^2}{2\sigma^2(f)}} \tag{3.39}$$

with the constraint that: $\int_{-\infty}^{\infty} w(\eta-\tau,f)d\tau = 1$

The inverse of is defined as:

$$d(x,t) = \int_{-\infty}^{\infty}\int_{-\infty}^{\infty}\int_{-\infty}^{\infty} A(f,\eta,q)\sqrt{\frac{2\pi}{f_o k_q}}e^{i2\pi f\tau}d\eta df dq \tag{3.40}$$

k_q is a variable that corresponds to variable to the curvature q. A percentile coherency filter can be applied in the time-frequency-curvature domain, in this case, the inverse is given as:

$$d_{Filter}(x,t) = \int_{-\infty}^{\infty}\int_{-\infty}^{\infty}\int_{-\infty}^{\infty} A(f,\eta,q)\sqrt{\frac{2\pi}{f_o k_q}}F(\eta,q)e^{i2\pi f\tau}d\eta df dq \tag{3.41}$$

$F(\eta,q)$ is a percentile coherency filter defined as:

$$F(\eta,q) = \begin{cases} 1, \text{ if } |m(q,\eta)| \geq |m(q,\eta)|_{percentile} \\ 0, \text{ otherwise} \end{cases} \tag{3.42}$$

and

$$m(q,\eta) = \int_{-\infty}^{\infty} d(x, \tau + qx^2) dx \tag{3.43}$$

$m(q,\eta)$ is the parabolic Radon transform.

Figure 3.5 demonstrates the forward and inverse Auxiliary S-transform with parabolic summation trajectory. Equation 3.38 is applied to a synthetic section with three events, one with a linear moveout and two with parabolic moveouts. The time-frequency-slowness volume generated is shown in Figure 3.5c. The inverse S-transform is applied to the time-frequency-slowness volume to map the data back into the intercept-time-curvature ($\tau - q$) domain, (Figure 3.5d). The parabolic Radon transform is then applied to transform the data back into the time-offset domain. The reconstructed data is shown in Figure 3.5e. In practice, it is useful to transform time-frequency-curvature volume into the time-frequency-offset domain. This is done by applying the parabolic Radon transform directly to the time-frequency-curvature volume (Figure 3.5c) for all frequencies. This is illustrated in Figure 3.6. Figure 3.6a shows the original data while Figure 3.6(b) shows the parabolic Radon transform (PRT) of the data. The ST is applied to the data and PRT where the data is better separated. Figure 3.6c to h show single frequencies panels at 20 Hz, 30 Hz, and 50 Hz for the ST and the AST (in Tau-q coordinates). The events are better separated in the AST panels. Figure 3.7 illustrates AST results mapped to the time-offsets domain and compared to the ST. The temporal resolution of the AST is improved. Figures 3.7e and f show zoomed in sections of the 50 Hz panel at Trace 69 for the ST and AST respectively, and illustrate the improved temporal resolution of the AST.

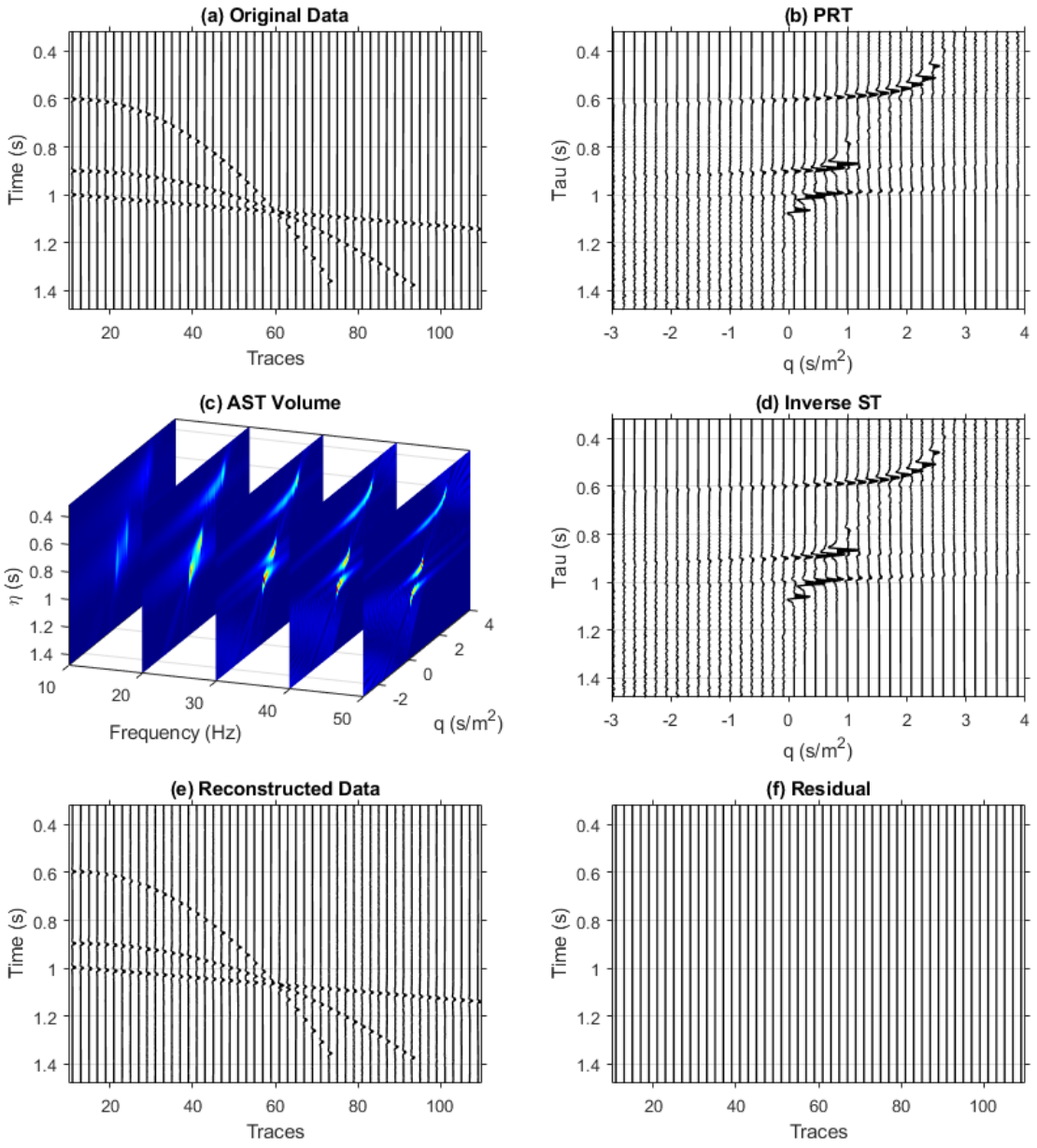

Figure 3.5: Demonstration of the forward and inverse AST for events with linear and parabolic moveouts. a) Original data. b) The parabolic Radon transform. c) The AST time-frequency-curvature volume d) The AST inverted to the Tau-p domain. e) The AST inverted to the time-offset domain to obtain the reconstructed data. f) The residual is obtained by subtracting the reconstructed data from the original data.

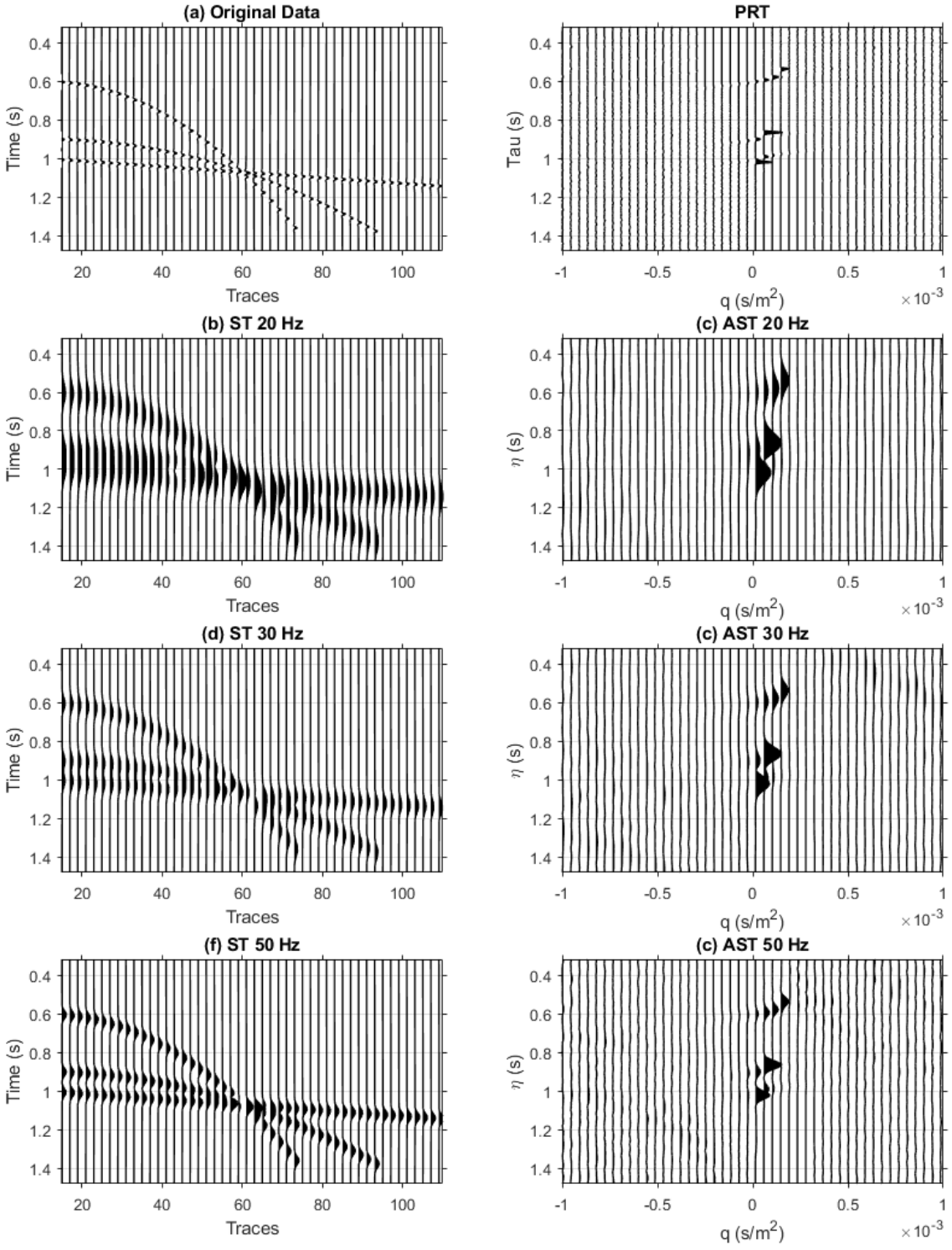

Figure 3.6: Separation of events on single frequency panels for the ST and the AST, for the three seismic events in Figure 3.1. a) The original data b) The parabolic Radon transform. c), e) and g) show the ST at 20Hz,40Hz and 60Hz respectively. d), f) and h) show the AST at 20 Hz, 40 Hz, and 60 Hz respectively. Events at better separated in curvature coordinates.

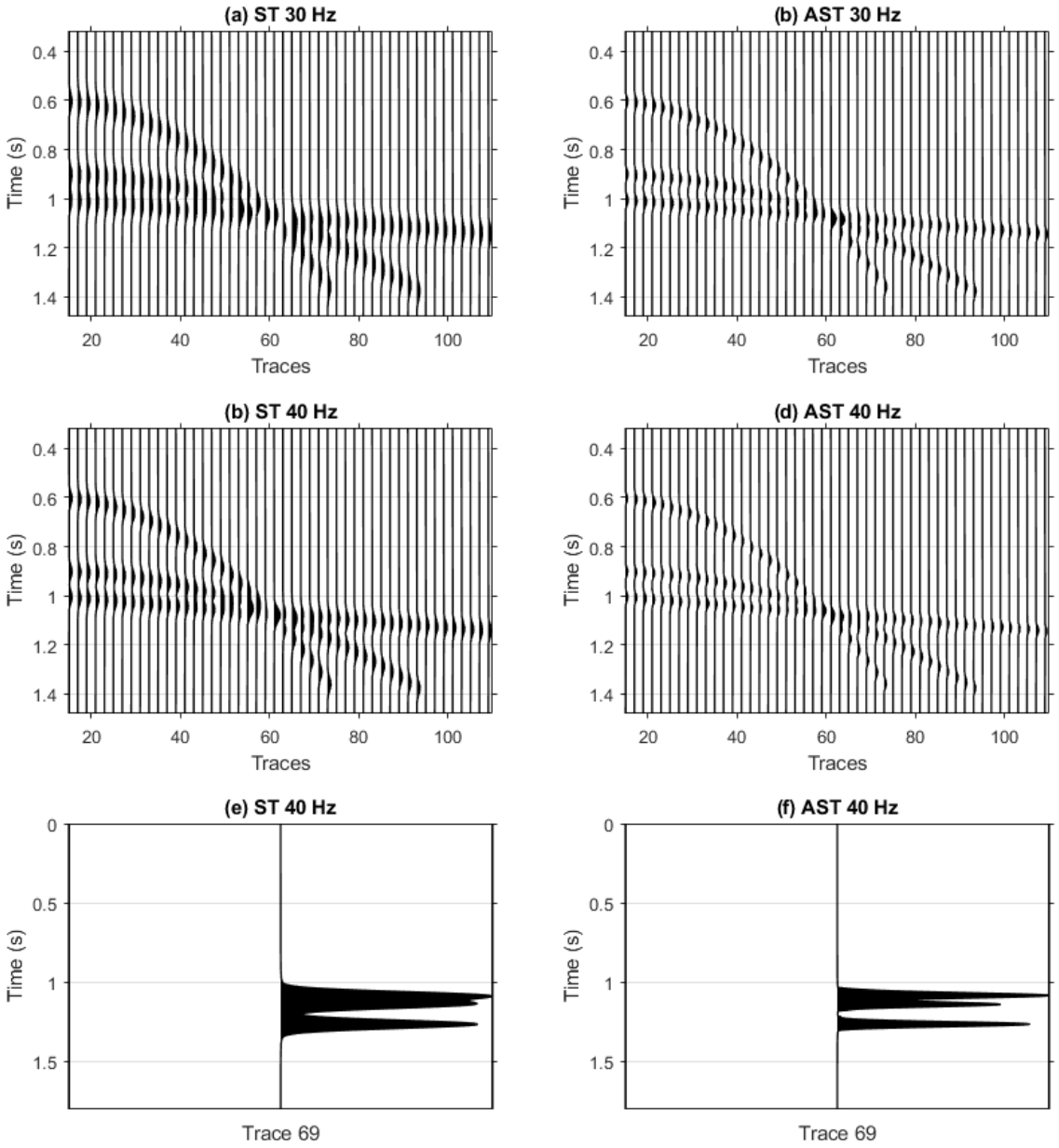

Figure 3.7: Comparison of single frequency panels of the ST and AST in time-offset coordinates inverted from the PRT. e) and f) show improved temporal resolution of the AST for a single trace.

3.4.1 Derivation of the Auxiliary S-transform with parabolic trajectory summation

Given seismic section $d(x,t)$. The linear Radon transform is given as:

$$m(q,\tau) = \int_{-\infty}^{\infty} d(x, \tau + qx^2)dx \tag{3.44}$$

Apply the s-transform to the individual traces in the $\tau - p$ domain:

$$A(f,\eta,q) = \int_{-\infty}^{\infty} m(q,\tau)\frac{|f|}{\sqrt{2\pi}}W(\eta-\tau)e^{-2\pi i f\tau}d\tau \tag{3.45}$$

$$A(f,\eta,q) = \int_{-\infty}^{\infty} m(q,\tau)\frac{|f|}{\sqrt{2\pi}}e^{\frac{-(\eta-\tau)^2f^2}{2}}e^{-2\pi i f\tau}d\tau \tag{3.46}$$

Average over all η:

$$\int_{-\infty}^{\infty} A(f,\eta,q)d\eta = \int_{-\infty}^{\infty}\int_{-\infty}^{\infty} m(q,\tau)\frac{|f|}{\sqrt{2\pi}}e^{\frac{-(\eta-\tau)^2f^2}{2}}e^{-2\pi i f\tau}d\tau d\eta \tag{3.47}$$

$$\int_{-\infty}^{\infty} A(f,\eta,q)d\eta = \int_{-\infty}^{\infty} m(p,\tau)e^{-2\pi i f\tau}d\tau \int_{-\infty}^{\infty}\frac{|f|}{\sqrt{2\pi}}e^{\left(\frac{-(\eta-\tau)^2f^2}{2}\right)}d\eta \tag{3.48}$$

I first solve for the second integral:

$$\int_{-\infty}^{\infty}\frac{|f|}{\sqrt{2\pi}}e^{\frac{-(\eta-\tau)^2f^2}{2}}d\eta \tag{3.49}$$

A curve translation doesn't change the shape under the curve, hence:

$$\int_{-\infty}^{\infty} e^{\frac{-(\eta-\tau)^2f^2}{2}}d\eta = \int_{-\infty}^{\infty} e^{\frac{-\eta^2f^2}{2}}d\eta \tag{3.50}$$

By using the integral principle of the Gaussian:

$$\int_{-\infty}^{\infty} e^{-\frac{x^2}{m}}dx = \sqrt{\pi m} \tag{3.51}$$

By applying equations 3.50 and 3.51 to equation 3.48 I obtain:

$$\frac{|f|}{\sqrt{2\pi}} \times \frac{\sqrt{2\pi}}{|f|} = 1 \tag{3.52}$$

Equation 3.48 then becomes:

$$\int_{-\infty}^{\infty} A(f,\eta,q)d\eta = \int_{-\infty}^{\infty} m(q,\tau)e^{-2\pi i f\tau}d\tau = M(q,f) \tag{3.53}$$

Which is the Fourier transform $M(q,f)$ of $m(q,\tau)$.

Hence the $m(p,t)$ can be retrieved from the AST as:

$$m(q,\tau) = \int_{-\infty}^{\infty} \left[\int_{-\infty}^{\infty} A(f,\eta,q)d\eta \right] e^{i2\pi f\tau}df \tag{3.54}$$

The data can be retrieved from $m(p,t)$ as:

$$d(x,t) = \int_{-\infty}^{\infty} \sqrt{\frac{2\pi}{f_o k_q}} m(q,\tau = t - px)dp \tag{3.55}$$

which is the inverse of the AST (substitute (3.54) in (3.55)):

$$d(x,t) = \int_{-\infty}^{\infty}\int_{-\infty}^{\infty}\int_{-\infty}^{\infty} A(f,\eta,q)\sqrt{\frac{2\pi}{f_o k_q}} e^{i2\pi f\tau}d\eta df dp \tag{3.56}$$

To prove equation (3.55), I first define the inverse parabolic Radon transform as:

$$d(x,t) = \int_{-\infty}^{\infty} m(q,t - qx^2)dq \tag{3.57}$$

In the frequency domain, this translates to:

$$D(x,f) = \int_{-\infty}^{\infty} M(q,f)e^{-i2\pi f q x^2} \tag{3.58}$$

To obtain the forward projection:

$$M'(q,f) = \int_{-\infty}^{\infty} D(x,f) e^{i2\pi f q x^2} \tag{3.59}$$

Substitute equation (3.58):

$$M'(q,f) = \int_{-\infty}^{\infty} \int_{-\infty}^{\infty} M(q',f) e^{i2\pi f x^2 (q-q')} dp' dx \tag{3.60}$$

$$M'(q,f) = \int_{-\infty}^{\infty} dp' M(p',f) \int_{-\infty}^{\infty} e^{i2\pi f x^2 (q-q')} dx \tag{3.61}$$

$$M'(q,f) = \int_{-\infty}^{\infty} M(p',f) \rho(q-q',f) dp' \tag{3.62}$$

$$M'(q,f) = M(p',f) * \rho(q,f) \tag{3.63}$$

where

$$\rho(q,f) = \int_{-\infty}^{\infty} e^{i2\pi f q x^2} dx \tag{3.64}$$

In the frequency domain this becomes:

$$M'(q,f) = M(k_q,f) \rho(k_q,f) \tag{3.65}$$

$$M(k_q,f) = \frac{M'(q,f)}{\rho(k_q,f)} \tag{3.66}$$

$$M(k_q,f) = \frac{\sqrt{2\pi f_o} M'(q,f)}{\rho'(k_q,f)} \tag{3.67}$$

Zhou and Greenhalgh (1994) showed that in the case when x is infinite equation (3.64) be-

comes:

$$\rho'(k_q) = \frac{2\pi}{\sqrt{k_q}} \tag{3.68}$$

Hence:

$$M(k_q, f) = \sqrt{\frac{f_o k_q}{2\pi}} M'(q, f) \tag{3.69}$$

$$M(k_q, f) = \sqrt{\frac{f_o k_q}{2\pi}} \int_{-\infty}^{\infty} D(x, f) e^{i2\pi f q x^2} \tag{3.70}$$

$$D(x, f) = \sqrt{\frac{2\pi}{f_o k_q}} \int_{-\infty}^{\infty} M(k_q, f) e^{-i2\pi f q x^2} \tag{3.71}$$

which is the frequency domain equivalent of equation (3.55). In the case when the range of x is finite in the range $(-x_1, x_2)$ there is no analytical solution for $\rho(q, f)$, however the integral can be approximated by numerical quadrature methods (Zhou and Greenhalgh, 1994)). For a rectangular integration rule:

$$\rho(q, f) \approx \Delta x \sum_{x_k = x_1 + (k-1)\Delta x}^{x_2} e^{i2\pi f q x_k^2} \tag{3.72}$$

3.5 The percentile coherency filter

The improved temporal resolution of the Auxiliary S-transform depends on the separation of seismic events achieved in the slowness or curvature domain. Due to the polarity of the data, complex geometry, and significant interference of events, it is possible the seismic events interfere in the slowness domain. A percentile coherency filter (PCF) can be applied in this domain to increase the separation between coherent events in the slowness/curvature domain. The parameter is chosen in such a way as to strike a balance between the separation of events and retaining useful data. If the parameter value is too low, the events will not be well separated. If the parameter value is too high, useful data may be muted and some events may be missing after reconstruction. The optimal choice can be achieved by iteratively computing the filter and visually selecting the value that causes reasonable separation of events while retaining all coherent signals. Typical values of the PCF range from 90% to 99.5%.

To test the effect of the percentile coherency filter on the performance of the Auxiliary S-transform I apply it to the complex geometry of a synthetic igneous intrusion cutting across several horizontal rock layers. Figure 3.8 shows the synthetic igneous intrusion created by convolving a 30 Hz wavelet with a complex reflector geometry. I first compare the performance of the S-transform to the performance of the Auxiliary S-transform (99% PCF) for the igneous intrusion (Figure 3.8). I generate time-frequency-offset volumes and compare the S-transform and the Auxiliary S-transform at specific frequencies (Figure 3.9). The S-transform is unable to completely resolve the horizontal layers at 20 Hz, 36 Hz, and 40 Hz; while the Auxiliary S-transform is able to completely resolve the geometry at these frequencies. The Auxiliary S-transform for this example is computed using a 99% percentile coherency filter. I vary the value of the percentile coherency filter from 96% to 99% (Figure 3.10). For a percentile coherency filter of 96%, the filtered image shows poor separation between the events in the slowness domain and the igneous intrusion geometry is not well resolved. The percentile coherency filter images show increasing separation as the value increases to 99% where the complete separation is achieved in the slowness domain and the geometry is properly reconstructed.

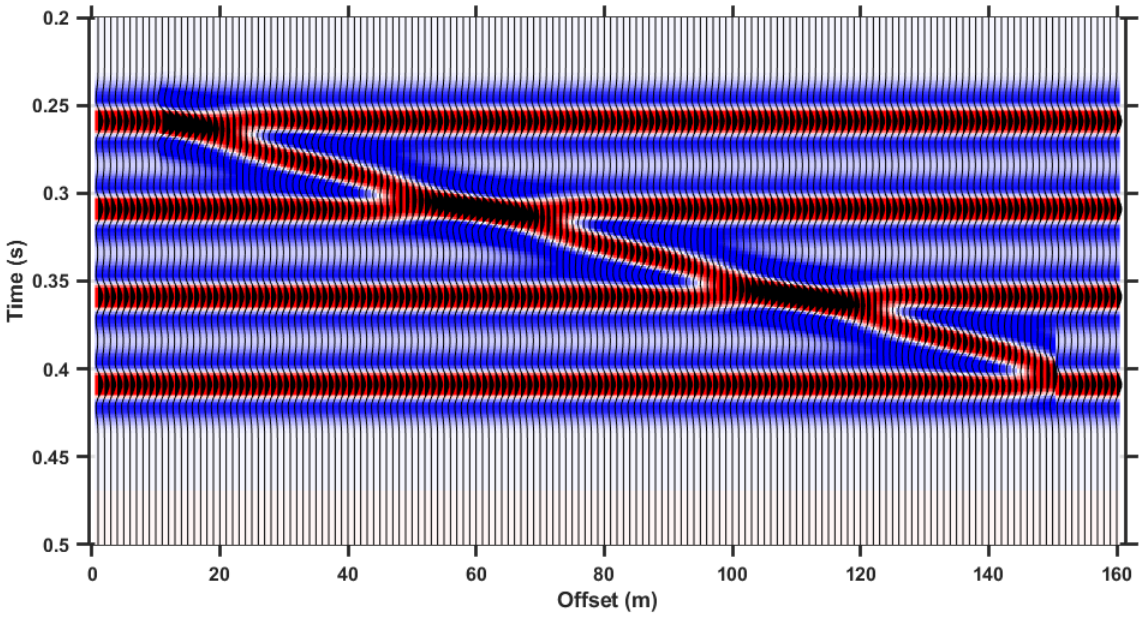

Figure 3.8: Synthetic seismic igneous intrusion generated by convolving a 30 Hz Ricker wavelet with a geometry of reflectors containing three tuning wedges.

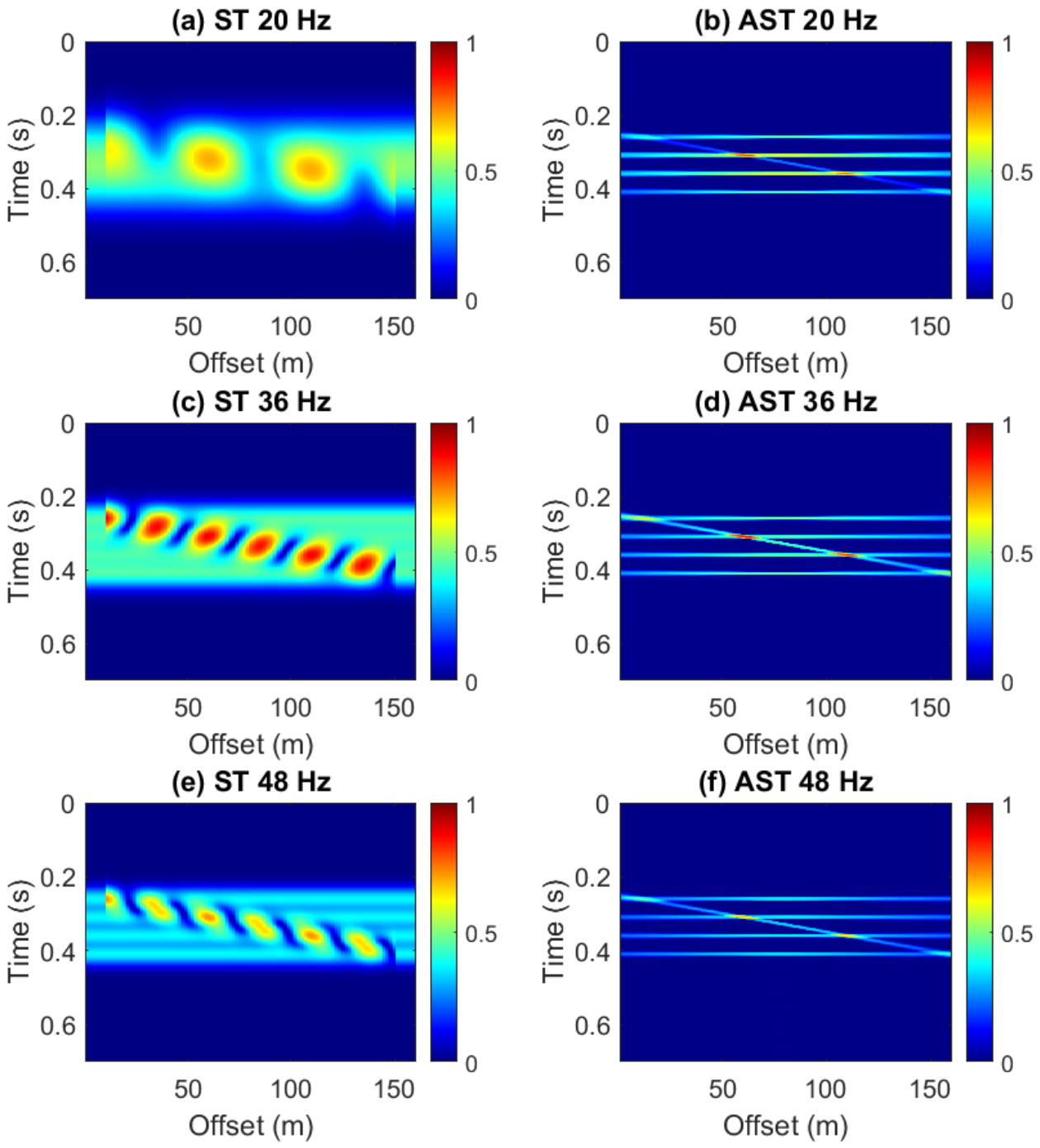

Figure 3.9: Comparison of ST and AST for igneous intrusion using a 99% percentile coherency filter (PCF).

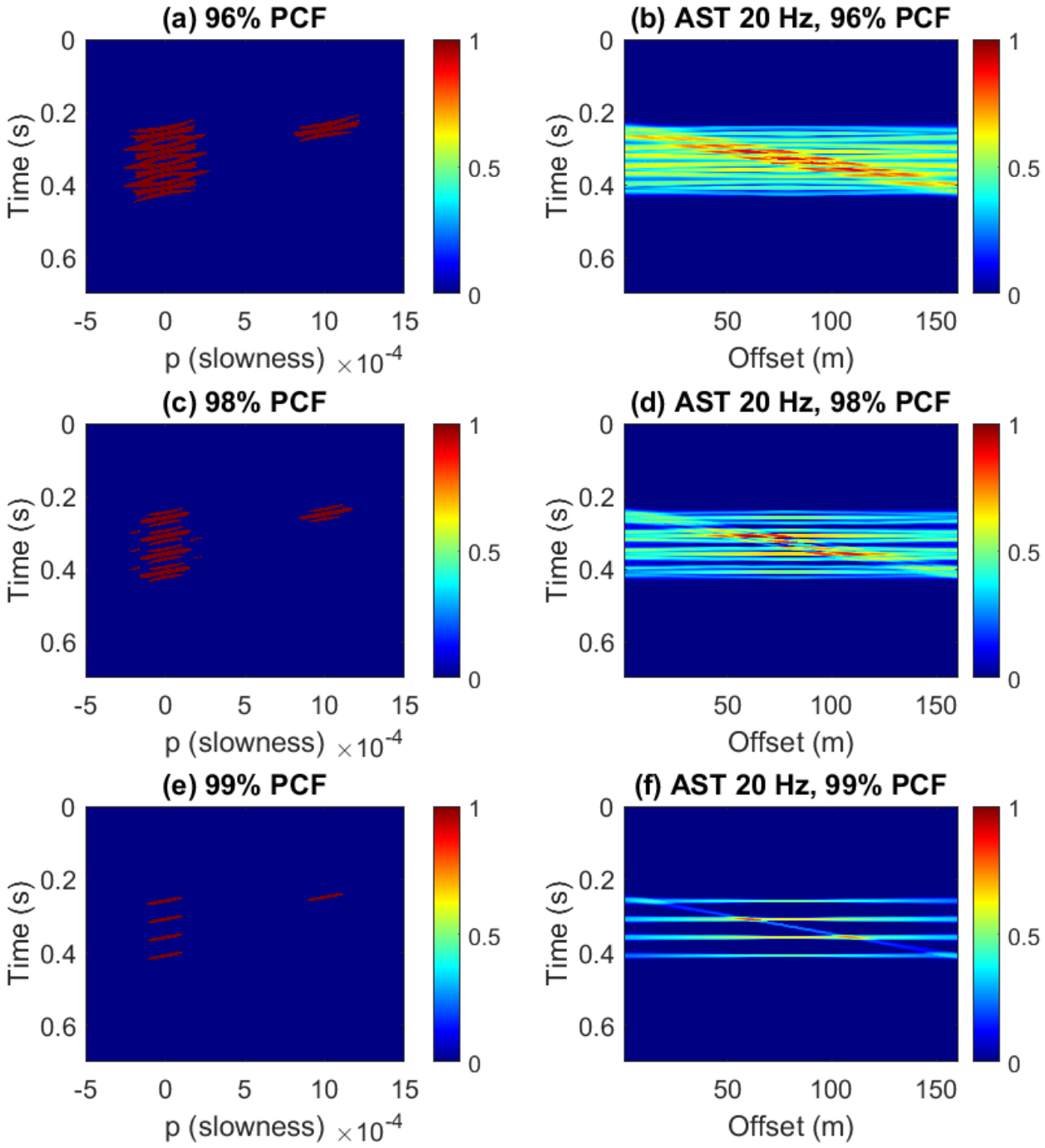

Figure 3.10: Effect of percentile coherency filter (PCF). The temporal resolution increases as the the value of the PCF changes from 96% to 99%.

3.6 Time and Frequency Resolution of the Auxiliary S-transform

Spectral decomposition reveals features that may only be obvious at specific frequencies. While the S-transform improves on other methods like the STFT and the CWT, its resolution may still be insufficient for high-resolution seismic interpretation problems. The features revealed are thus limited by the resolution. The Auxiliary S-transform is designed to significantly improve on the resolution of the S-transform. To test the resolution of both methods I make use of a synthetic tuning seismic wedge. The zero-offset seismic wedge model is generated by convolving a 40 Hz Ricker wavelet with a reflectivity wedge model for an odd reflection coefficient pair. The reflectivity is generated from the geological model given in Table (3.1).

Geological Model				
Layer Type	V_p (m/s)	V_s (m/s)	ρ (g/cn^3)	*Impedance* $(m/s.g/cn^3)$
Shale	2340	966	2.19	5125
Gas Sand	1850	1228	1.9	3515
Water sand	2342	970	2.20	5152

Table 3.1: Geological model for constructing synthetic wedge. The layer properties generate a reflectivity of -0.2 between shale and gas sand layers and a reflectivity of +0.2 between the gas sand and water sand layers.

Figure 3.11 shows the generation of the synthetic tuning wedge for a bright spot scenario. Figure 3.11a shows the odd reflection coefficient pair generated from the geological model in Table (3.1). Figure 3.11b and c show a 25 Hz Ricker wavelet and its amplitude spectrum. The Ricker wavelet is convolved with the pair of reflectors to generate the data in panel (d). The black line in panel (d) indicates the tuning thickness of the wedge where constructive wavelet interference peaks (Widess, 1973). I apply both the S-transform (ST) and the Auxiliary S-transform (AST) to the synthetic seismic wedge and compare their time-frequency-space volumes (Figure 3.12). The temporal resolution of the AST is much better than the resolution of the ST at low, intermediate,

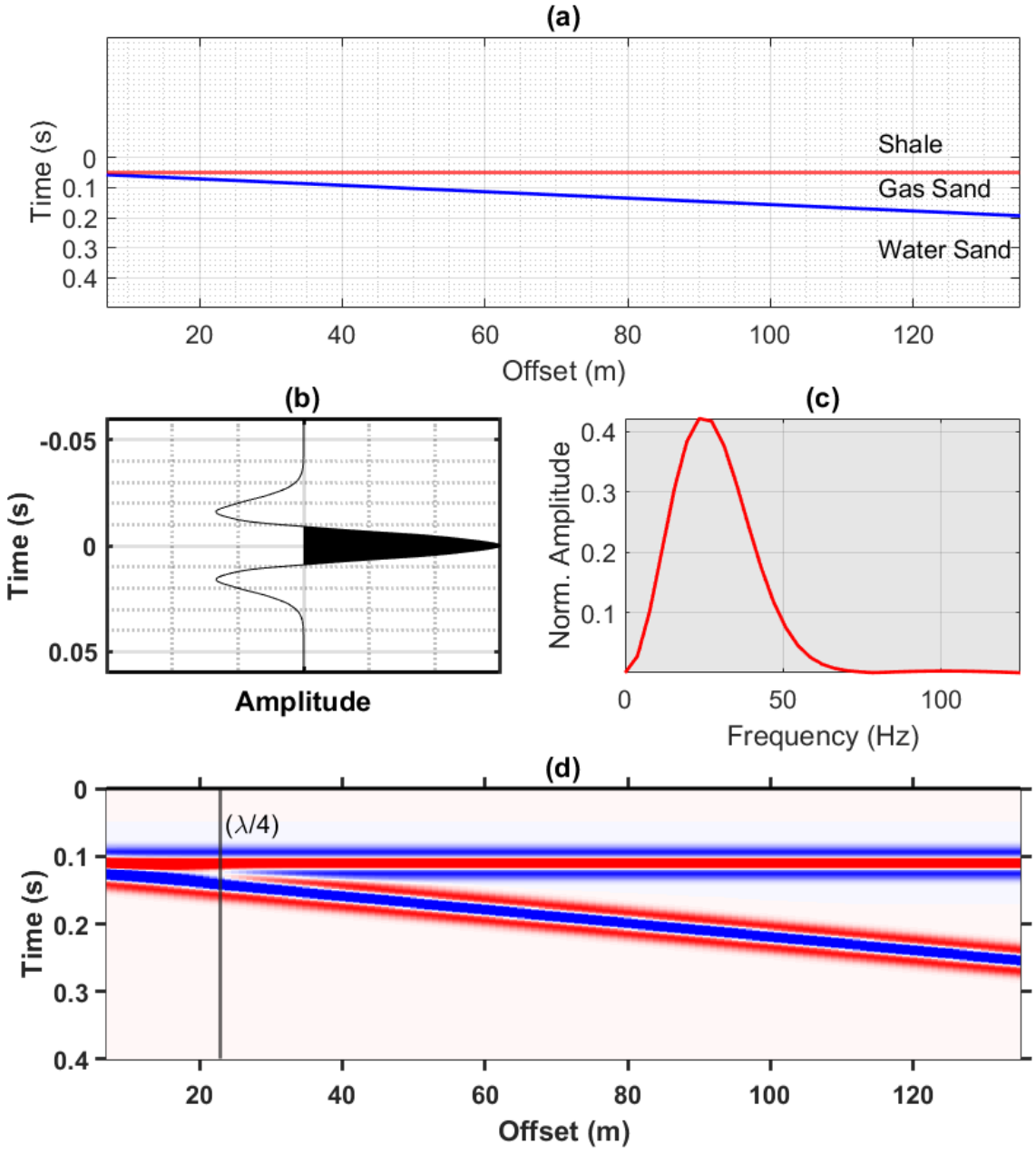

Figure 3.11: Generation of a synthetic tuning wedge. a) Odd reflection coefficient pair. b) A 25 Hz Ricker wavelet. c) The amplitude spectrum of the Ricker wavelet. d) The seismic tuning wedge generated by convolving the 40 Hz Ricker wavelet with the reflector pair.

and high frequencies. In addition, at low frequencies, the AST has higher amplitudes at the center of the wedge. This effect reduces towards the edge of the wedge, with the exception of the wedge

junction. This indicates the AST is better at imaging coherent (laterally continuous) signals. By measuring the distance between the wedge arms at the same location on the ST and AST volumes, I estimate that that the AST improves on the resolution of the ST by as much as 40%.

To investigate the frequency resolution of the AST, I examine the behavior at specific traces as the separation between the wedge increases (Traces 35, 51, 81, and 111). I extract the time-frequency panels for each trace and examine the change in amplitude at a specific time and compare the frequency resolution to that of the ST in Figure 3.13. The red curves in the last column of panels of Figure 3.13 are amplitudes extracted from the ST panel along the white line while the blue curves are amplitudes extracted from the AST panel along the white line. The red and blue curves match indicating that the AST at least preserves the frequency resolution of the ST. In addition as opposed to the AST, the ST amplitudes are affected by interference where the reflectors almost meet, at Traces 35 and 51.

Figure 3.14 examines the temporal resolution of the AST and compares it to that of the ST. Again, I examine the specific traces (Traces 35, 51, 81, and 111) as the separation of the wedge increases. The ST is unable to completely resolve the time separation between the two arrivals at all trace locations, however, the AST is able to resolve the arrivals. For each trace, I extract the time-frequency panels and extract amplitudes at a specific frequency along the white line for both the ST and AST. I compare the amplitudes in the last column of panels of Figure 3.14. The red and blue curves are amplitudes extracted from the ST and AST panels respectively; they indicate superior temporal resolution of the AST compared to the ST. The AST thus preserves the frequency resolution of the ST but demonstrates superior temporal resolution to the ST at all frequencies.

I repeat the process for AST with a 99% percentile filter. Figures (3.15) and (3.16) show the frequency and temporal resolution respectively. Again the AST preserves the frequency resolution of the ST but further improves on the temporal resolution at all frequencies.

Figure 3.17 shows the full temporal width at half maximum (FWHM) as a function of frequency at the location of Trace 10, for the ST and AST. The temporal FWHM is a measure of window width. The FWHM for the AST is lower than that of the ST at all frequencies; this demonstrates

that the AST has superior temporal resolution to the ST. The superior temporal resolution of the AST is most prominent at low frequencies, where the separation between the FWHM for the ST and AST increases (Figure 3.17). For the AST, the FWHM is constant at low and intermediate frequencies and further improves at high frequencies.

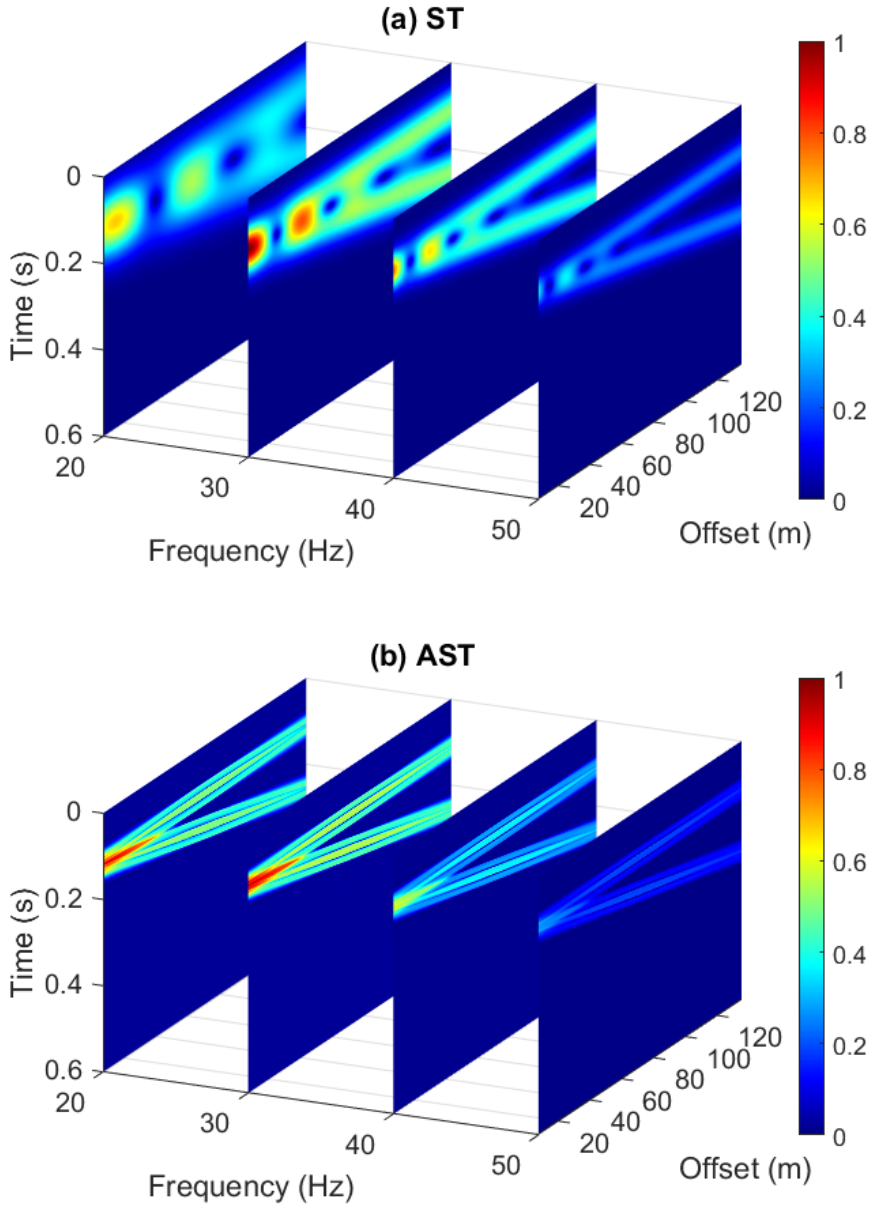

Figure 3.12: Comparison of ST and AST time-frequency-space volumes for the synthetic wedge.

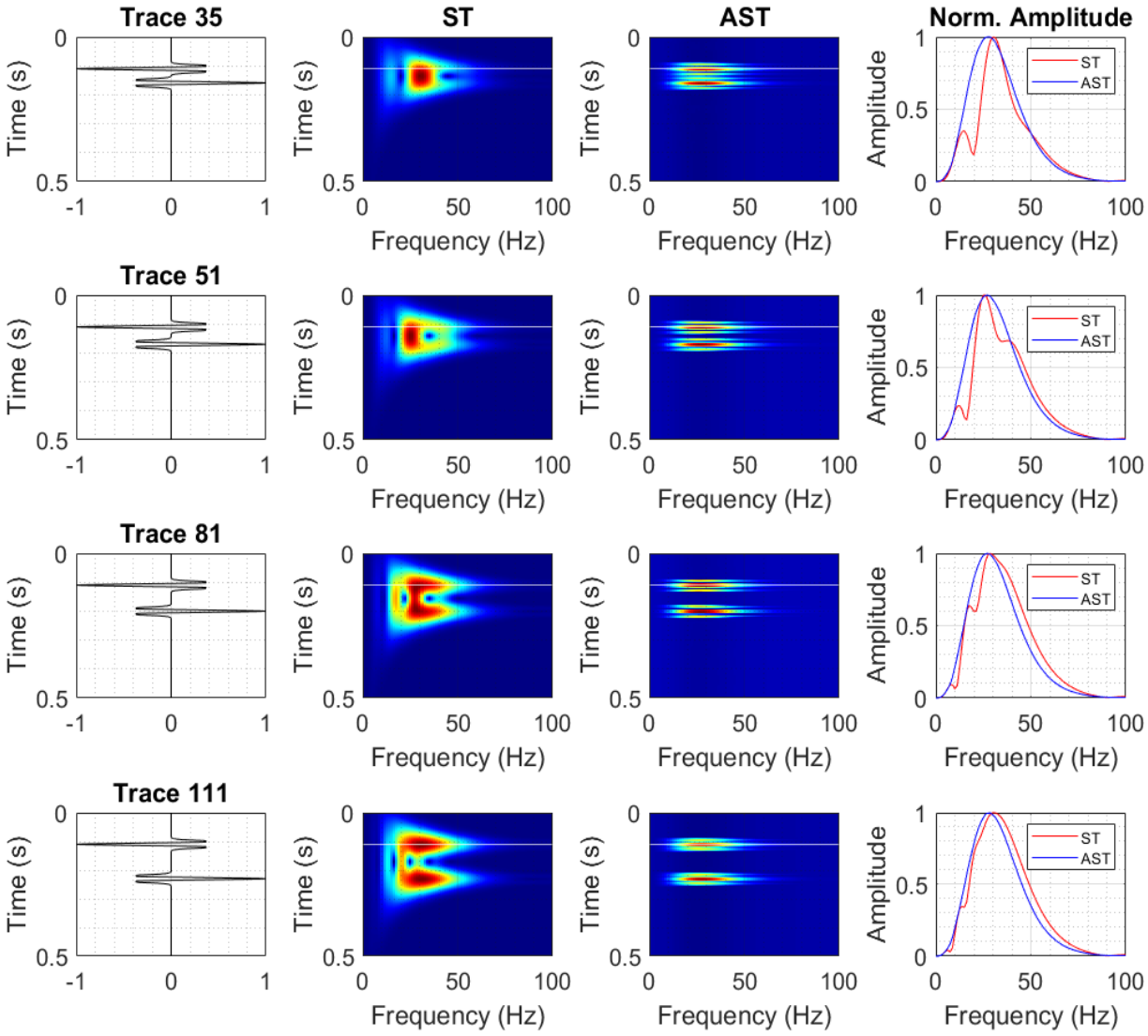

Figure 3.13: Comparison of the frequency resolution of the ST to that of the AST at different trace locations extracted from the synthetic wedge as the wedge separation increases. The second and third column of panels show the time-frequency panels for the ST and AST respectively. The amplitudes shown in the fourth column of panels are extracted along the white lines.

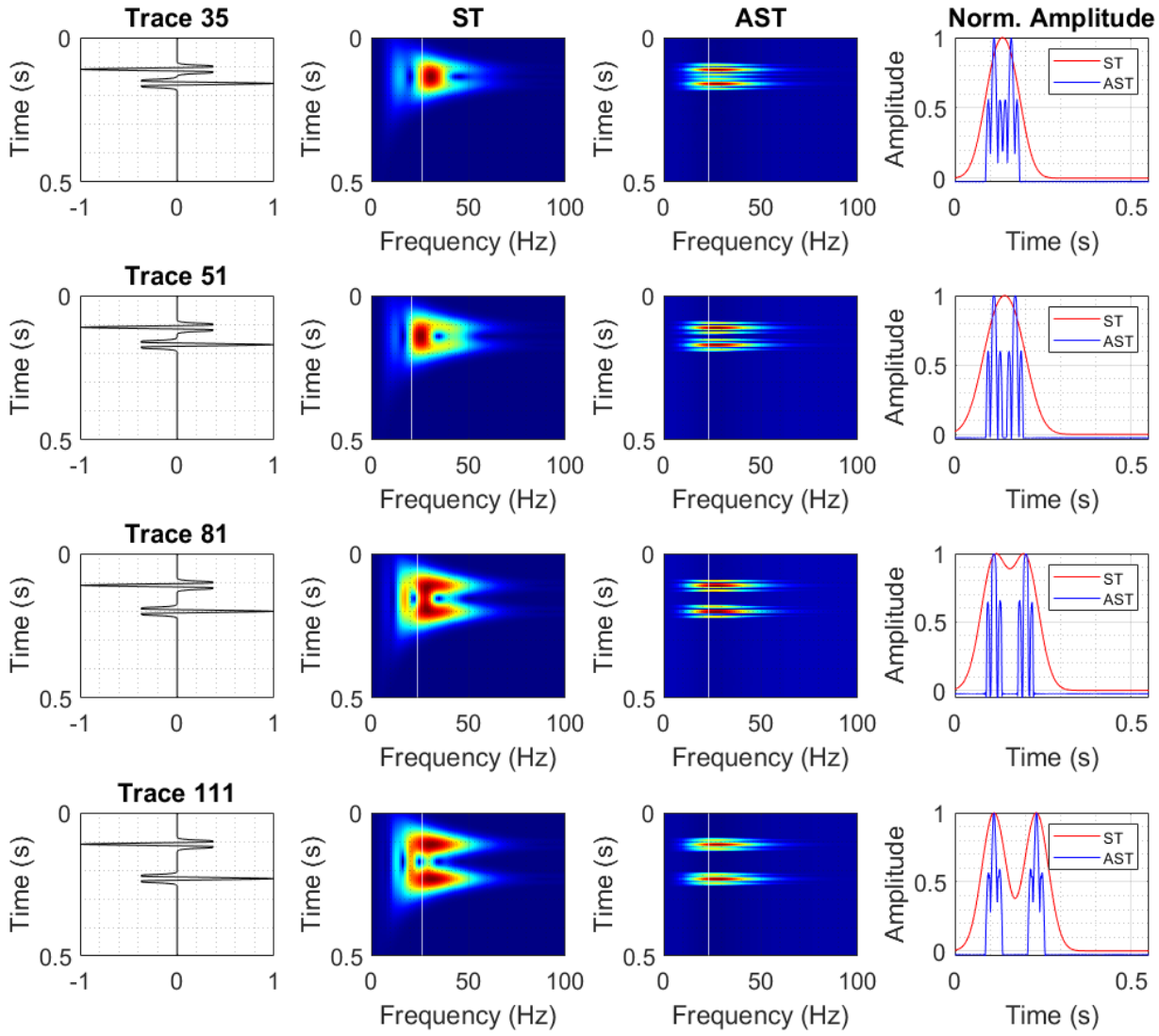

Figure 3.14: Comparison of the temporal resolution of the ST to that of the AST at different trace location extracted from the synthetic wedge as the wedge separation increases. The second and third columns of panels show the time-frequency panels for the ST and AST respectively. The amplitudes shown in the fourth column of panels are extracted along the white lines.

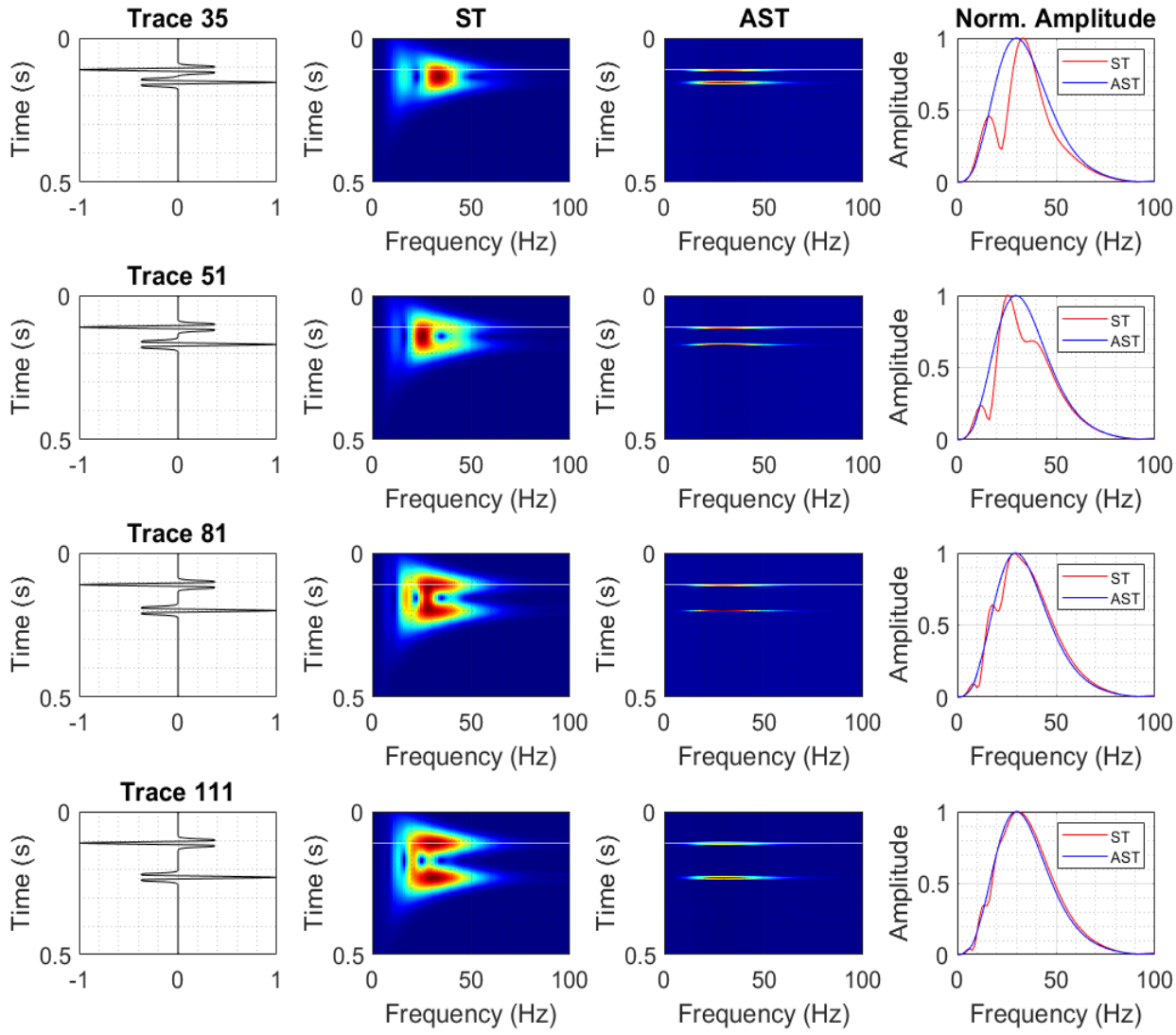

Figure 3.15: Comparison of the frequency resolution of the ST to that of the AST (99% PCF) at different trace locations extracted from the synthetic wedge as the wedge separation increases. The second and third columns of panels show the time-frequency panels for the ST and AST respectively. The amplitudes shown in the fourth column of panels are extracted along the white lines.

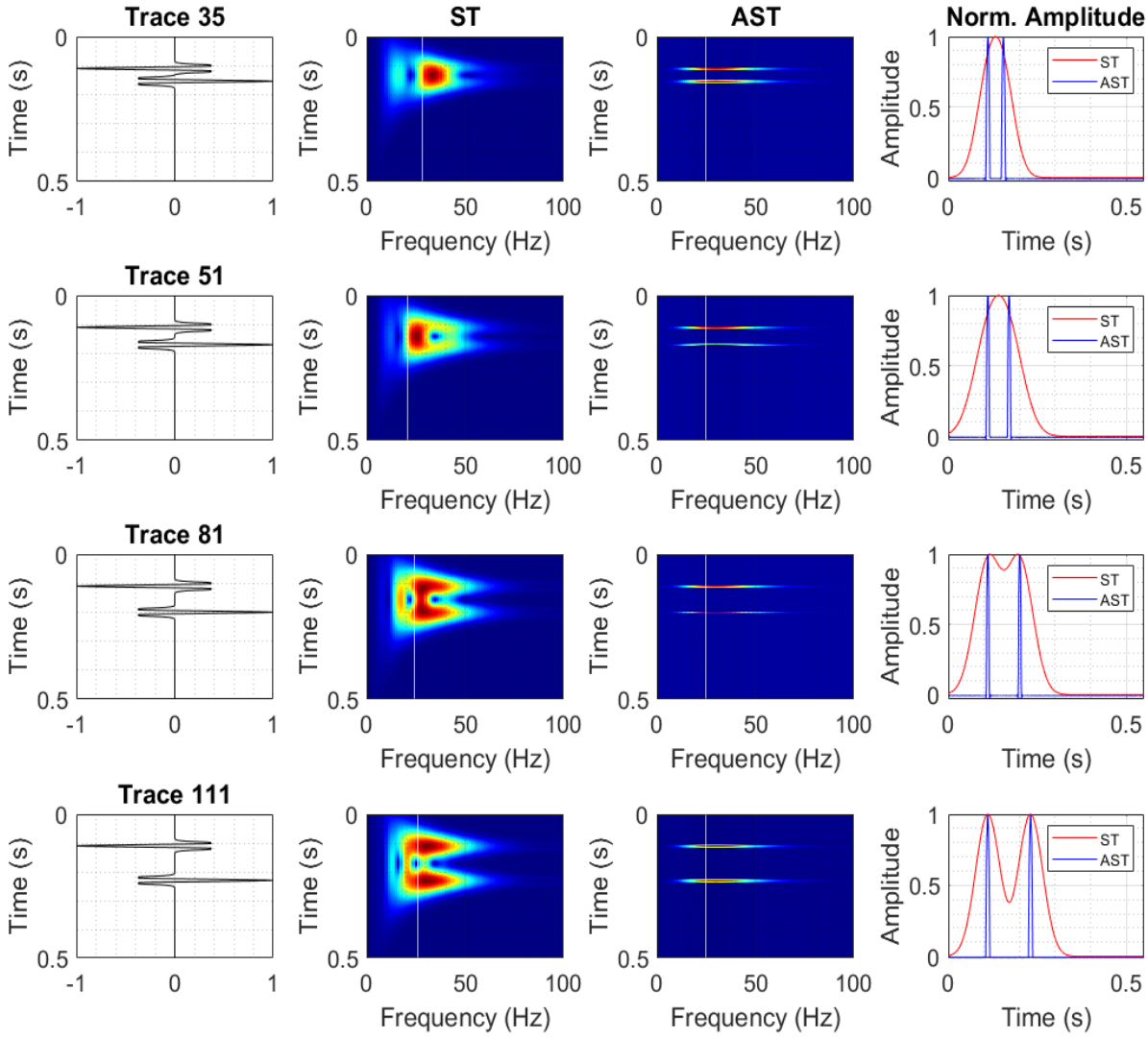

Figure 3.16: Comparison of the temporal resolution of the ST to that of the AST (99% PCF) at different trace locations extracted from the synthetic wedge as the wedge separation increases. The second and third columns of panels show the time-frequency panels for the ST and AST respectively. The amplitudes shown in the fourth column of panels are extracted along the white lines.

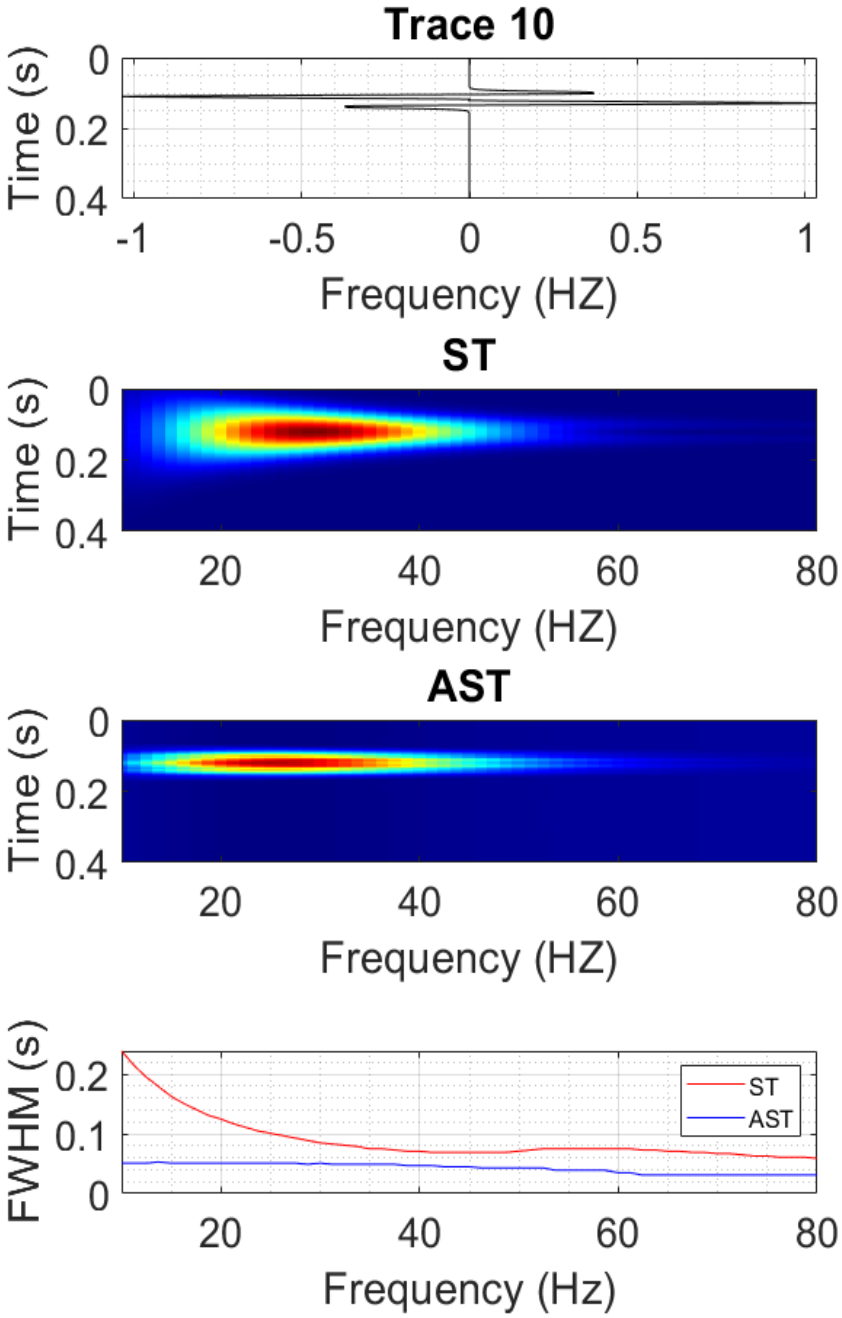

Figure 3.17: Comparison of full temporal width at half maximum (FWHM) as a function of frequency for the ST and AST. For the ST, the FWHM decreases as frequency increases, however, it is almost constant for the AST. This implies the AST has better temporal resolution at all frequencies especially lower frequencies.

3.7 Auxiliary S-transform for broadband seismic data

Recent technological developments have enabled the acquisition of broader bandwidth seismic data (Hill et al., 2006; Ten Krood et al., 2013). Traditional marine seismic acquisition produces data with a frequency range of about 8-80 Hz, however, broadband seismic data has frequencies ranging from about 2.5-200 Hz. The advantages of broader bandwidth seismic acquisition are that they produce higher-resolution seismic images, better signal penetration to greater depths, and better suitability for seismic inversion (Ten Krood et al., 2013). Low-frequency seismic waves travel to greater depths and are useful for imaging deep targets. They also give greater stability in seismic inversion. In addition, low-frequency shadows found below gas reservoirs have been used as a direct hydrocarbon indicator (Castagna et al., 2003). In the frequency resolution test performed in section (3.6), the data used was generated using a single wavelet with a peak frequency. It is useful to test the frequency resolution using broadband seismic data. I apply the Auxiliary S-transform to synthetic broadband seismic data in order to further investigate the frequency resolution, and investigate its applicability for low-frequency related studies. The synthetic broadband data is generated by respectively convolving a tuning wedge with a pair of reflectors with opposite polarity with three different Ricker wavelets with peak frequencies 20 Hz, 40 Hz, and 70 Hz. The seismic data generated from all three are then stacked together. Figure 3.18 shows the broadband seismic data generated and its amplitude spectrum. Figure 3.19 shows the three wavelets used in generating the broadband seismic data. Figures 3.20 and 3.21 compare the temporal and frequency resolution of the Auxiliary S-transform for the synthetic broad data to that of the S-transform. The Auxiliary S-transform improves on the temporal resolution of the S-transform at all frequencies. The resolution of the Auxiliary S-transform is the same as that of the S-transform, however, the S-transform spectrum is affected by interference which artificially boosts high frequencies. On the other hand, the Auxiliary S-transform spectrum better resembles the actual spectrum of the data and attenuates high frequencies faster. The Auxiliary S-transform is thus more suitable for low-frequency studies compared to the S-transform.

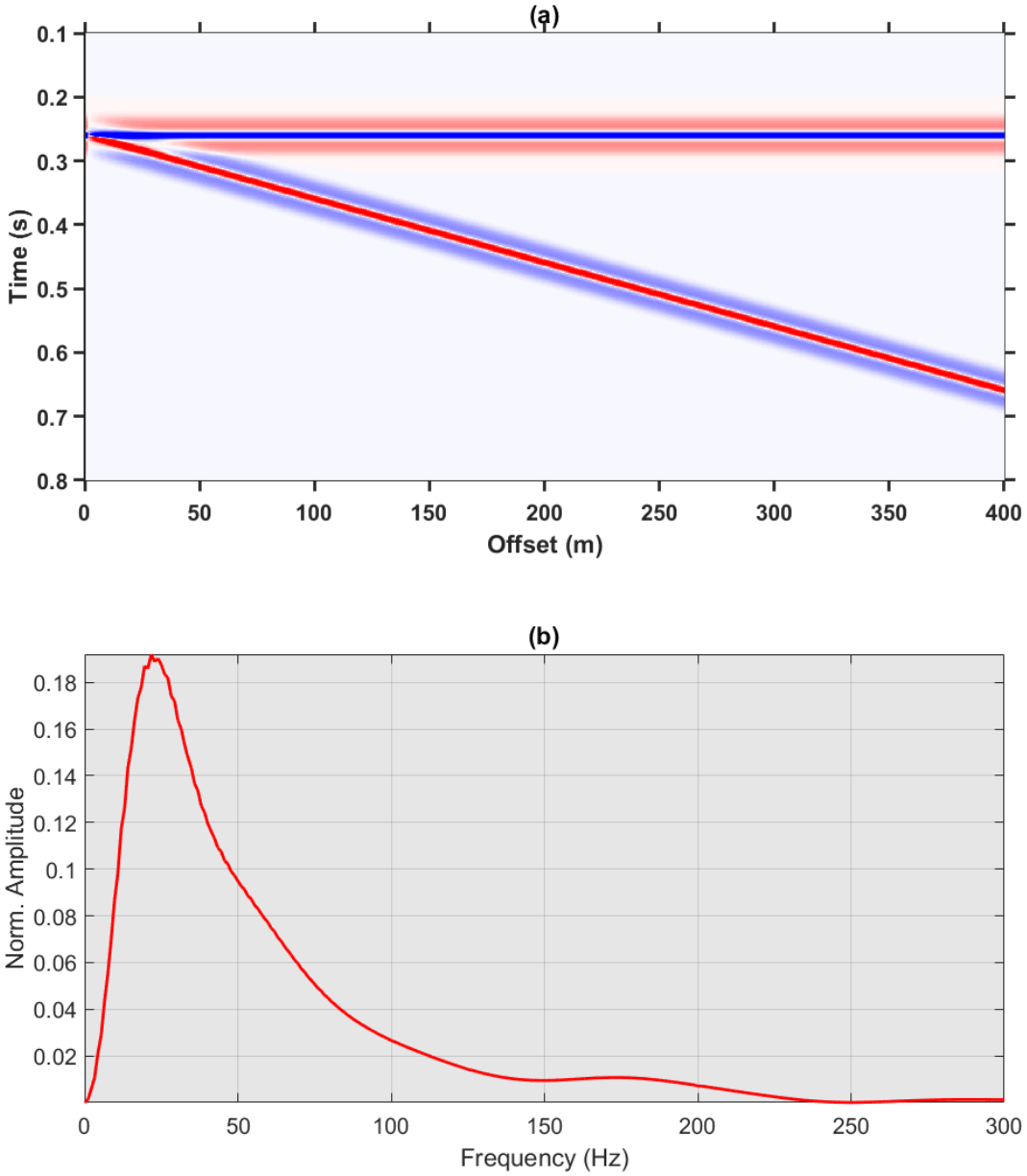

Figure 3.18: Stacked broadband synthetic seismic data generated by convolving a pair of reflectors with odd reflection coefficients with three Ricker wavelets of different frequencies (20 Hz, 40 Hz and 70 Hz).

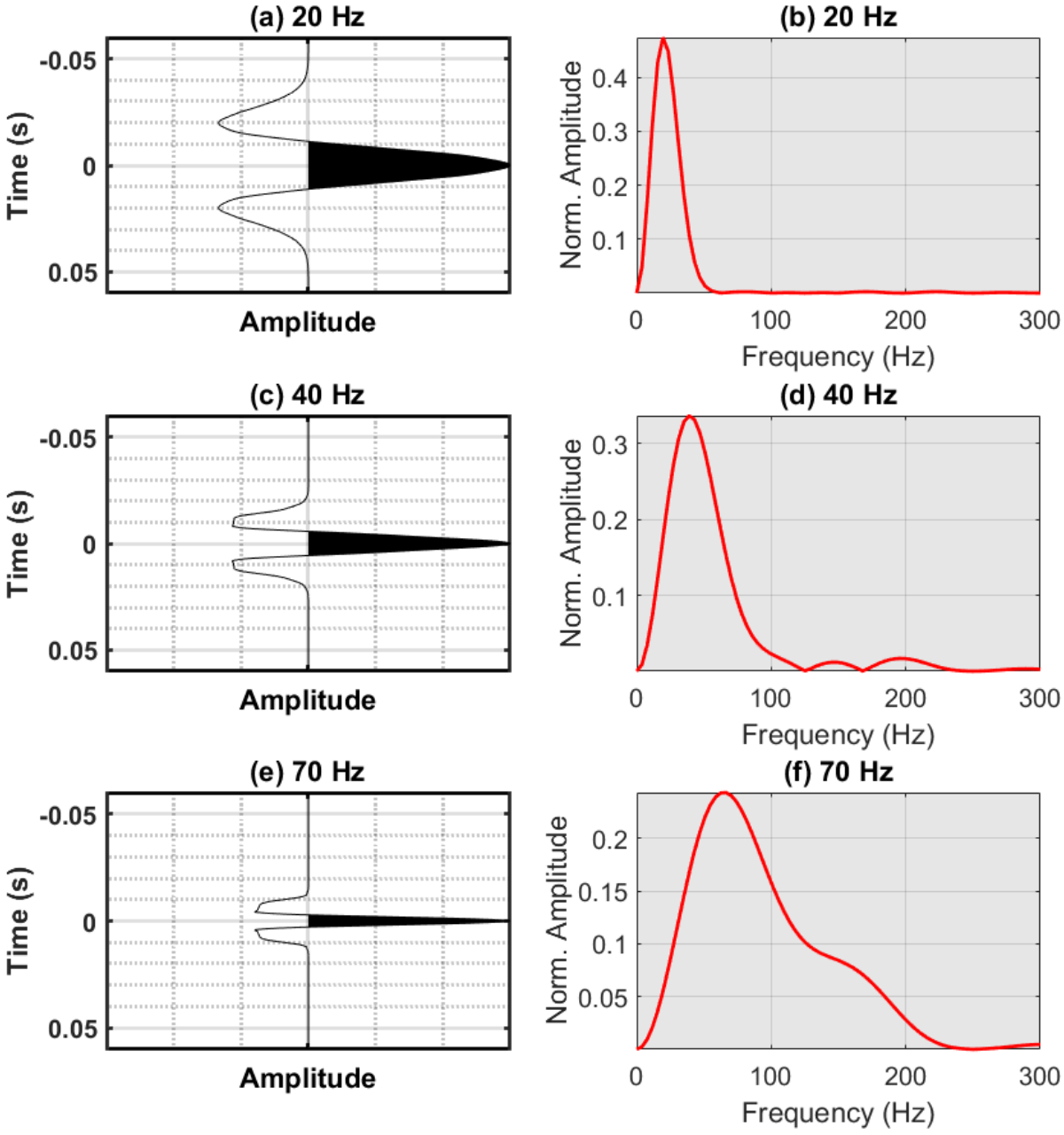

Figure 3.19: Three wavelets (20 Hz, 40 Hz, and 70 Hz) used in generating the synthetic seismic wedge in Figure 3.17.

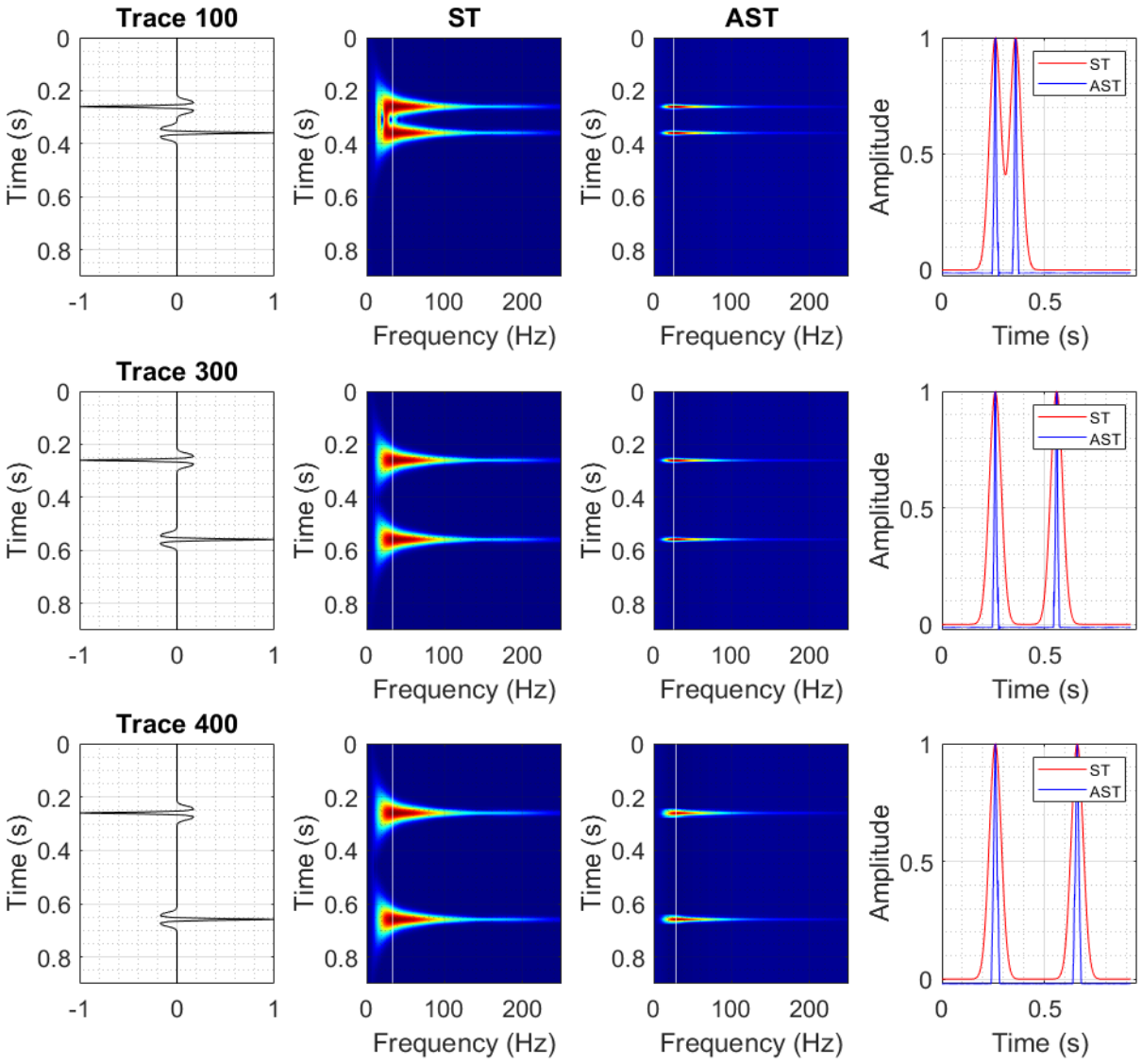

Figure 3.20: Comparison of the temporal resolution of the ST to that of the AST (99% PCF) at different trace locations extracted from the broadband synthetic wedge as the wedge separation increases. The second and third columns of panels show the time-frequency panels for the ST and AST respectively. The amplitudes shown in the fourth column of panels are extracted along the white lines.

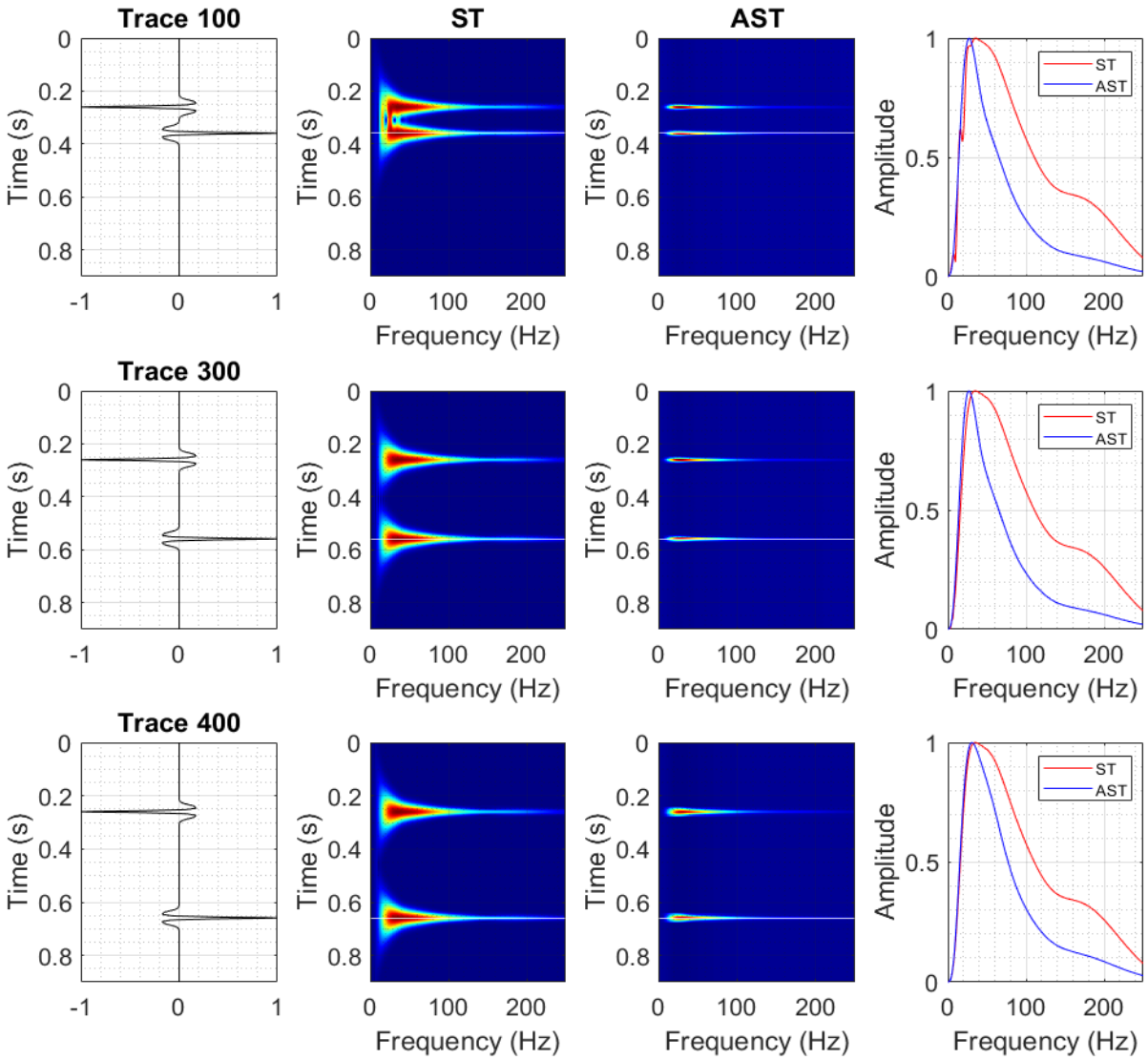

Figure 3.21: Comparison of the frequency resolution of the ST to that of the AST (99% PCF) at different trace locations extracted the broadband synthetic wedge as the wedge separation increases. The second and third columns of panels show the time-frequency panels for the ST and AST respectively. The amplitudes shown in the fourth column of panels are extracted along the white lines.

Some studies have documented the existence of low-frequency shadows below gas reservoirs (Taner et al., 1979; Castagna et al., 2003; Ebrom, 2004). While the phenomenon is not yet well understood, some hypotheses include reflection boosting due to tuning effects in gas reservoirs, the heterogeneous nature of reservoir zones, and wavelength-scale fluid flow (Chabyshova and Goloshubin, 2014) and high P-wave attenuation at low seismic frequencies (Korneev et al., 2004). A simple way to reproduce the LFS effect is to making use of reflection coefficients that vary as a function of frequency (Chen et al., 2016). To simulate the low-frequency shadows, I apply the Auxiliary S-transform to a tuning wedge overlaying a series of reflectors with frequency-dependent reflection coefficients. I generate broadband seismic data by respectively convolving three wavelets (20 Hz, 40 Hz, and 70 Hz) with the reflector geometry in Figure 3.22 and stacking the data. The reflection coefficient significantly reduces as the frequency increases below the reservoir, hence the high frequencies are attenuated below the reservoir. Figure 3.23 shows the disappearance of the shadows at high frequencies (75 Hz) for the Auxiliary S-transform and the S-transform. At high frequencies such as 60 Hz, the shadow disappears for the Auxiliary S-transform however, it is still slightly visible for the S-transform due to smearing in the frequency domain caused by interference. At 20 Hz, the Auxiliary S-transform better localizes the low-frequency shadows. Considering that the appearance of the low-frequency shadow is a combination of the properties of the reservoir and the properties of the rocks below, it may be useful to obtain well log and core data at the precise location where the low-frequency shadow occurs to further investigate the phenomenon. The Auxiliary S-transform is useful for temporal and therefore depth localization of the low-frequency shadows. Figures 3.24 and 3.25 compare the frequency and temporal resolution of the Auxiliary S-transform to that of the S-transform. The Auxiliary S-transform improves on the temporal resolution of the S-transform at all frequencies. The frequency resolution (Figure 3.24) indicates Auxiliary S-transform better images low-frequency phenomena.

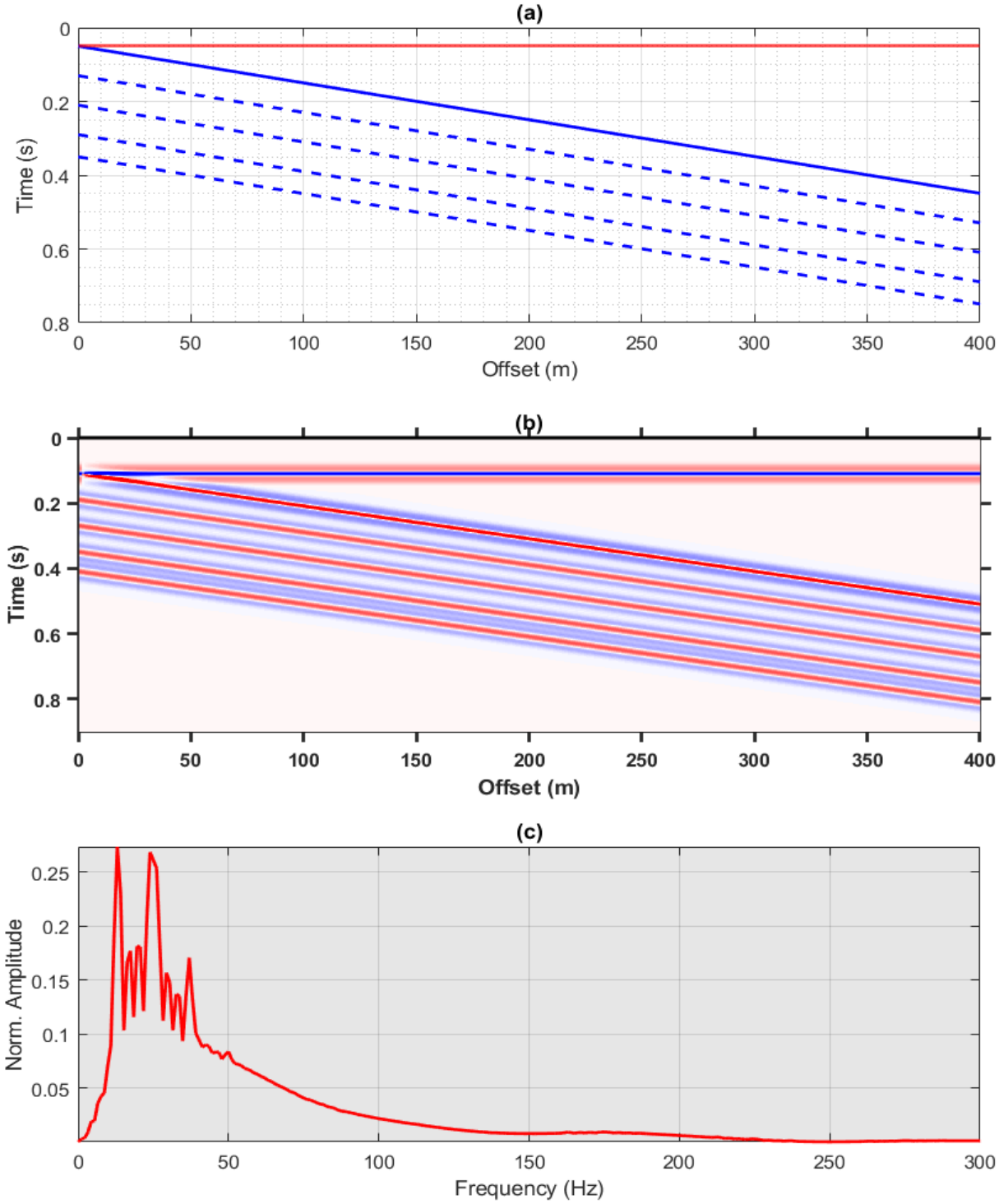

Figure 3.22: Generation of broadband synthetic data simulating the case of the low-frequency shadows (LFS) observed below some gas reservoirs.

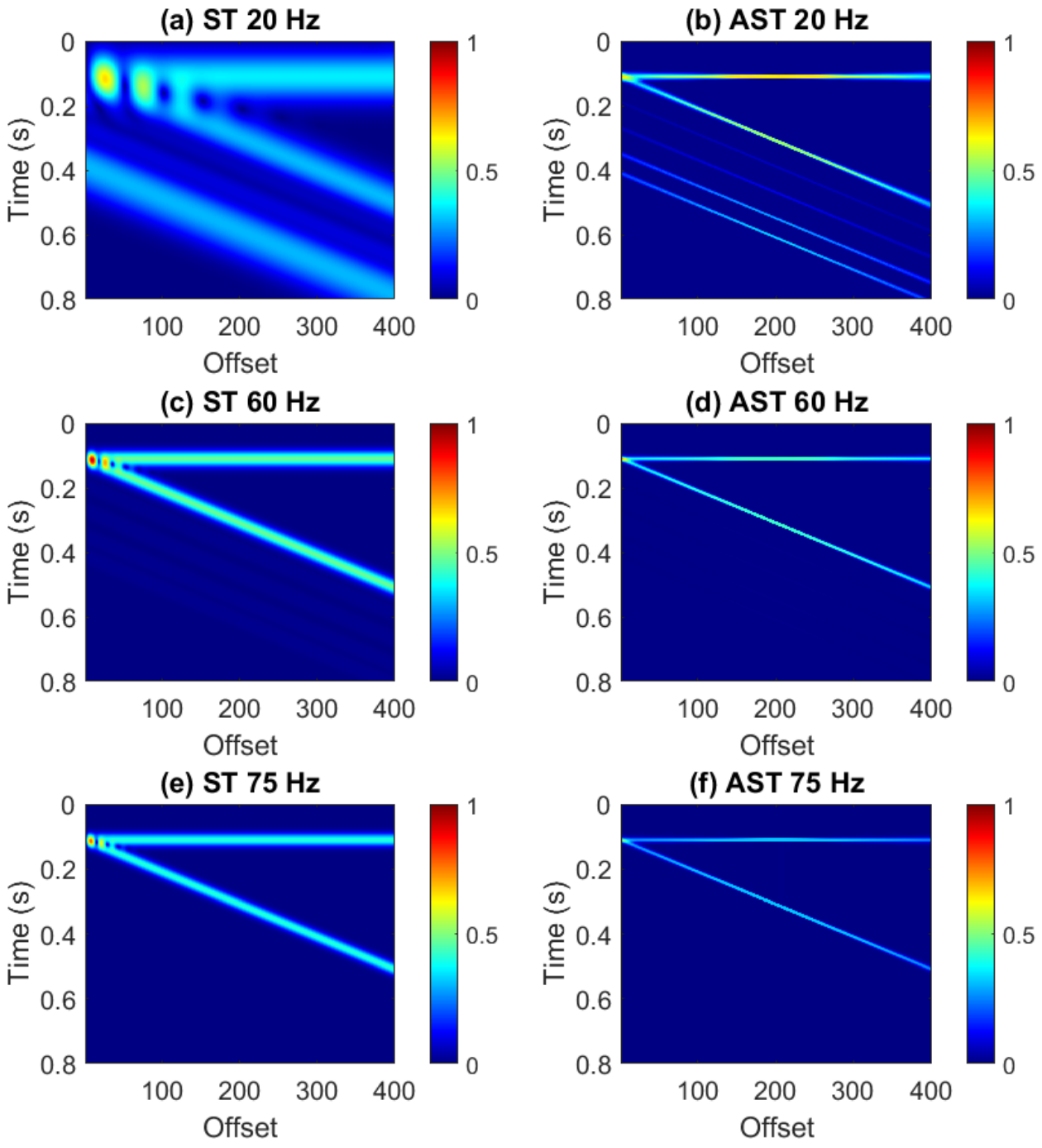

Figure 3.23: Comparison of the detection of the low-frequency shadow (LFS) for the ST and AST. The LFS appears on the 20 Hz panel but disappears at high frequencies. Due frequency smearing of the ST and better localization by the AST, the LFS completely disappears on the 60 Hz panel but is slightly visible for the ST.

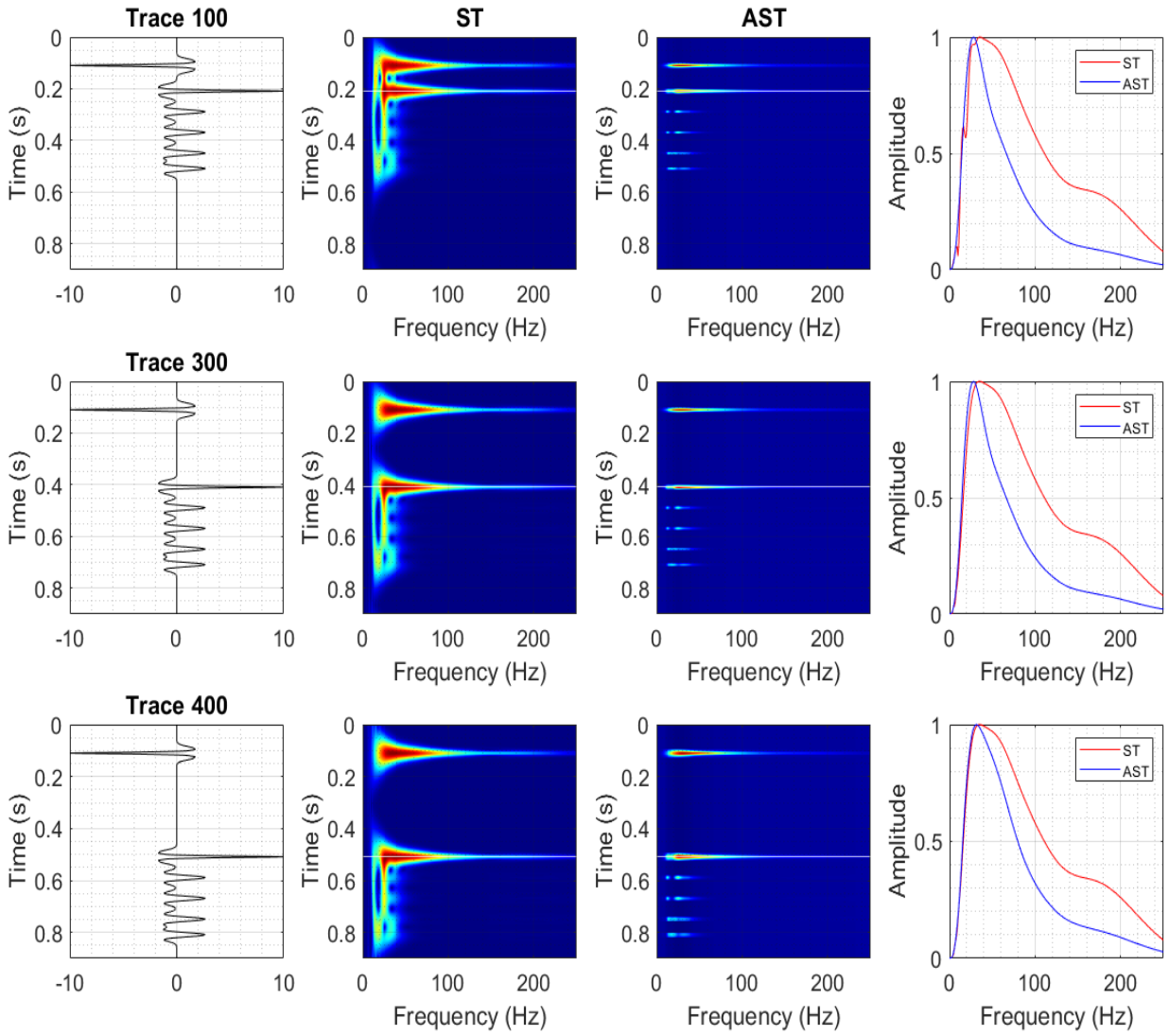

Figure 3.24: Comparison of the frequency resolution of the ST to that of the AST (99% PCF) at different trace locations for the case of a low-frequency shadow below a gas reservoir.

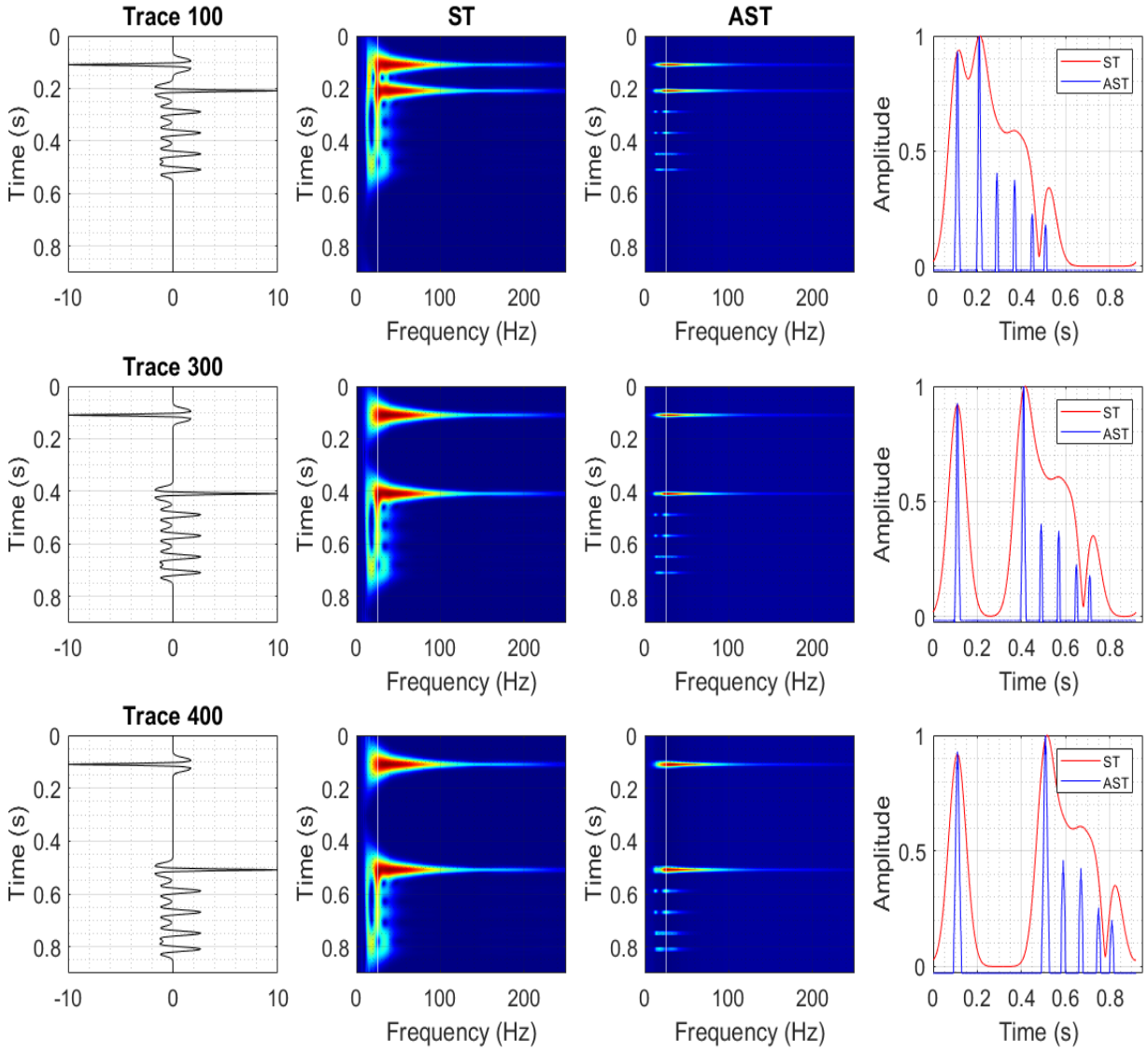

Figure 3.25: Comparison of the temporal resolution of the ST to that of the AST (99% PCF) at different trace locations for the case of a low frequency shadow below a gas reservoir.

3.8 Computational Cost of the Auxiliary S-transform

I measure and compare time for computing the Auxiliary S-transform to the S-transform (Figure 3.26) as the number of traces increases. The computer architecture used has an i7 Intel processor and 16 GB random access memory (RAM). The red bar shows the computational time for the traditional S-transform. The blue bar shows the computational time for the S-transform applied in the slowness domain. The black bar shows the computational time for both the forward and inverse Radon transforms. The green bar gives the computational time of the Auxiliary S-transform. It is equal to the sum of the black and blue bars. The Auxiliary S-transform is done in two steps, the Radon transform and the S-transform in the slowness domain. If the trajectory of the data doesn't change the number of traces in the slowness remains the same even though the number of offset traces increases. Hence the computational time for the S-transform in the slowness domain (blue bar) is almost constant. The computational time increase with the number of traces for the traditional S-transform and the Radon transform both. The resulting configuration is that before a certain number of traces (500 traces in this case), the Auxiliary S-transform takes more computational time than the Auxiliary S-transform; but as the number of traces increases further, the S-transform takes more computational time. The Auxiliary S-transform is thus more computationally efficient for large data seismic sets (as is the case in most seismic projects) compared to the S-transform while at the same time improving the resolution.

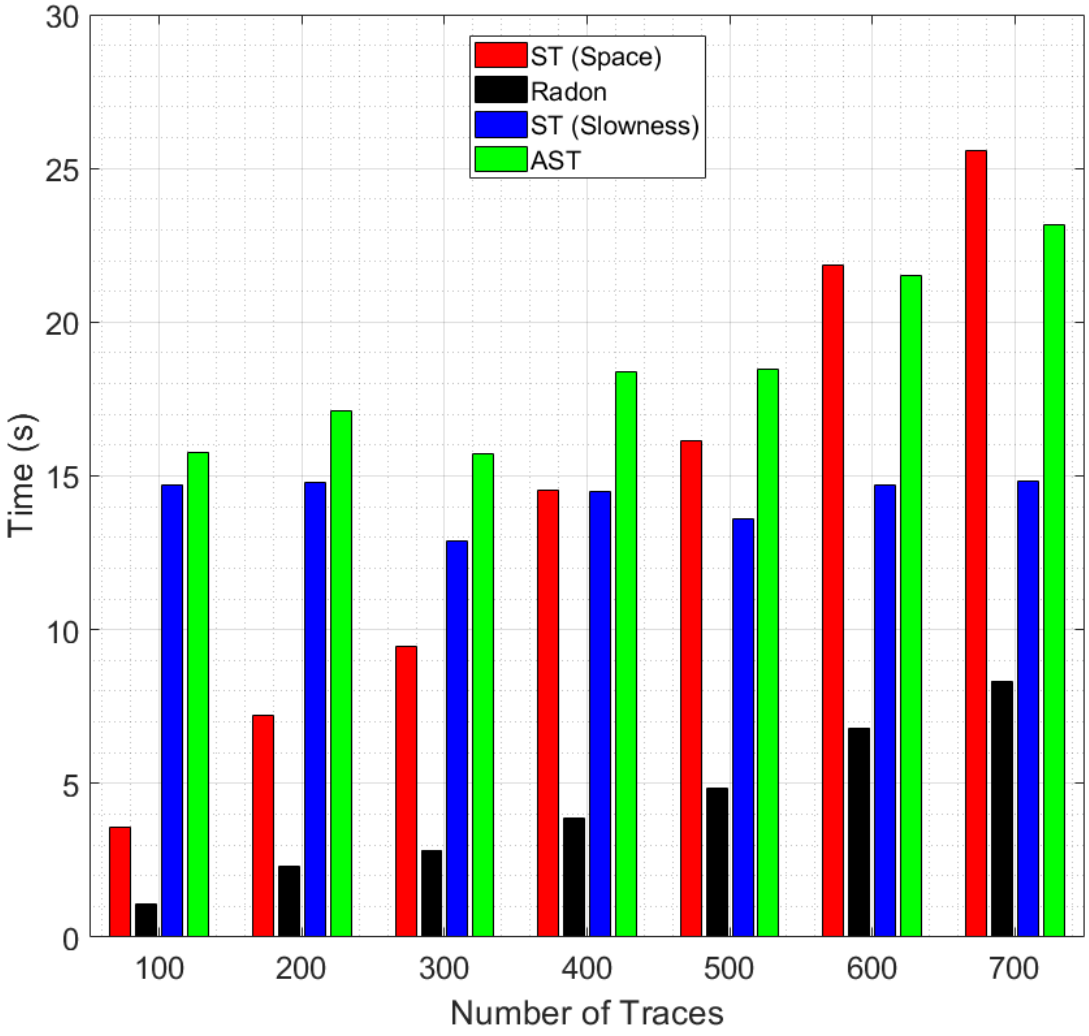

Figure 3.26: Computational cost of the AST and ST as a function of the number of traces.

3.9 Application to Real Seismic Data

The Auxiliary S-transform is applied to real seismic data from the F3 block, a 16 X 24 Km block, located offshore the Netherlands (Figure 3.27. In this area, shallow gas has been of interest because the gas can be a hazard and a risk when drilling a well, or choosing the site of an offshore platform at the seabed and may also indicate deeper hydrocarbon reserves (Schroot and Schuttenhelm, 2003). It is therefore important to accurately track the location of thin lateral shallow gas layers in the time/depth domain.

The North Sea basin is a sedimentary basin that was dominated by rifting during most of the Mesozoic, with acceleration in rifting activity at the transition from the Jurassic to the Cretaceous (Ziegler, 1990). Occasionally rifting or thermal subsidence was interrupted by compressional tectonic events, such as those related to the Alpine deformation (Schroot et al, 2005). The area is strongly disturbed by salt diapirs, which were active several times, from the Zechstein to the Paleogene periods (Remmelts, 1996). The Zechstein carbonate and salt formations serve as a seal for Lower Permian reservoirs. Several bright spots are found over salt domes in the area. Other features of interest include a Mid-Miocene unconformity, buried at depths ranging from 1000 to 1500 m and a complex fan delta system, prograding over the Mid-Miocene unconformity (Schroot et al., 2005).

Table (3.2) gives the stratigraphy of the study area. The data used in this study span the North Sea Group which was assembled in the Cenozoic. The North Sea Group is subdivided into the Paleogene Lower and Middle North Sea Groups, and Neogene Upper North Sea group. The depositional setting of the Lower and Middle North Sea groups are predominantly marine while the depositional setting of the Upper North Sea Group is shallow marine with terrestrial beds of a fluvial and lacustrine origin (Van Adrichem Boogaert and Kouwe, 1993). The Lower North Sea group is made up of grey sands, sandstones and clay; the Middle North Sea group consists of sands, silts, and clays while the Upper North Sea Group consists of clays and fine-grained to coarse-grained sands with gravel, peat, and brown coal seams (Van Adrichem Boogaert and Kouwe, 1993).

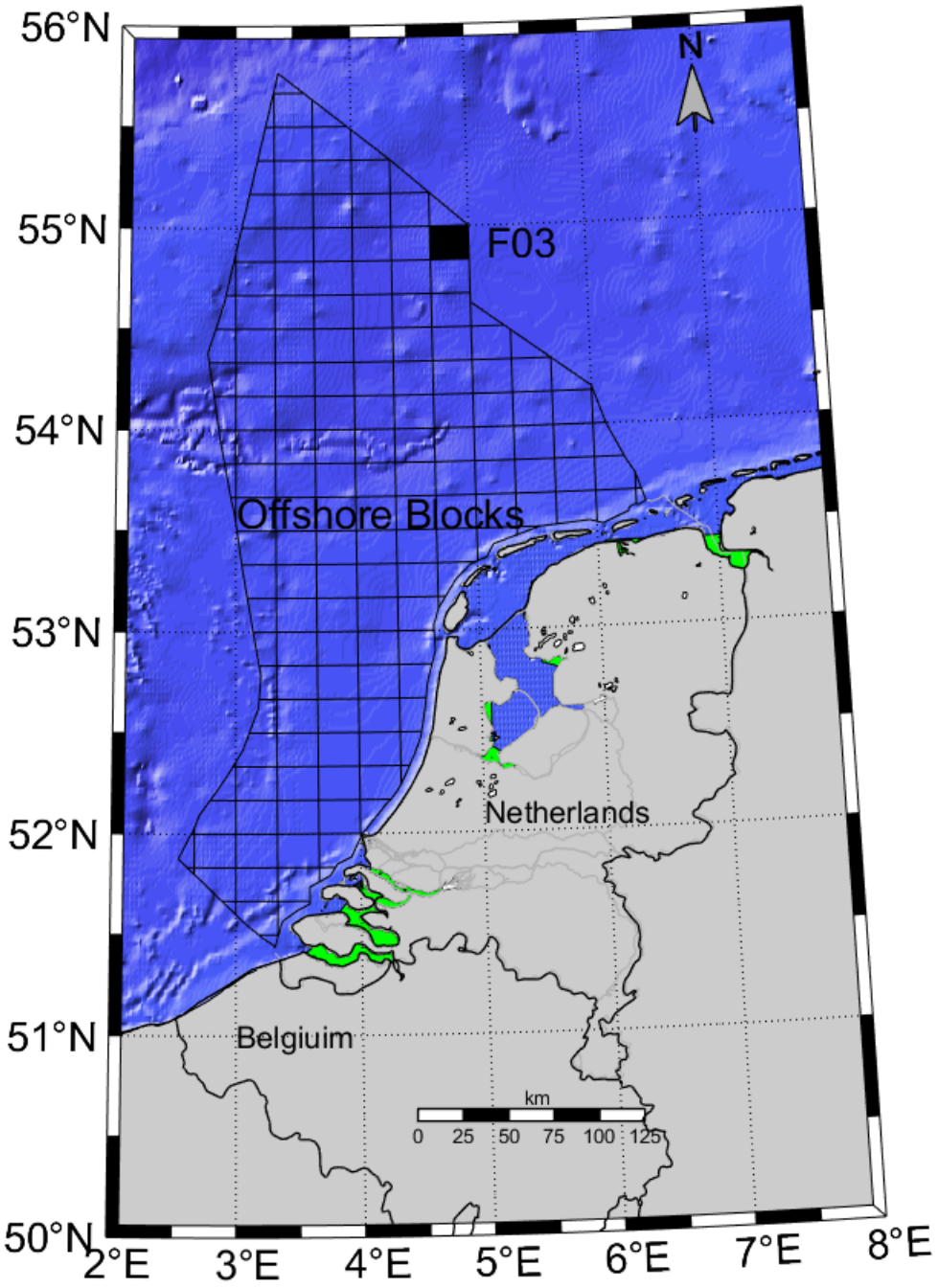

Figure 3.27: Location map of the study area, the F3 block, offshore the Netherlands.

Era	Period	Epoch	Lithographic units	Orogeny	Time (Ma)
CENOZOIC	Neogene	Pleistocene-Holocene	Upper North Sea Group	ALPINE	0
		Pliocene			
		Miocene			
	Paleogene	Oligocene	Middle North Sea Group		
		Eocene	Lower North Sea Group		
		Paleocene			62

Table 3.2: Stratigraphy of the the study area, modified from Van Adrichem Boogaert and Kouwe (1993).

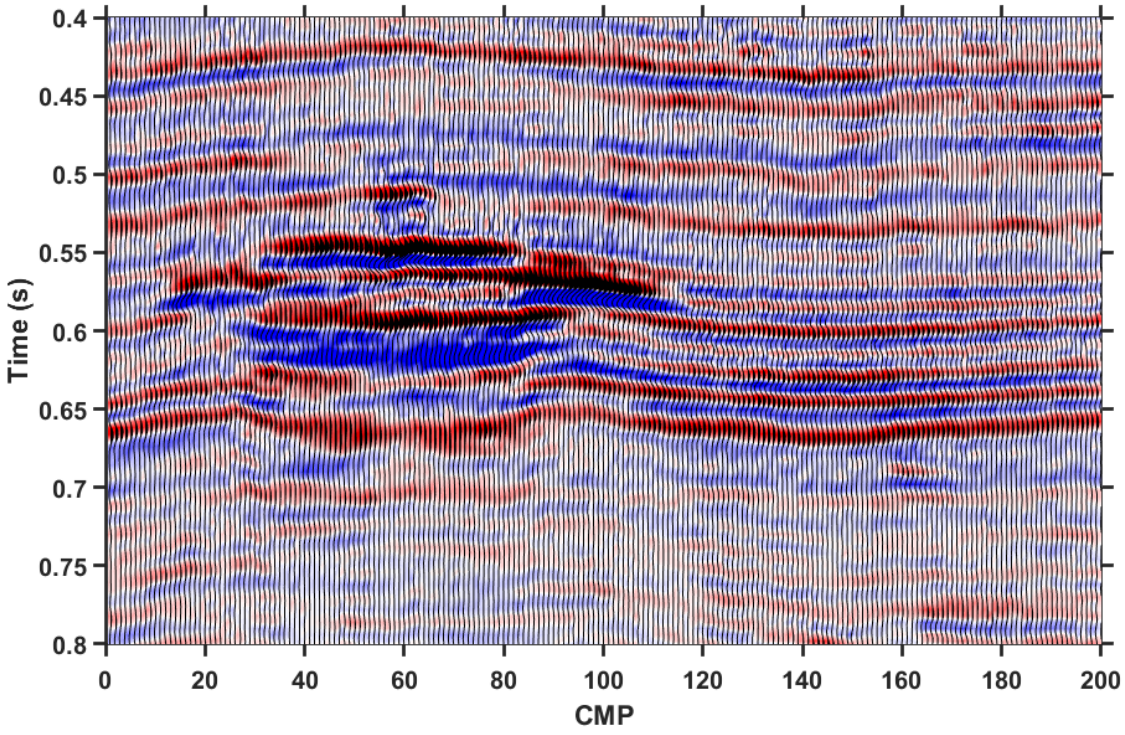

Figure 3.28: A composite seismic section from a 3D post-stack seismic dataset. The data is from block F3 of the Netherlands North Sea sector showing a bright spot over a flat spot.

Figure 3.28 shows a composite section that contains a bright spot over a flat spot corresponding to Upper Pliocene gas sands (Schroot et al., 2005). The configuration represents a sand layer containing hydrocarbons trapped between a shale layer on top, and brine sand below. The hydrocarbon sand has lower impedance than both the overlying shale and the brine sand while the brine sand has lower impedance than the overlying shale. The observed signal in the seismic data is a bright spot over a flat spot. There is a decrease in amplitude over the crest of the structure. The bright spot corresponds to the shale-hydrocarbon contact and the flat spot corresponds to the hydrocarbon-brine contact. I apply the Auxiliary S-transform to the seismic section in Figure 3.28. Figure 3.29 shows the comparison of the ST and the AST at different frequencies (10 Hz, 60 Hz, and 75 Hz). The Auxiliary S-transform successfully captures the shape of the structural traps more accurately than the S-transform and shows a significant improvement in the temporal resolution compared to S-transform for all frequencies. Figure 3.30 shows a comparison of the Auxiliary S-transform with linear and parabolic trajectories to the S-transform at low and high frequencies. The Auxiliary S-transform for both cases demonstrates significantly better temporal resolution than the S-transform and better resolves structure of the bright spot. The Auxiliary S-transform with linear and parabolic trajectories produce similar imaging results.

I apply the Auxiliary S-transform to a 3D volume of the data ranging from crossline 655 to 730 and inline 500 to 700. I create single frequency volumes, obtain time slices at different depths and compare the performance of the S-transform to that of the Auxiliary S-transform. Figures 3.31 shows a time slice passing through the bright spot. Figure 3.31a shows a time slice of the seismic data. Figures 3.31b, d and f show S-transform images of the time slice at 10 Hz, 30 Hz and 60 Hz respectively while Figures 3.31c, e and g show the Auxiliary S-transform images of the time slice at 10 Hz, 21 Hz, and 60 Hz respectively. The Auxiliary S-transform demonstrates better localization of the bright spot.

Figures 3.32, 3.33, 3.34, 3.35, and 3.36 show time slices of the seismic data ranging from 0.87s to 0.89s and several single-frequency panels (21 Hz, 30 Hz, 78 Hz) imaged using the S-transform and Auxiliary S-transform. The Auxiliary S-transform is able to image a complex network of

meandering channels, indicated with white arrows, which are not visible on the original seismic data and on the S-transform images. The channel is better imaged at high frequencies. This demonstrates the better performance of the Auxiliary S-transform and its ability to better image coherent signals compared to the S-transform.

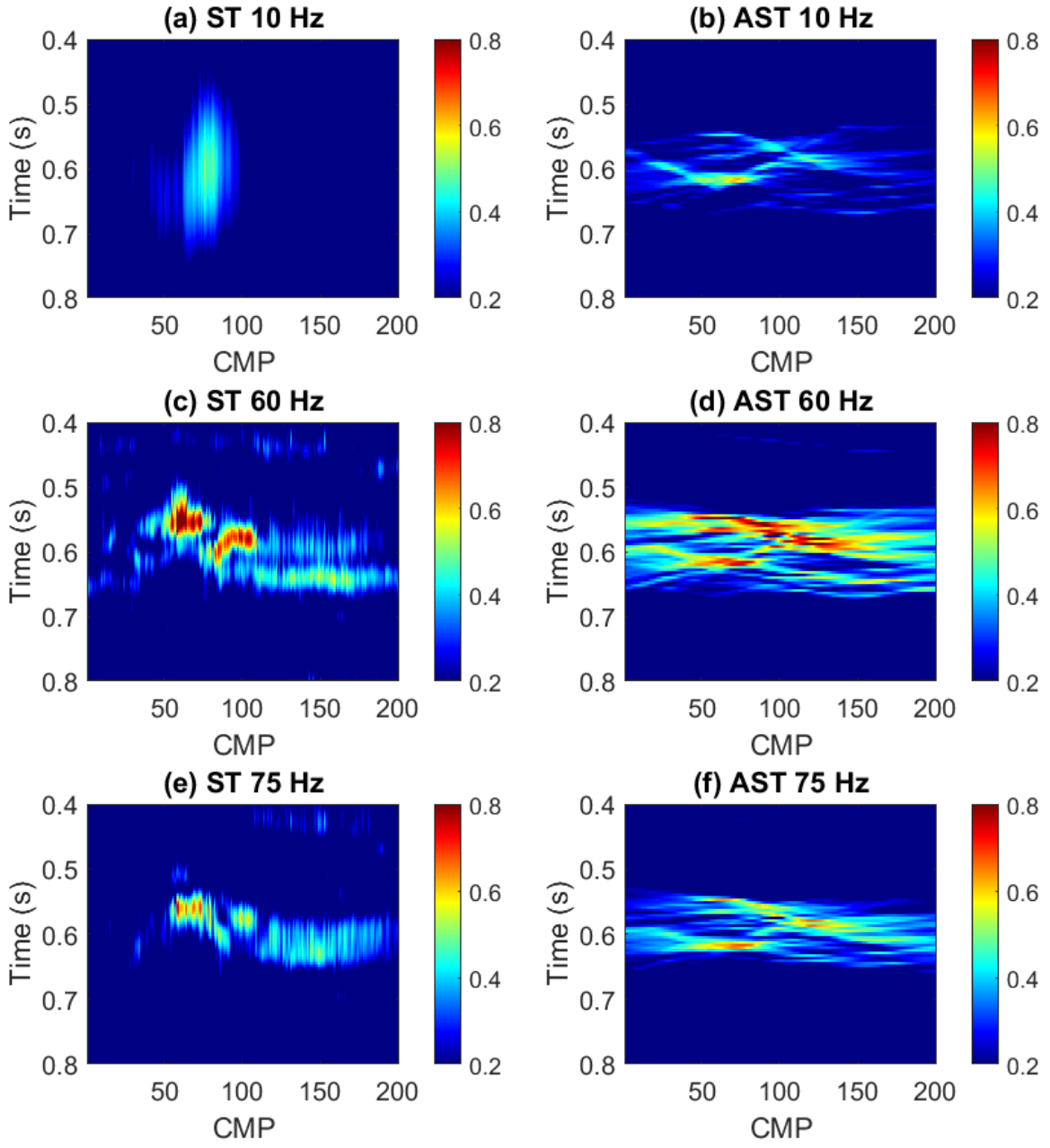

Figure 3.29: Comparison of ST and linear AST for the composite 2D section from the F3 block at different frequencies. The AST better images the bright spot over a flat spot structure.

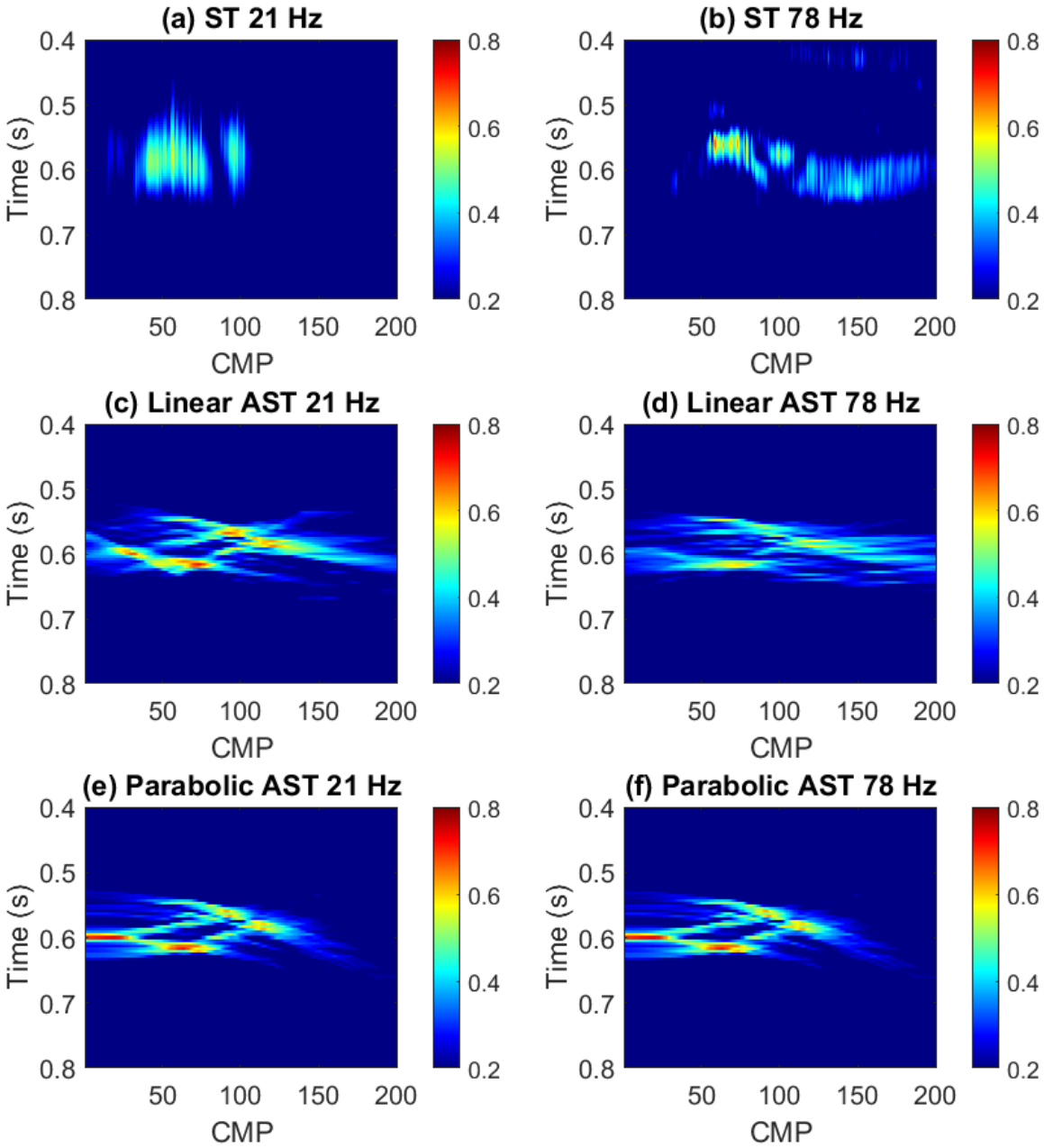

Figure 3.30: Comparison of ST and linear AST and parabolic AST for the composite 2D section from the F3 block at low and high frequencies. The AST better images the bright spot over a flat spot structure.

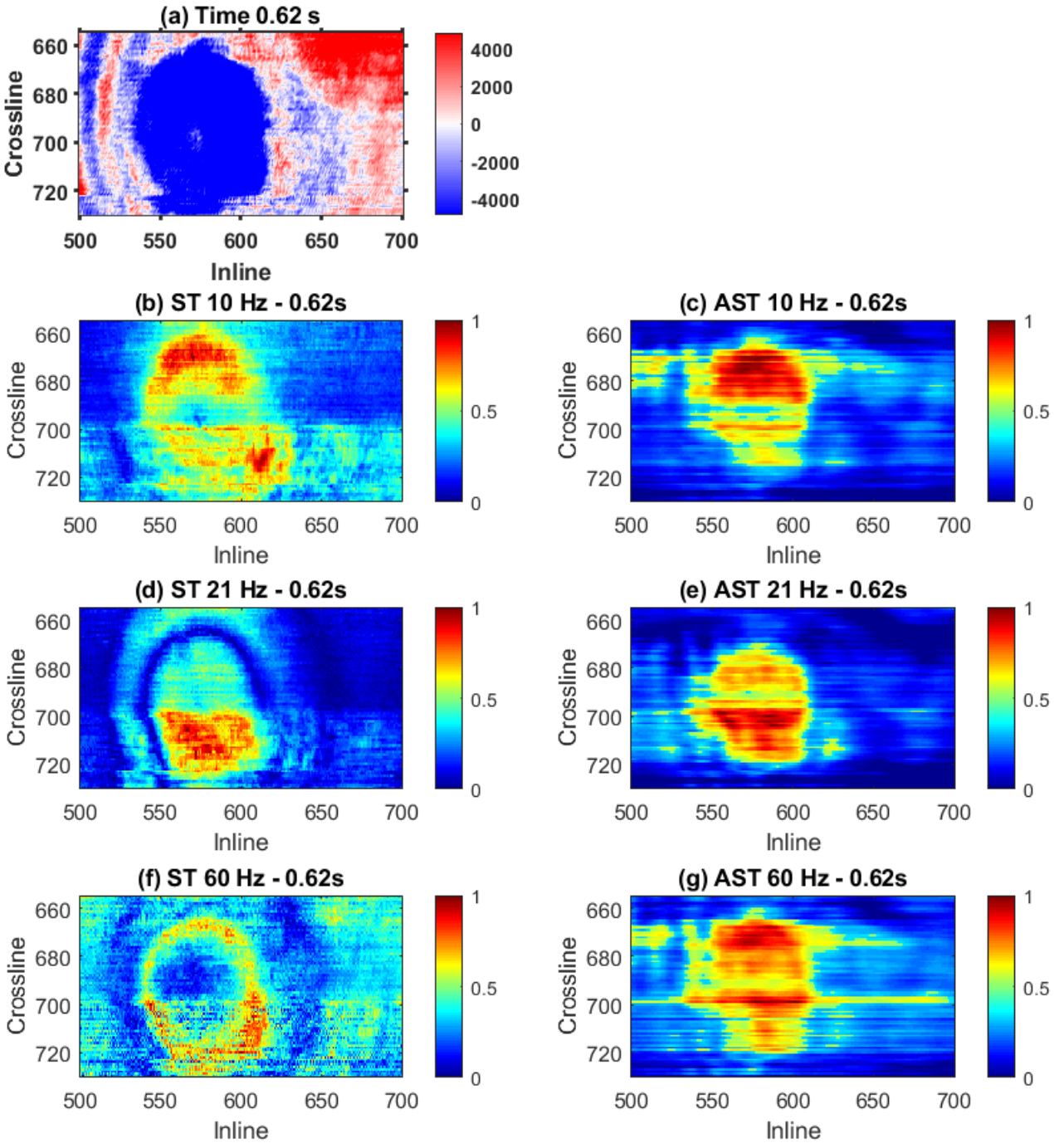

Figure 3.31: Time slice at 0.62 s. a) Time slice of the seismic data. b), d), and f) show ST images of the time slice at 10 Hz, 21 Hz, and 60 Hz respectively. c), e), and g) show AST images of the time slice at 10 Hz, 21 Hz and 60 Hz respectively. The AST is able to detect a complex network of channels (indicated by the white arrow).

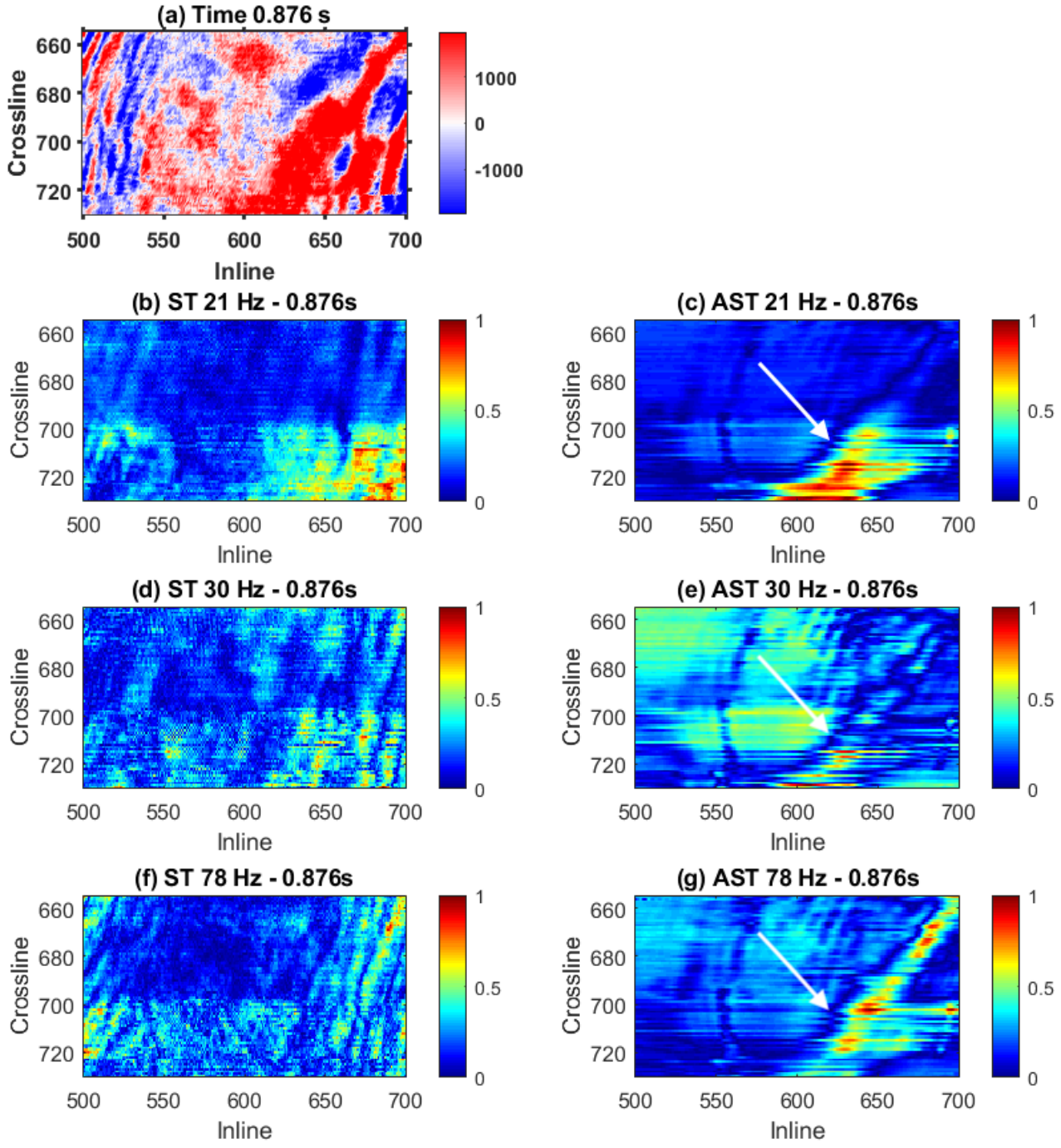

Figure 3.32: Time slice at 0.876 s. a) Time slice of the seismic data. b), d), and f) show ST images of the time slice at 21 Hz, 30 Hz, and 78 Hz respectively. c), e), and g) show AST images of the time slice at 21 Hz, 30 Hz, and 78 Hz respectively. The AST is able to detect a complex network of channels (indicated by the white arrow).

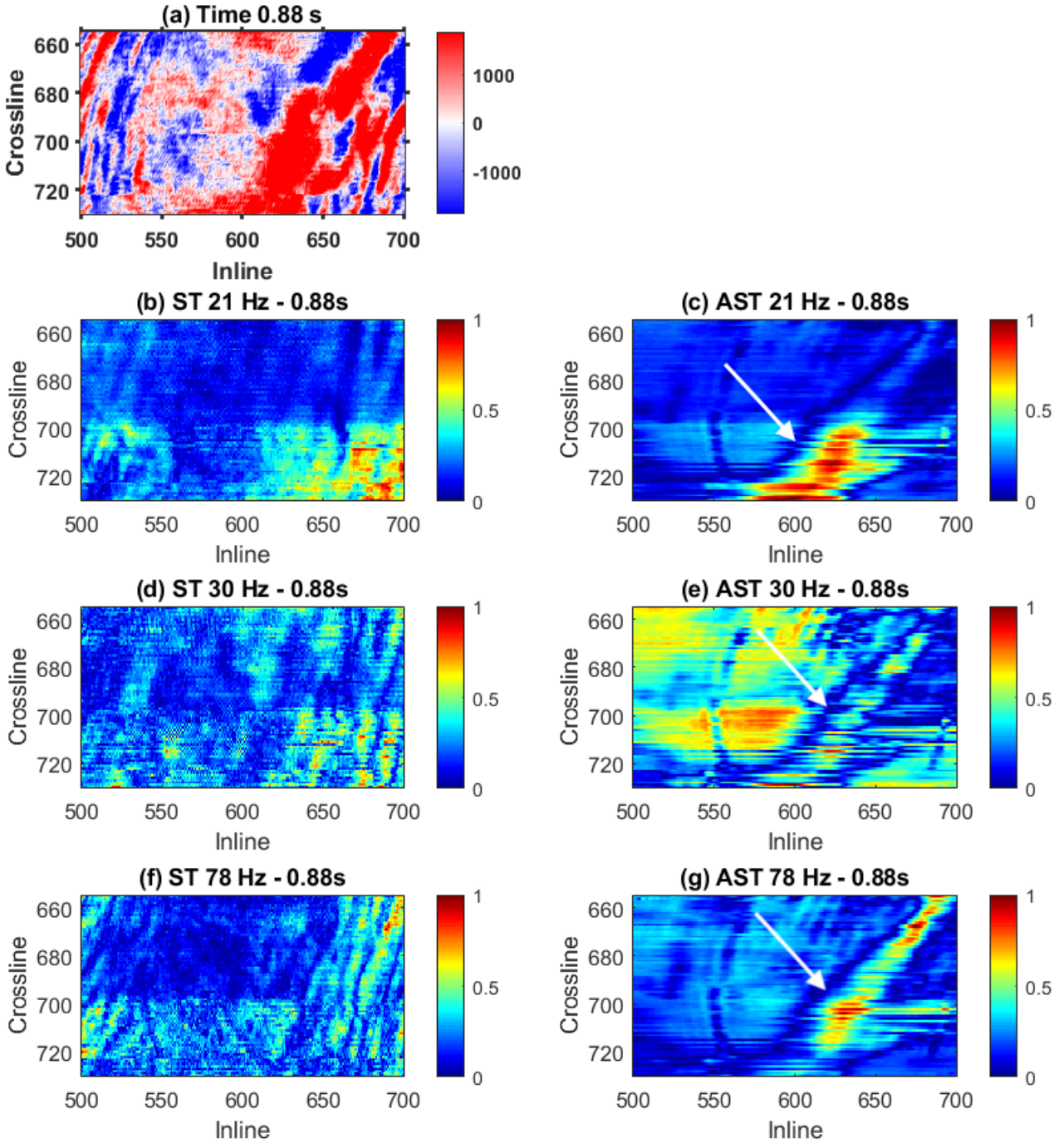

Figure 3.33: Time slice at 0.88 s. a) Time slice of the seismic data. b), d), and f) show ST images of the time slice at 21 Hz, 30 Hz, and 78 Hz respectively. c), e), and g) show AST images of the time slice at 21 Hz, 30 Hz, and 78 Hz respectively. The AST is able to detect a complex network of channels (indicated by the white arrow).

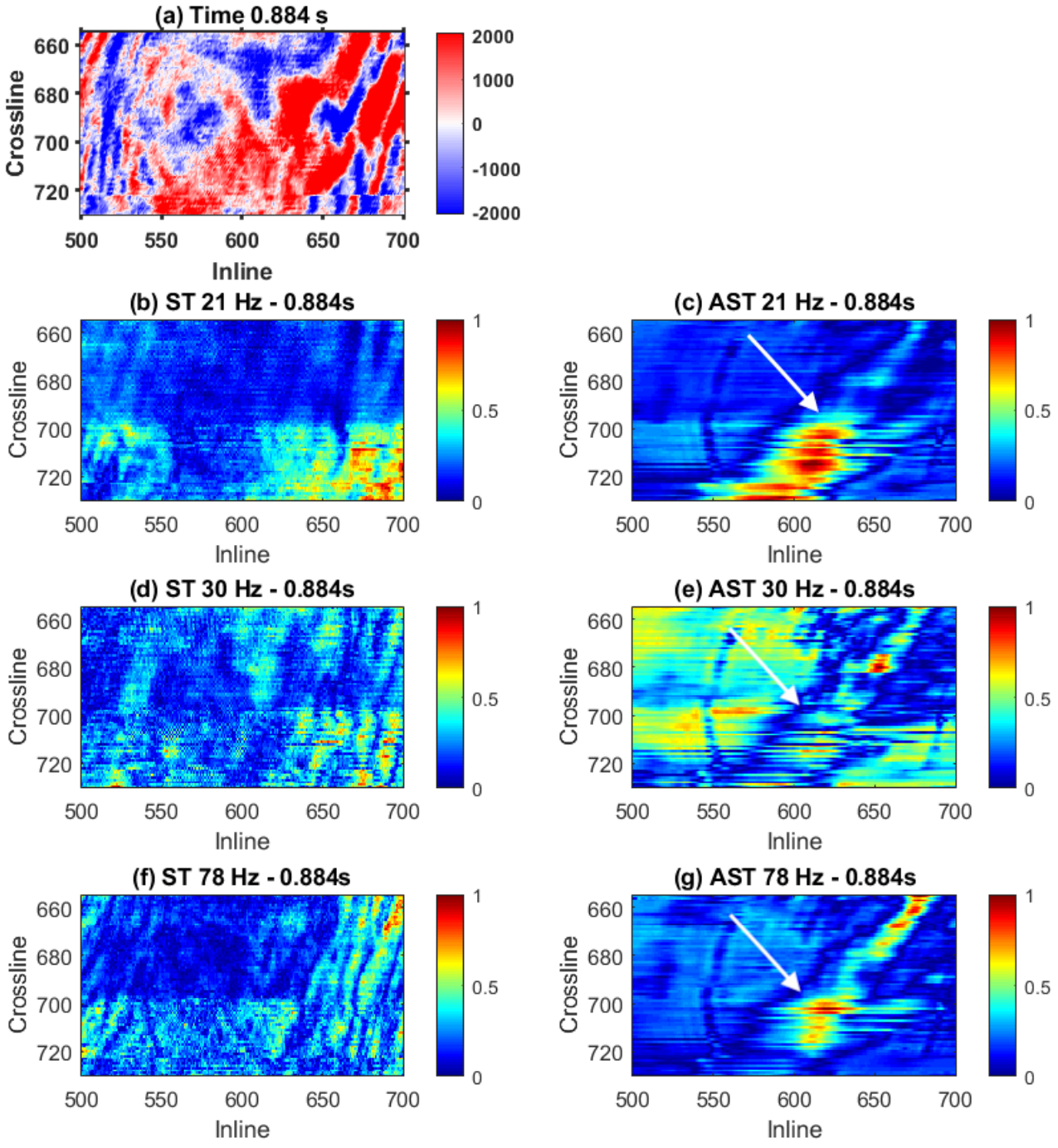

Figure 3.34: Time slice at 0.884 s. a) Time slice of the seismic data. b), d), and f) show ST images of the time slice at 21 Hz, 30 Hz, and 78 Hz respectively. c), e), and g) show AST images of the time slice at 21 Hz, 30 Hz, and 78 Hz respectively. The AST is able to detect a complex network of channels (indicated by the white arrow).

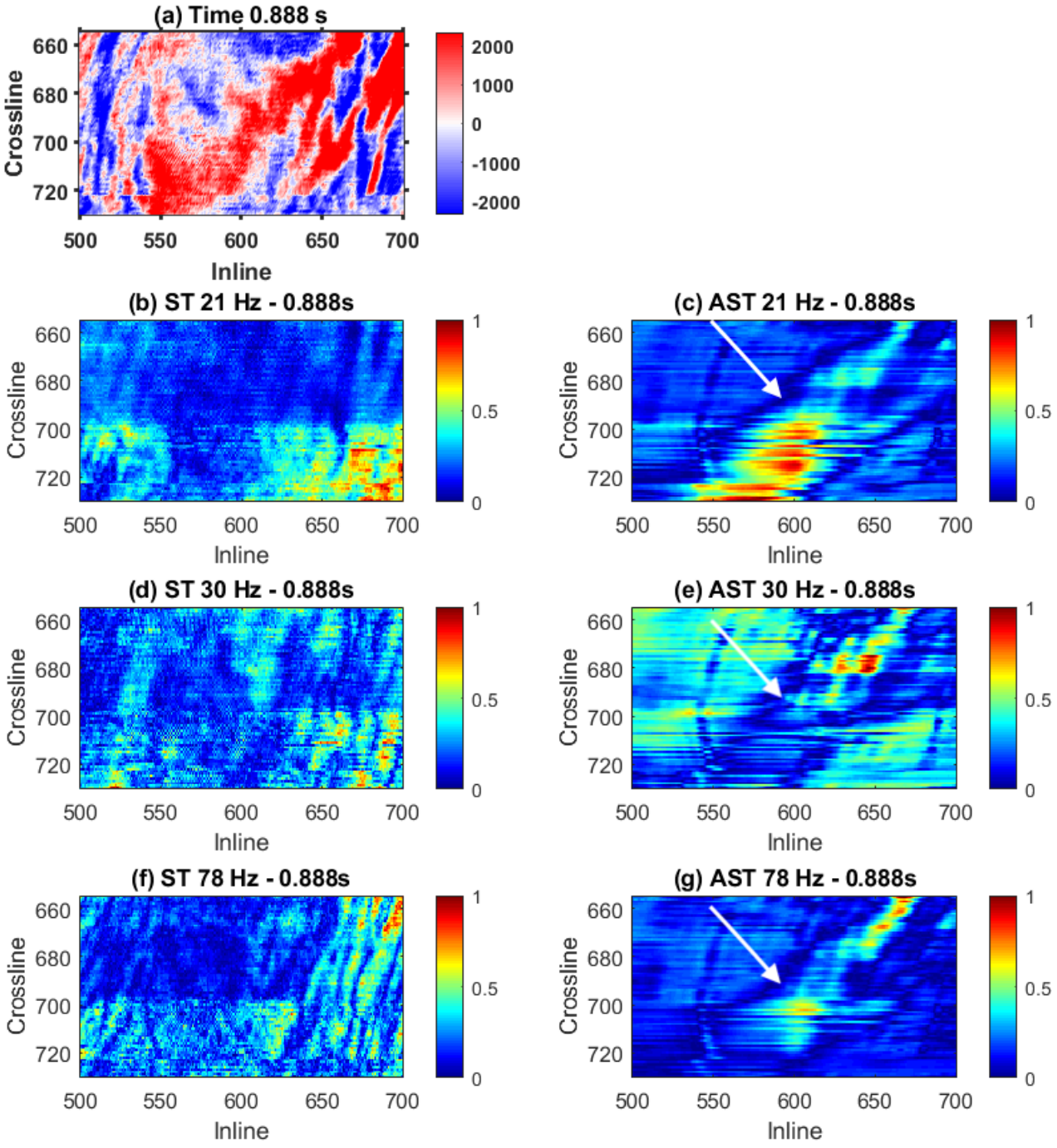

Figure 3.35: Time slice at 0.888 s. a) Time slice of the seismic data. b), d), and f) show ST images of the time slice at 21 Hz, 30 Hz, and 78 Hz respectively. c), e), and g) show AST images of the time slice at 21 Hz, 30 Hz, and 78 Hz respectively. The AST is able to detect a complex network of channels (indicated by the white arrow).

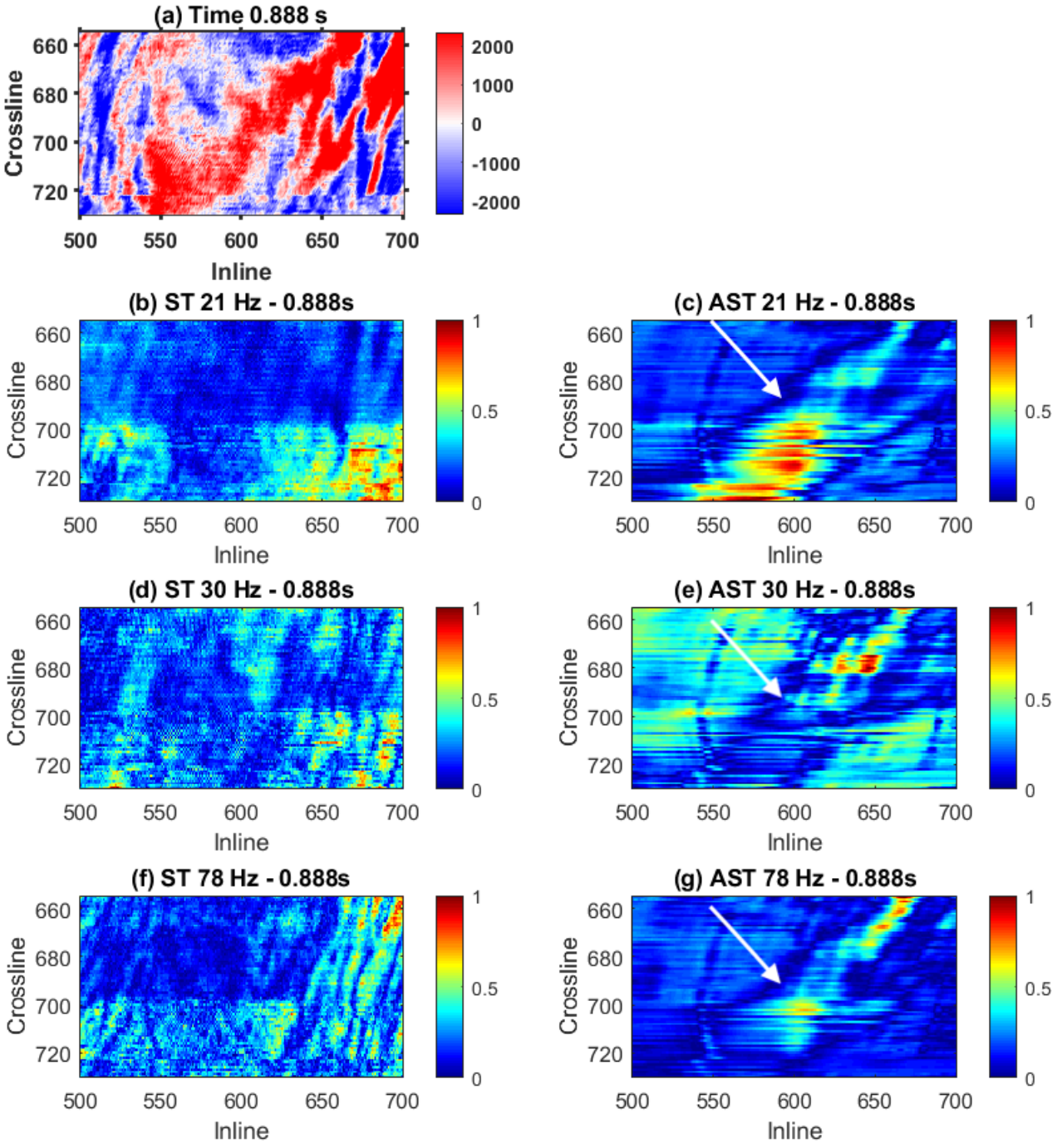

Figure 3.36: Time slice at 0.892 s. a) Time slice of the seismic data. b), d), and f) show ST images of the time slice at 21 Hz, 30 Hz, and 78 Hz respectively. c), e), and g) show AST images of the time slice at 21 Hz, 30 Hz, and 78 Hz respectively. The AST is able to detect a complex network of channels (indicated by the white arrow).

3.10 Conclusion to Chapter 3

This chapter presents the Auxiliary S-transform, a novel method for spectral decomposition of seismic data. The Auxiliary S-transform is an invertible spectral decomposition method that takes into account velocity and multi-trace coherency information in performing spectral decomposition of seismic data. It achieves this by mapping the data into the time-frequency-slowness or the time-frequency-curvature domain, where seismic events are better separated. The resolution of the inverted image can be improved by applying a percentile coherency filter in this domain. The Auxiliary S-transform incorporates the Radon transform into the spectral decomposition process. While the Radon transform is affected by smearing artifacts, the effects of the artifacts can be reduced by applying the percentile coherency filter while simultaneously increasing the separation between coherent seismic events in the time-frequency-slowness or the time-frequency-curvature domain. The choice of trajectory path used in the Radon transform may also reduce smearing effects.

Performance evaluation of the Auxiliary S-transform compared to the S-transform, indicates the new method improves on the temporal resolution at all frequencies. The resolution properties of the Auxiliary S-transform indicate its suitability for reservoir volume estimation. In general, the Auxiliary S-transform preserves the frequency resolution of the S-transform. For broadband seismic data, the Auxiliary S-transform is not affected by interference which artificially boosts high frequencies as is the case for the S-transform. The Auxiliary S-transform is thus more suitable for low-frequency studies and direct hydrocarbon indication than the S-transform. The Auxiliary S-transform is applied to real seismic data from the F3 block offshore the Netherlands. The method successfully images a complex network of meandering channels not visible in the original seismic data or detectable by the S-transform.

4. A QUANTITATIVE PROBABILISTIC FRAMEWORK FOR ESTIMATING THE CRITICAL MOMENT IN A PETROLEUM SYSTEM

4.1 Introduction, Definition and Statement of Problem

The petroleum system is a unifying concept that spans all the disparate elements and processes of petroleum geology including all pods of active source rock and all genetically related oil and gas accumulations, shows and seeps (Magoon and Dow, 1994). The essential elements of the petroleum system are the source rock, the reservoir rock, the seal rock, and the overburden rock while the processes are trap formation and generation-migration-accumulation of petroleum. These essential elements and processes have to be arranged in the right temporal order and the system has to be subjected to the right temperature conditions for petroleum generation to take place. Three important time concepts associated with the petroleum system are the age of the petroleum system, the critical moment and the preservation time (Magoon and Beaumont, 1999). The age or duration of the petroleum system is the time required to deposit the essential elements plus the time required for the processes of generation-migration-accumulation of petroleum. The critical moment is the point in time that best depicts the generation-migration-accumulation of petroleum. At the critical moment, about 50% to 90% of the petroleum is generated and expelled. Technically, it is the point in time with the highest probability for generation-migration-accumulation of petroleum to take place. It is best estimated using vitrinite reflectance data together with burial history and thermal history data of the essential elements of the petroleum system and it often occurs when the source rock is at or near the depth of maximum burial. In many cases, these data are unavailable, unreliable or incomplete or there is a high degree of uncertainty associated with them because of uplift and erosion. This uncertainty translates to risk in petroleum exploration assessment because the stratigraphic and geographic extents of the petroleum system are constructed at the critical mo-

Parts of this chapter have been published in the American Association of Petroleum Geologists (AAPG) Bulletin, (Amosu and Sun, 2019)

ment. It is therefore important to determine the critical moment in a quantitative manner within a probability-based framework and to quantify the uncertainty in its determination. The preservation time starts after the process of generation-migration-accumulation is complete and continues till present day. A petroleum system is named by combining the source rock name, the major reservoir rock name and one of three levels of uncertainty: speculative (?), hypothetical (.) or known (!). The level of uncertainty indicates the level of confidence one has that the petroleum in an accumulation came from the source rock specified in the name. In a known petroleum system, a geochemical match exists between the source rock and hydrocarbon accumulations; in a hypothetical petroleum system, geochemical data identifies the source rock but lacks a geochemical match to hydrocarbon accumulations; while in a speculative petroleum system, the existence of source rocks is only postulated on the basis of petroleum (Magoon [1992]). A quantitative probabilistic estimation of the critical moment is useful for all categories of petroleum systems.

To better illustrate the concept of a petroleum system, Magoon and Dow (1994) presented a useful example of a fictitious petroleum system called the Deer-Boar(.). Figure 4.1 shows the stratigraphic and geographic configuration of the elements of the Deer-Boar(.) at the critical moment. A line encompassing the pod of active source rock and all petroleum accumulations defines the geographic extent. The stratigraphic extent of the petroleum system contains all lithological units, which encompass the essential elements within the geographic extent of the petroleum system.

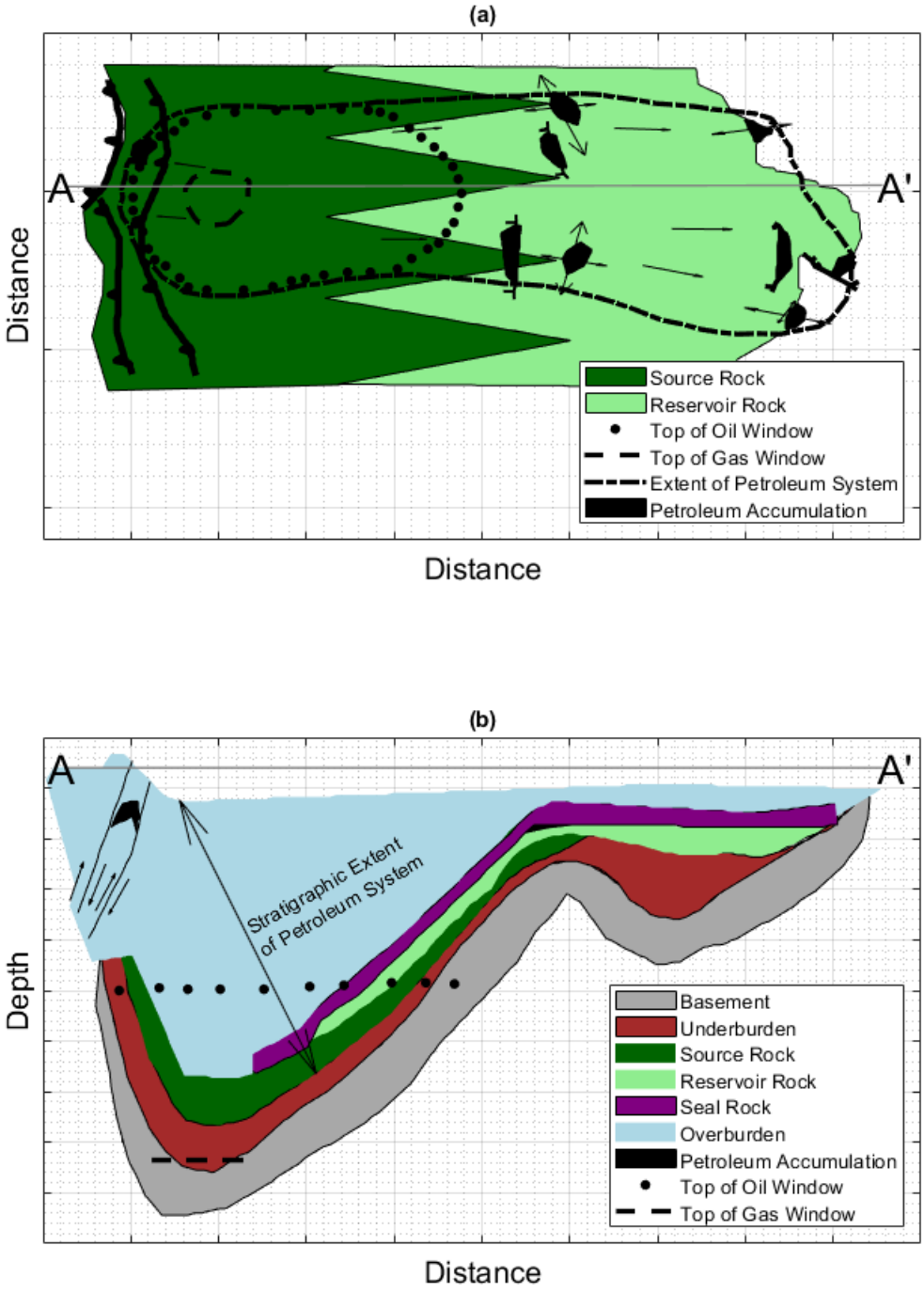

Figure 4.1: Geographical and stratigraphic extent of the Deer-Boar(.) petroleum system. A-A' is location of cross-section. A line encompassing the pod of active source rock and all petroleum accumulations defines the geographic extent. The stratigraphic extent encompasses all essential elements and stratigraphic units within the geographic extent of the petroleum system. Modified from Magoon and Dow (1994).

4.2 Quantitative Probabilistic Framework

The petroleum system can be investigated using different types of data including geochemical data, spatial geographic data, and temporal stratigraphic data. Commonly used charts and table are the burial history chart, table of hydrocarbon accumulations, the petroleum system map and cross-section at the critical moment and the events chart. The quantitative probabilistic framework will focus on the events chart in order to estimate the timing of the critical moment; data relating to the timing of generation-migration-accumulation and preservation can be included in the events chart as well. Sequence stratigraphic studies can be used to constrain the timing of the events and processes (see Amosu and Sun, 2017 a, b). In an events chart, the x-axis usually represents geologic time (usually measured in mega-annum time units: Ma); the essential elements and processes are arranged in a column in order of increasing difficulty and the known time range of occurrence of each is plotted. In addition, the critical moment and preservation time are included.

The essential elements and processes have to be present in order to have a viable petroleum system. The quantitative probabilistic framework aims to estimate the probability for each moment in time using data of the timing of the essential elements and processes, i.e. I will calculate the probability as a function of time. The probability of the critical moment occurring generally increases after the occurrence of each essential element or process. There are four stages involved:

1. Estimating the early limit (Ma).
2. Estimating the late bound (Ma).
3. Estimating the critical moment (Ma) and the early bound (Ma).
4. Estimating the critical range (Ma) and uncertainty (Ma).

4.2.1 Estimating the Early Limit

The early limit of the critical moment (c_{EL}) is defined as the earliest moment with probability greater than zero for the generation-migration-accumulation of hydrocarbons estimated using only the first participating block of each essential element or process while treating all the essential

elements and processes as independent events. The early limit is the first moment in time with the possibility of the critical moment occurring, before this point, it is not possible for the critical moment to exist (i.e. the probability is zero). Note that the late limit for the occurrence of the critical moment is present day.

For each moment in time i the probability of c_{EL} is defined as:

$$P(c_{EL})^i = \prod_{E=1}^{n} W_E P(E)_1^i \tag{4.1}$$

where P is the probability, n is the total number of elements and processes, E is the element or process being considered, the second subscript (1) is the participating block position within the element or process row (in this case only the first participating block), the superscript represents the moment i in time, W_E is a weight with values between 0 and 1 representing the confidence in the data source for the timing of element or process E. $\prod$ is the product symbol.

If it is assumed that W_E is 1 for all elements and processes, then equation 4.1 can be written out explicitly as:

$$P(c_{EL})^i = P(SR)_1^i \cdot P(RR)_1^i \cdot P(SL)_1^i \cdot P(OV)_1^i \cdot P(TF)_1^i \cdot P(GMA)_1^i \cdot P(PT)_1^i \tag{4.2}$$

where SR is the source rock, RR is the reservoir rock, SL is the seal rock, OV is the overburden rock and TF is trap formation, GMA is generation-migration-accumulation and PT is preservation time (GMA and PT should be used only used if available from another data source). These abbreviations will be used throughout the rest of this paper. I choose the early limit c_{EL} as the location of the earliest occurring non-zero probability value. See figure 4.2(a-f) for an example of the application of equation (4.2).

4.2.2 Estimating the Late Bound

The late bound of the critical moment (c_{LB}) is defined as the earliest moment with the greatest probability value for the generation-migration-accumulation of hydrocarbons estimated using all participating blocks of each element or process while treating all the essential elements and pro-

cesses as independent events. For each moment in time i within the age of the petroleum system the probability of c_{LB} is:

$$P(c_{LB})^i = \prod_{E=1}^{n} W_E \left(\sum_{j=1}^{m_E} P(E)_j \right)^i \tag{4.3}$$

where P is the probability, E is the element or process being considered, m_E is the number of participating blocks in the row of E, the second subscript j ranges from 1 to m_E, n is the total number of elements and processes, W_E (with values between 0 and 1) is a weight representing the confidence in the data source for the timing of element or process E . The oldest moment with the greatest probability calculated this way is then selected as c_{LB}. See figure 4.2(g-l) for an example of the application of equation (4.3).

4.2.3 Estimating the Critical Moment and the Early Bound

The best estimate of the critical moment is obtained by making use of some additional insight into the actual processes of generation-migration-accumulation. Generation and migration of the hydrocarbons are dependent on the presence of a source rock and a sufficient overburden rock. The source rock contains organic matter and the overburden rock pushes the source rock into the oil/gas window where it is subjected to the appropriate temperature for generation and migration to take place. The effectiveness of the overburden rock in pushing the source rock into the oil/gas window is directly related to the proportion of overburden rock above the source rock. This can be estimated as the thickness of overburden rock above a particular source rock (T_j) divided by the total thickness of overburden rock (T_t) in the petroleum system. The probability of generation and migration ($P(GM)^i$) at a moment in time i is then given as:

$$P(GM)^i = \left(W_{SR} \sum_{j=1}^{m_{SR}} \frac{T_j}{T_t} P(SR)_j . W_{OV} \sum_{j=1}^{m_{OV}} P(OV)_j \right)^i \tag{4.4}$$

Accumulation is dependent on the reservoir rock, the seal rock and trap formation. It begins to take place only after the beginning of generation and when the reservoir rock is present together with a seal rock and a trap to keep the hydrocarbons in place. I calculate the probability of accumulation $P(A)^i$ at any moment in time i, given that the reservoir rock and seal rock exists and that

the traps have been formed after the process of generation has begun.

$$P(A)^i = \left(W_{RR} \sum_{j=1}^{m_{RR}} P(RR) \cdot W_{SL} \sum_{j=1}^{m_{SL}} P(SL) \cdot W_{TF} \sum_{j=1}^{m_{TF}} P(TF) \right)^i \tag{4.5}$$

The probability of critical moment occurring at time i is then found by combining both probabilities $P(GM)^i$ and $P(A)^i$ as independent events:

$$P(c_M)^i = P(GM)^i \cdot P(A)^i \tag{4.6}$$

The critical moment is then selected as the earliest position i with the greatest probability value. To estimate the early bound c_{EB} I again make use of equation (4.3). I select as the early bound the location of the greatest probability next to but older than the position of the best estimate c_M. See figure (4.3) for an example of the application of equation (4.6).

4.2.4 The Critical Range and Uncertainty

The critical range (c_R) is defined as the absolute value of the difference between the early bound and the late bound.

$$c_R = |c_{EB} - c_{LB}| \tag{4.7}$$

The critical moment falls within the critical range such that: $(c_{LB} <= c_M <= c_{EB})$; where c_M is the critical moment. The critical range can thus be used to quantify uncertainty associated with estimation of the critical moment. The uncertainty associated with the estimation u_{CM} is defined as follows:

$$u_{CM} = \frac{1}{2} c_R = \frac{1}{2} |c_{EB} - c_{LB}| \tag{4.8}$$

The critical moment is then reported as $c_M \pm |u_{CM}|$.

4.3 Application

4.3.1 The Ellesmerian(!)

I will demonstrate the application of the quantitative probabilistic framework using the Ellesmerian(!). The Ellesmerian(!) is located in the North slope of Alaska. Trap formation preceded generation-migration-accumulation by several million years resulting in major oil accumulations and timing favorable for stratigraphic traps (Bird, 1994). However there is significant risk associated with migrating petroleum from the source rock upward and structural traps (Peters et. al., 2009). Table 4.1 shows the data used as input into the quantitative probability framework for the Ellesmerian(!). I choose the weight W_E for all elements and processes as 1 in all examples. I assume the burial history is unknown and omit input of any direct information about generation-migration-accumulation and preservation from other source rocks. Figure 4.2 shows the estimation of the early limit, the early bound and the late bound for the Ellesmerian(!). It depicts the probability as a function of time for all elements and processes. Figures 4.2(a and g) shows probability as a function of time calculated using the source rock. Before deposition of the source rock, the probability is zero; it then increases once the source rock is deposited. Figures 4.2(f) show the product of all probabilities calculated using only the first block of each element or process in the events chart. Figures 4.2(l) show the product of all probabilities calculated using all block of each element or process in the events chart. The early limit is 166 Ma (black square), the early bound is 64 Ma (blue triangle) and the late bound is 44 Ma (red dot). Figure 4.3 shows the estimate of c_M (green star) for the Ellesmerian(!). Combining the analysis in figures 2 and 3, I obtain values of 61 $\pm$ 10 Ma for the critical moment and uncertainty, which is consistent with (Peters et. al., 2009). Figure 4.4 shows the events chart for the Ellesmerian(!) with the critical range and critical moment included.

Element or Process	Start Time (Ma)	End Time (Ma)
Source Rock	234.2	212.8
Reservoir Rock	349.7	335.2
Reservoir Rock	326.0	305.4
Reservoir Rock	244.9	234.3
Reservoir Rock	230.4	225.1
Reservoir Rock	214.4	207.5
Reservoir Rock	202.2	196.0
Reservoir Rock	147.1	131.0
Reservoir Rock	111.2	105.0
Reservoir Rock	79.0	61.0
Reservoir Rock	61.0	46.1
Seal Rock	336.0	326.1
Seal Rock	306.2	294.0
Seal Rock	234.3	231.3
Seal Rock	225.9	217.5
Seal Rock	209.9	201.5
Seal Rock	196.9	190.8
Seal Rock	131.8	123.5
Seal Rock	106.6	97.5
Seal Rock	64.6	59.2
Seal Rock	49.3	40.1
Overburden Rock	208.4	8.8
Trap Formation	166.4	129.7
Trap Formation	44.8	31.0

Table 4.1: Input into the quantitative probability framework for the Ellesmerian(!)

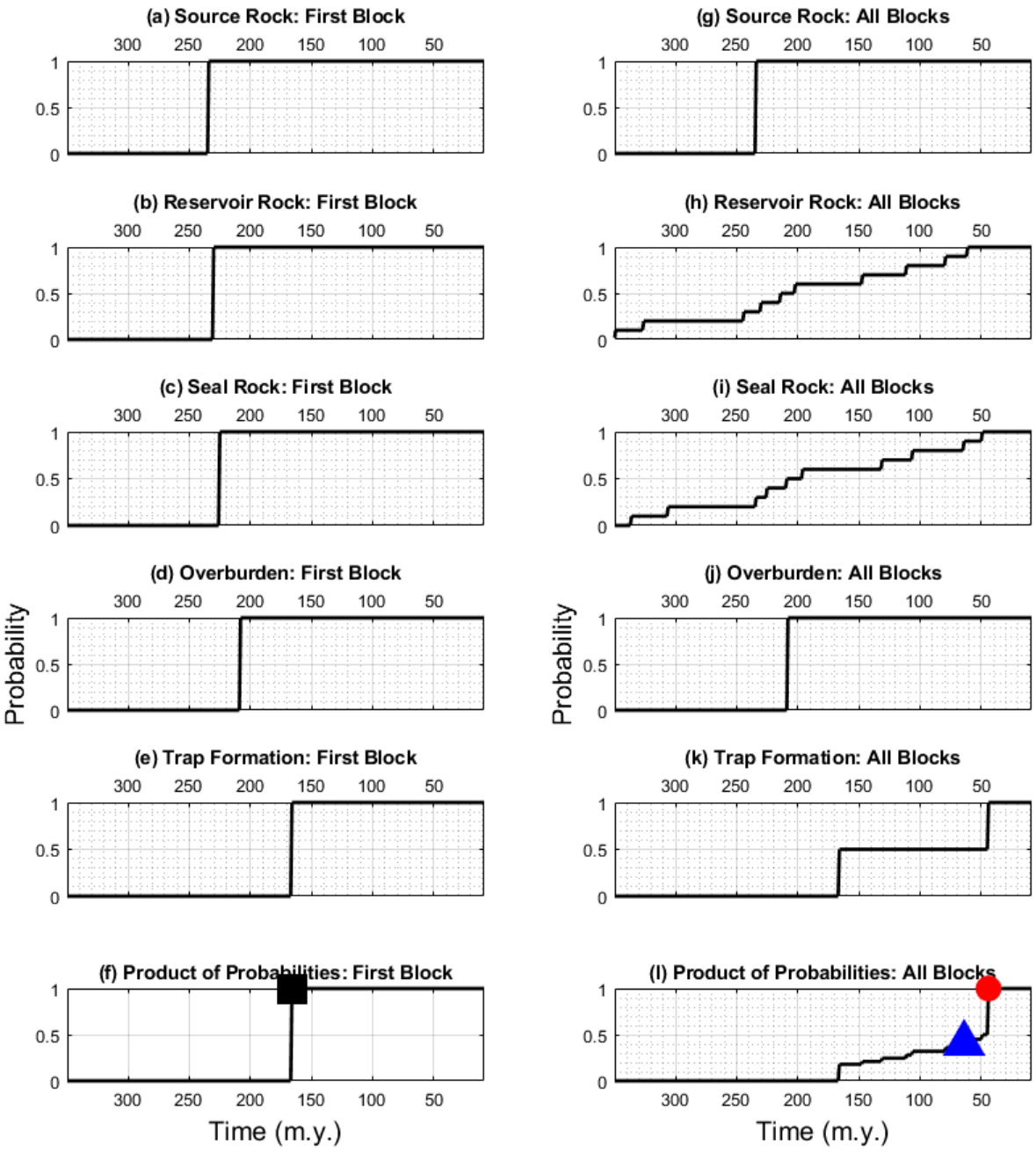

Figure 4.2: Estimating early limit (black square), early bound (blue triangle) and late bound (red dot) of the critical moment for the Ellesmerian(!).

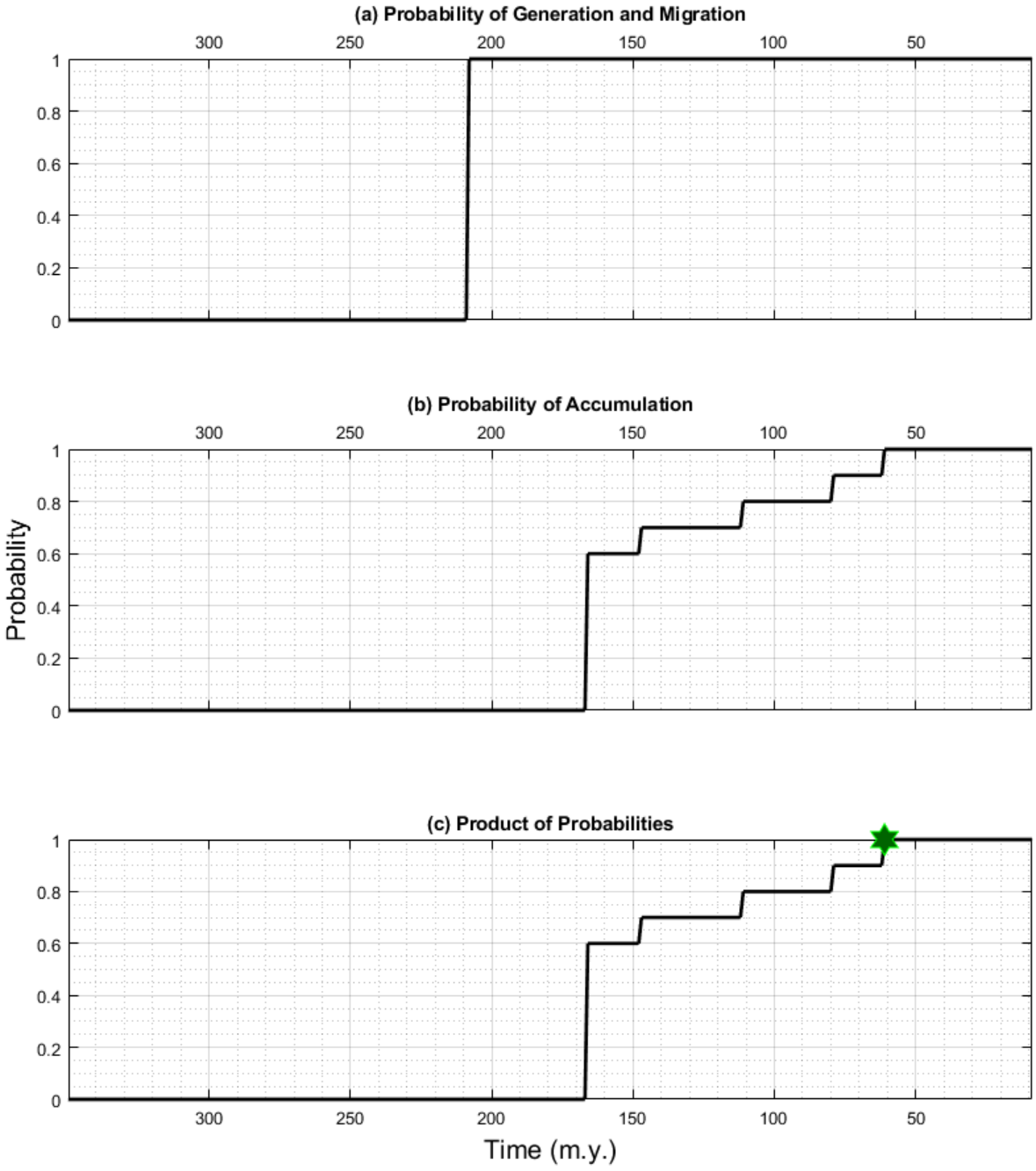

Figure 4.3: Estimating the critical moment (green star) for the Ellesmerian(!).

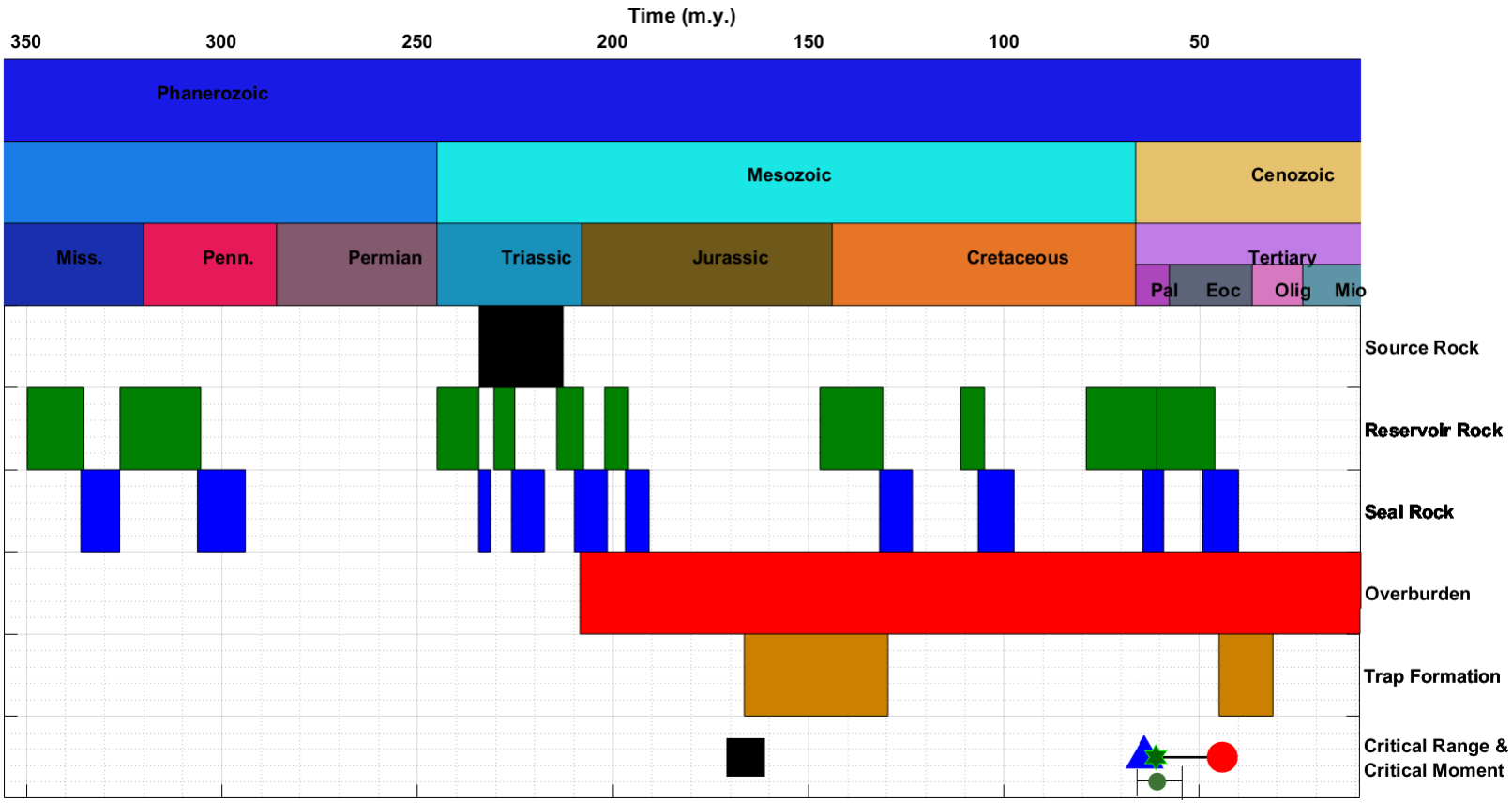

Figure 4.4: Events chart for the Ellesmerian(!). The blue triangle and the red dot are the early and late bounds, the black square is the early limit. The green star is the critical moment with a value of 61 ± 10 which agrees with Peters et. al., (2009)

4.3.2 Simple Petroleum Systems

A special case for the critical range occurs in simple petroleum systems with very little or no duplicity in the elements of the system. The critical range (both early and late bounds) converges at a point, which is also the critical moment. To examine this I apply the quantitative probability framework to the fictitious Deer-Boar(.) (figure 4.1) introduced by Magoon and Dow, (1994). Table 4.2 shows the data used as input into the quantitative probability framework for the Deer-Boar(.). Figures 4.5 to 4.6 show the estimation of the early limit, the late bound, the critical moment and the early bound for the Deer-Boar(.). All four numbers converge at 241 Ma. To estimate the uncertainty for special cases as this, I choose the position with the next highest probability predicted by the individual elements or processes. In this case, I select the position of GMA in figure 4.5 (inverted blue triangle) which is 258 Ma . I then subtract the position of c_M from this and half the result to obtain an uncertainty of 8.5 Ma. The critical moment is then reported as 241 ± 8.5 Ma, which is consistent with Magoon and Dow (1994). Figure 4.7 shows the events chart for the Deer-Boar(.).

Element or Process	**Start Time (Ma)**	**End Time (Ma)**
Source Rock	338.01	378.1
Reservoir Rock	378.1	314.02
Seal Rock	314.02	301.3
Overburden Rock	378.1	247.1
Trap Formation	288.5	267.7
GMA	258.6	240.6
Preservation Time	240.6	0

Table 4.2: Input into the quantitative probability framework for the Deer-Boar(.)

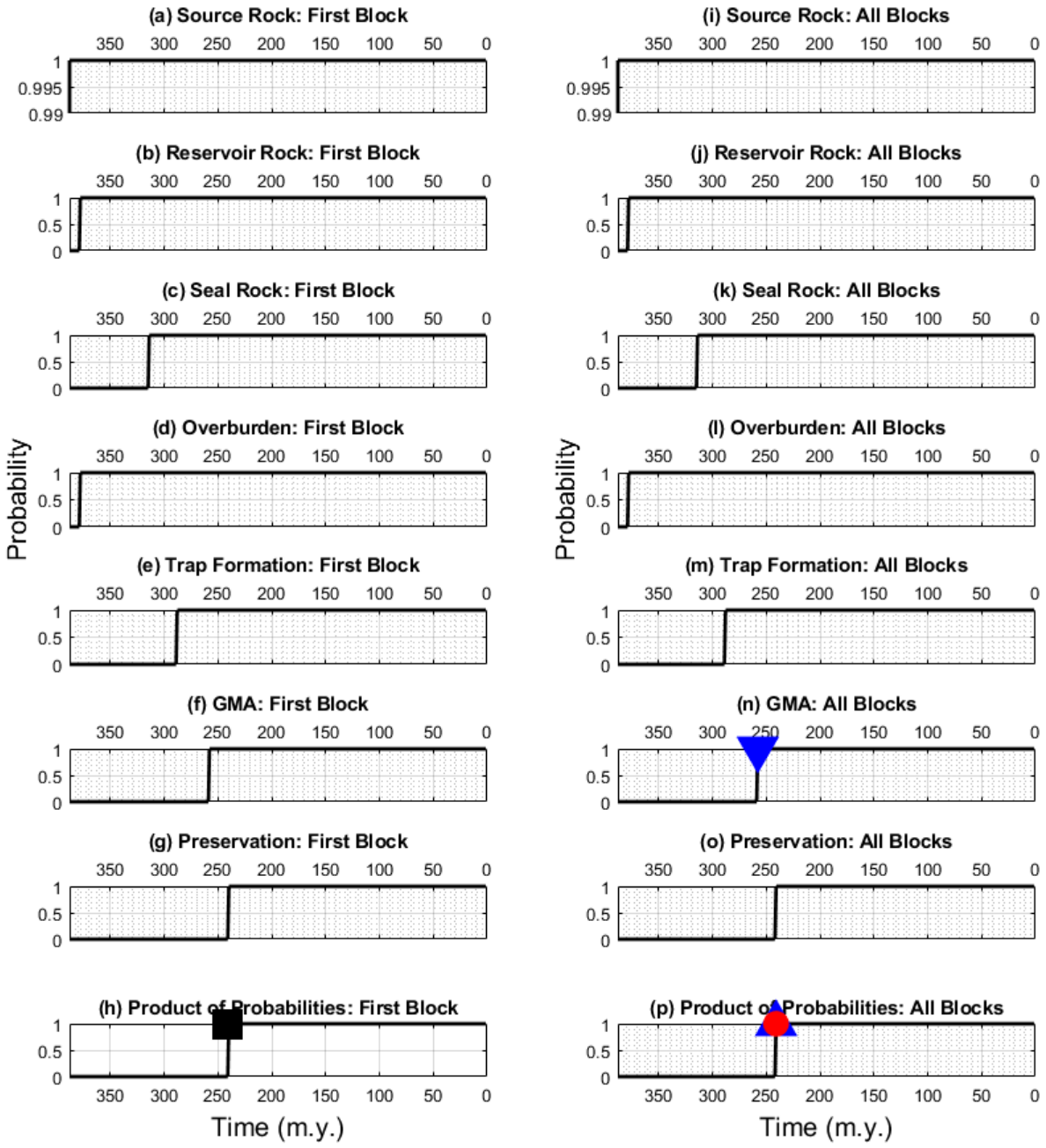

Figure 4.5: Estimating early limit (black square), early bound (blue triangle) and late bound (red dot) of the critical moment for the Deer-Boar(.). In this case the points all have the same value. The inverted blue triangle is selected for uncertainty analysis.

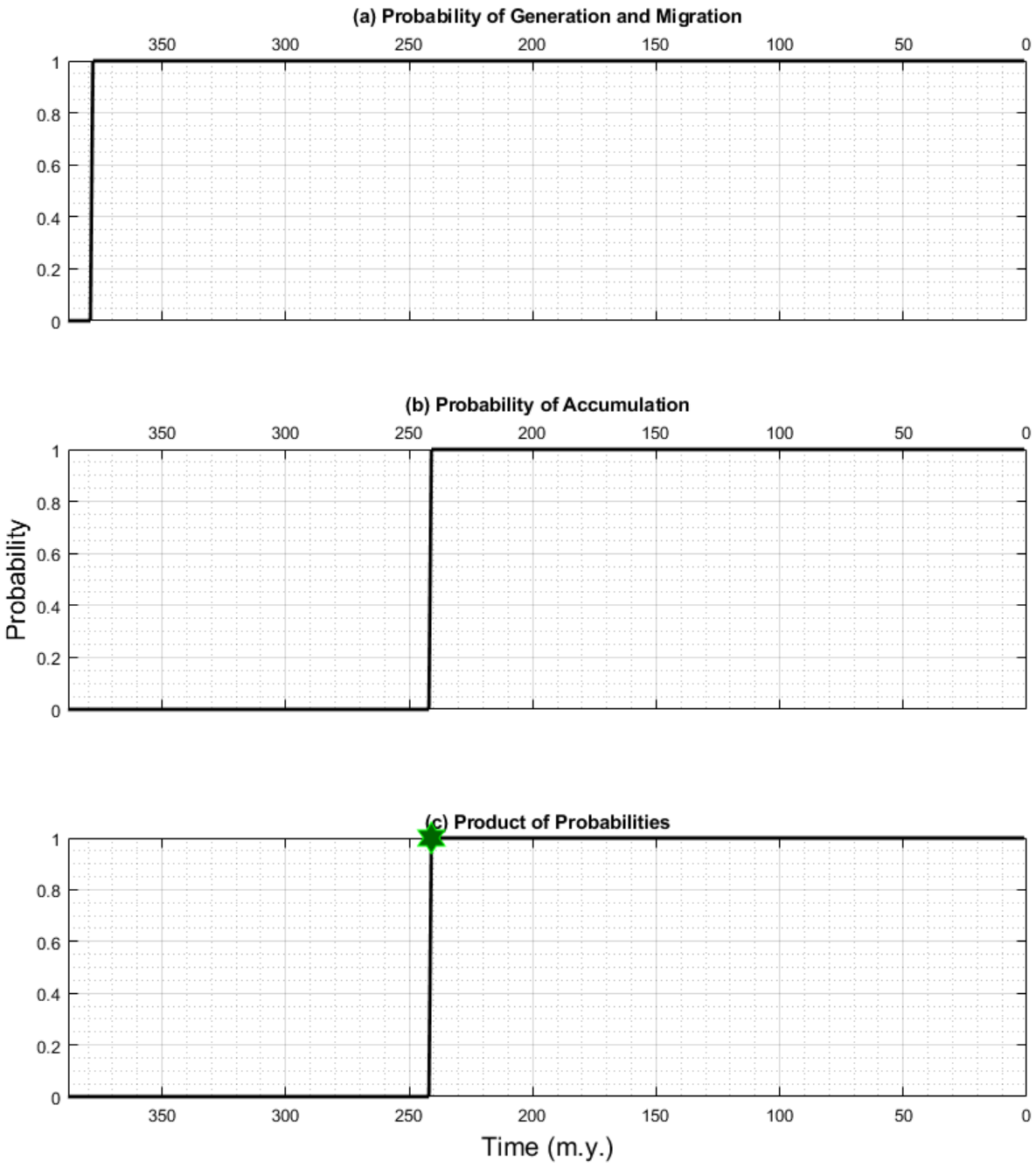

Figure 4.6: Estimating the critical moment (green star) for the for the Deer-Boar(.)

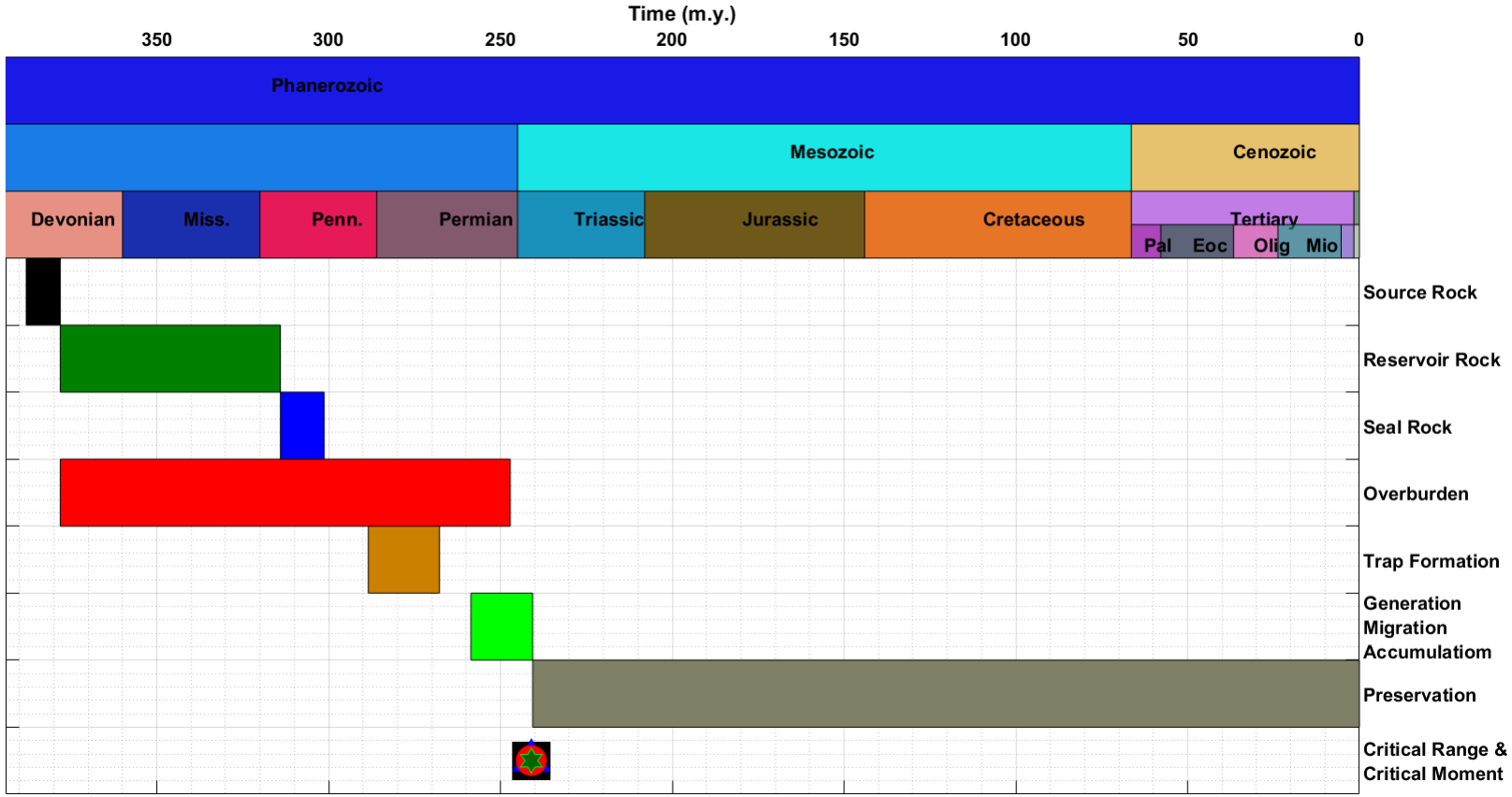

Figure 4.7: Events chart for the Deer-Boar(.). The simplicity of the Deer-Boar(.) generates an early limit (black square) and late bound (red dot) of the same value which is also the critical moment (green star; 241 Ma)

4.3.3 The Total Petroleum System

The concept of the petroleum system described above only includes discovered hydrocarbon, it was, therefore, necessary to develop to include undiscovered oil and gas fields. Magoon (1995) termed undiscovered resources complementary plays and complementary prospects. The total petroleum system (TPS) refers to the petroleum system of Magoon and Dow (1994), and the sum of all undiscovered oil and gas fields in the complementary plays and complementary prospects within that system (Magoon, 1995; Magoon and Beaumont, 1999).

Magoon and Schmoker (2000) define the TPS as the essential elements (source rock, reservoir rock, seal rock, and overburden rock) and processes (generation-migration-accumulation and trap formation) as well as all genetically related petroleum that occurs in seeps, shows, and accumulations, both discovered and undiscovered, whose provenance is a pod or closely related pods of active source rock. The assessment unit (AU) is a volume of rock within the TPS that encompasses fields, discovered and undiscovered, sufficiently homogeneous in terms of geology, exploration strategy and risk characteristics to constitute a single population of field characteristics with respect to criteria used for resource assessment (Magoon and Schmoker, 2000). Two commonly used accumulation types are conventional and continuous accumulations. Conventional oil and gas accumulations generally occur in stratigraphic and structural traps within fields while continuous oil and gas accumulations include those types of accumulations where the source rock and reservoir rock are interbedded or the same (Dubiel, 2013).

In this section I apply the quantitative probability framework to total petroleum systems from the San Juan Basin Province. The data and information used as input to the quantitative probability framework in this section is obtained from the U.S. Geological Survey Digital Data Series 69–F (Dubiel, 2013). I follow the TPS nomenclature used in this report. The San Juan Basin (Figure 4.8) is a Laramide structural depression that may have formed about 75 million years ago. It is located on the eastern margin of the Colorado Plateau in New Mexico and Colorado. The basin has a pronounced northwest-southeast structural grain that appears to have controlled sedimentary geometry and shoreline positions throughout the Phanerozoic (Dubiel, 2013). The basin margin is

characterized by Mesozoic sedimentary outcrops. Early and late Cenozoic tectonic activity resulted in folding, fracturing, and uplift. Two total petroleum systems found in the San Juan Basin are the Lewis Shale TPS and the Fruitland TPS. The Fruitland TPS contains the Tertiary Conventional Gas AU while the Lewis Shale TPS contains the Lewis Continuous Gas Resource. Table 4.3 gives a summary of their major elements. I apply the quantitative probability framework the two TPSs. Figures 4.9, 4.10, and 4.11 show the results for Tertiary Conventional Gas AU while Figures 4.12, 4.13, and 4.14 show the results for the Lewis Continuous Gas Resource. The critical moments for the Tertiary Conventional Gas AU and Lewis Continuous Gas Resource are estimated as 25 Ma and 56 Ma respectively. The ability to predict the critical moment in total petroleum systems will reduce the risk associated with the exploration assessment of undiscovered resources.

TPS & AU	**Source**	**Reservoir**	**Trap/Seal**
Fruitland TPS			
Tertiary Conventional Gas AU	Coal of the Fruitland Formation	Paleocene Ojo Alamo Sandstone, Nacimiento Formation, and San Jose Formation.	Overbank mudstones, stratigraphic pinchouts and an anticline.
Lewis Shale TPS			
Lewis Continuous Gas Resource	Lewis Shale	La Ventana and Chacra Tongues of the Cliff House Sandstone	Lewis Shale

Table 4.3: Summary of the major elements of Fruitland and Lewis Total Petroleum Systems, San Juan Basin (from the U.S. Geological Survey Digital Data Series 69–F; Dubiel, 2013))

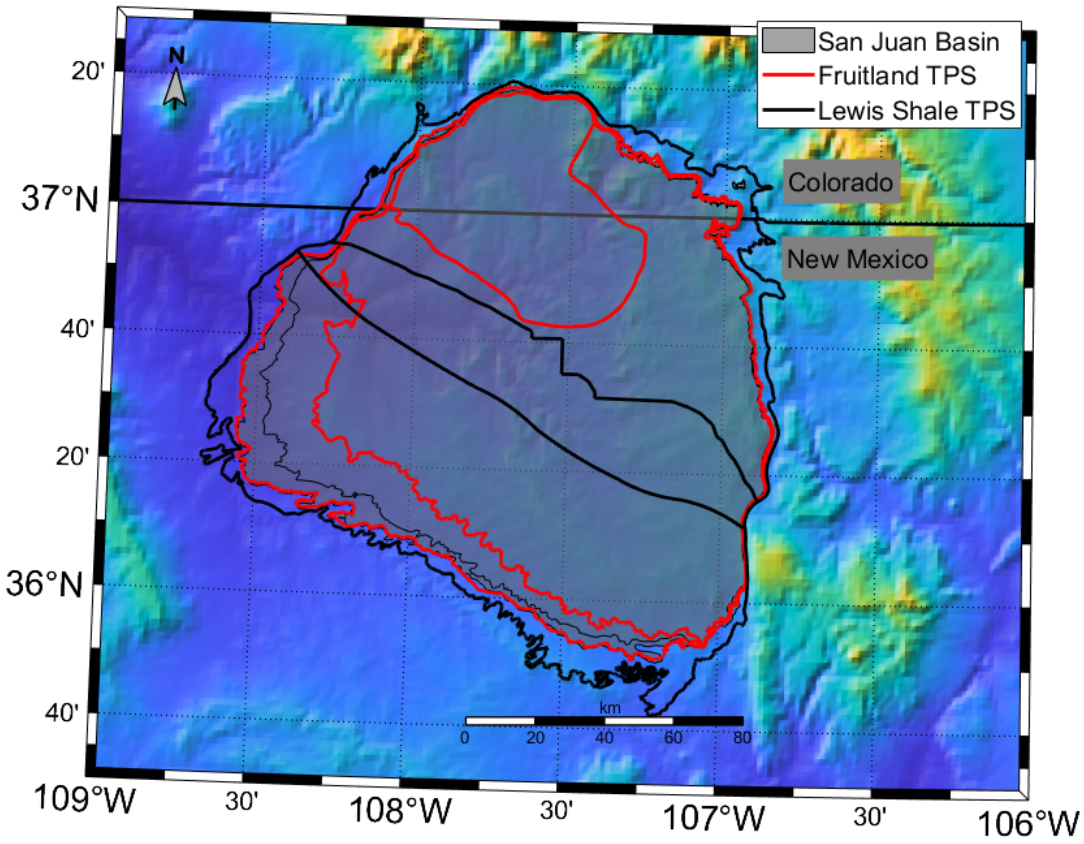

Figure 4.8: Map showing the location and boundary of the San Juan Basin, the Fruitland TPS, and the Lewis Shale TPS.

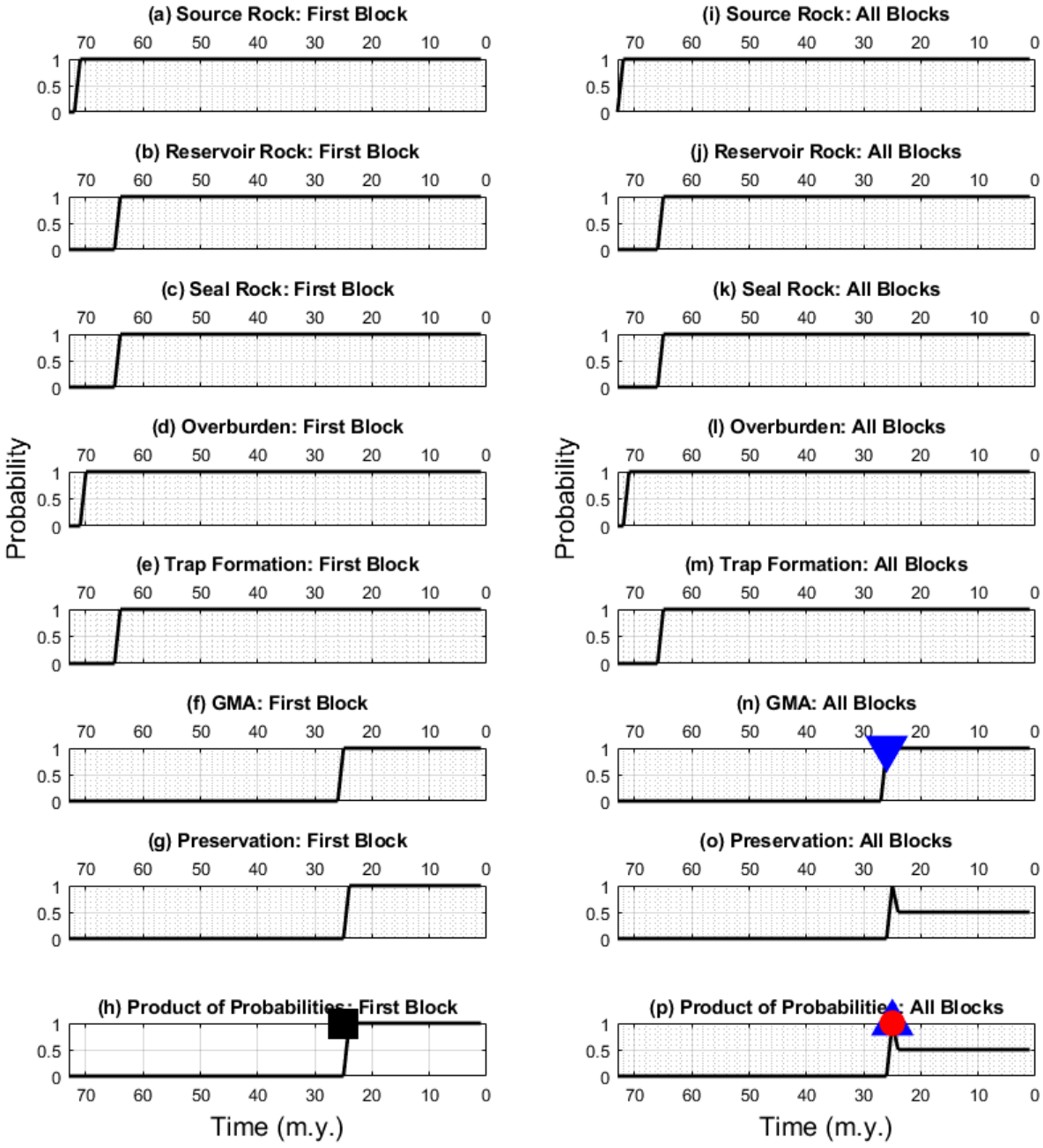

Figure 4.9: Estimating early limit (black square), early bound (blue triangle) and late bound (red dot) of the critical moment for the Tertiary Conventional Gas AU.

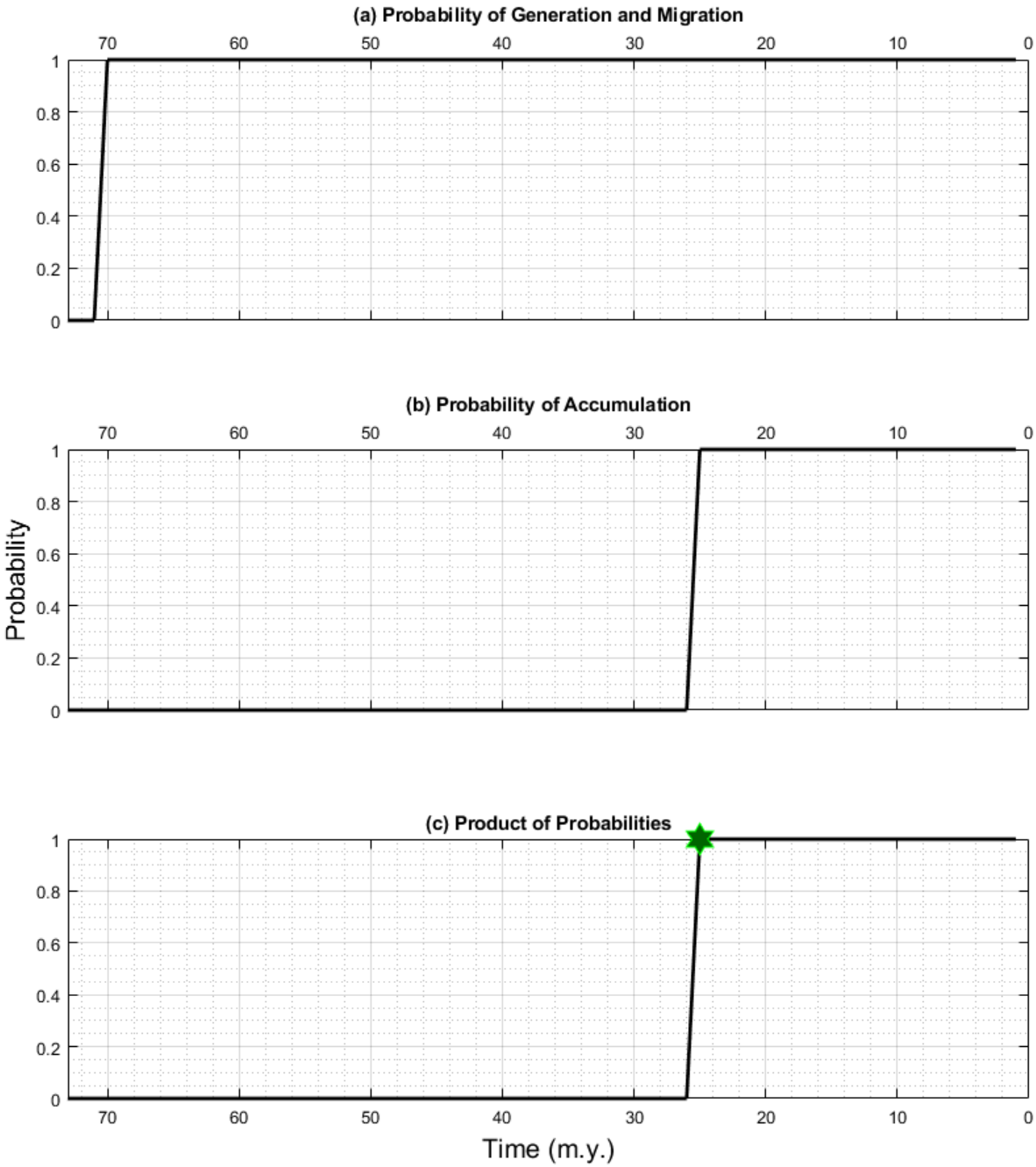

Figure 4.10: Estimating the critical moment (green star) for the Tertiary Conventional Gas AU.

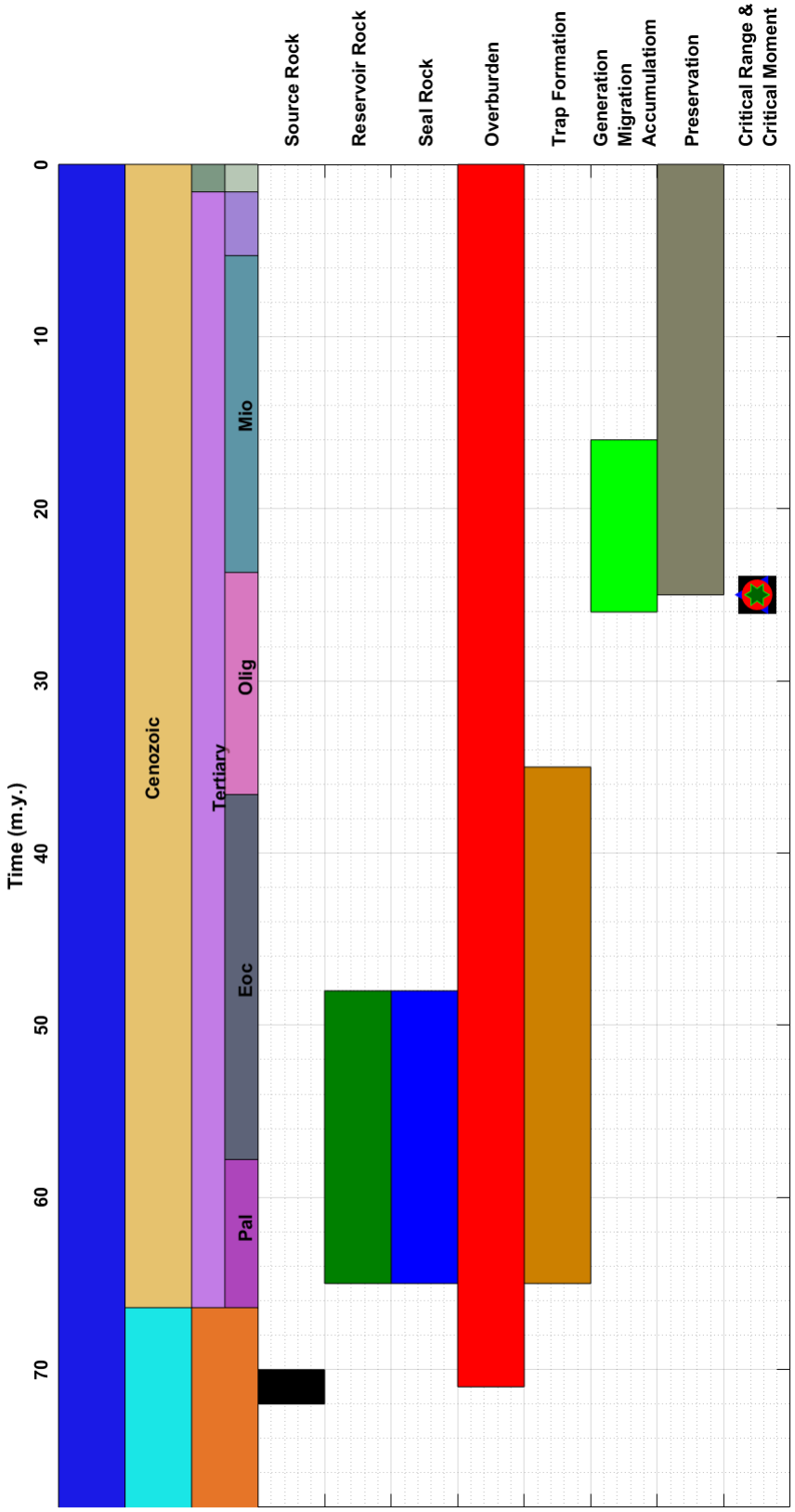

Figure 4.11: Events chart for the Tertiary Conventional Gas AU.

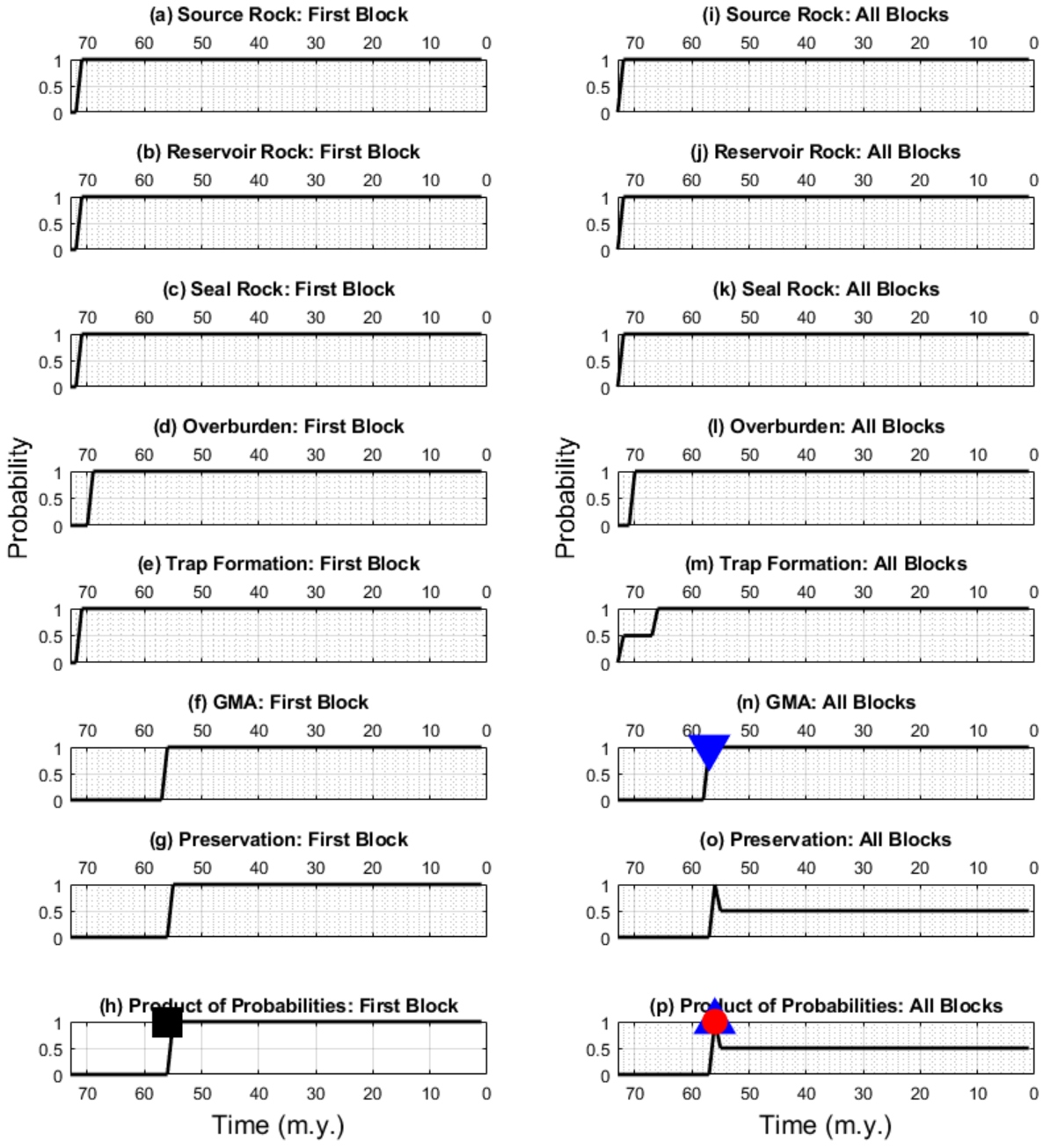

Figure 4.12: Estimating early limit (black square), early bound (blue triangle) and late bound (red dot) of the critical moment for the Lewis TPS.

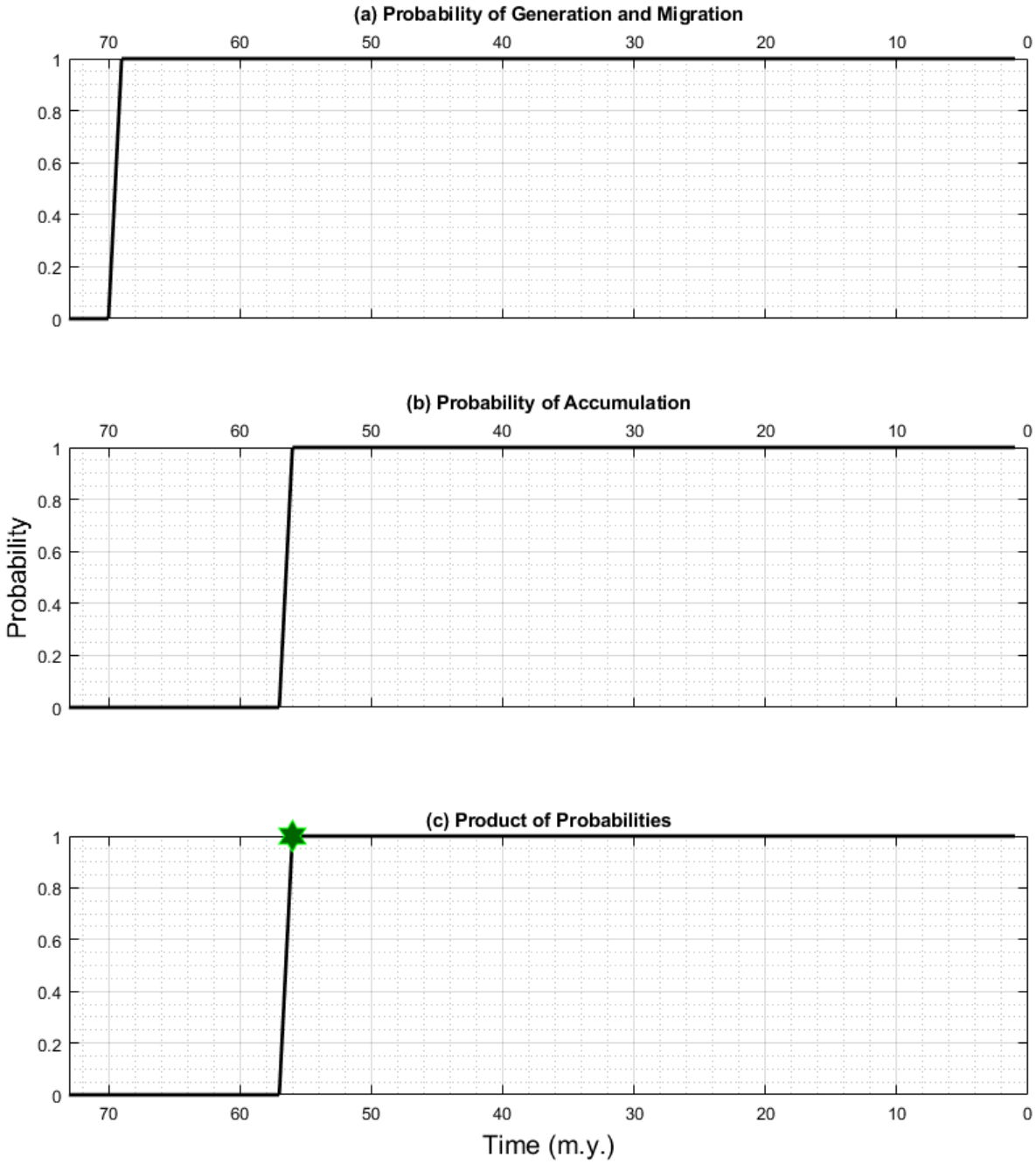

Figure 4.13: Estimating the critical moment (green star) for the Lewis TPS.

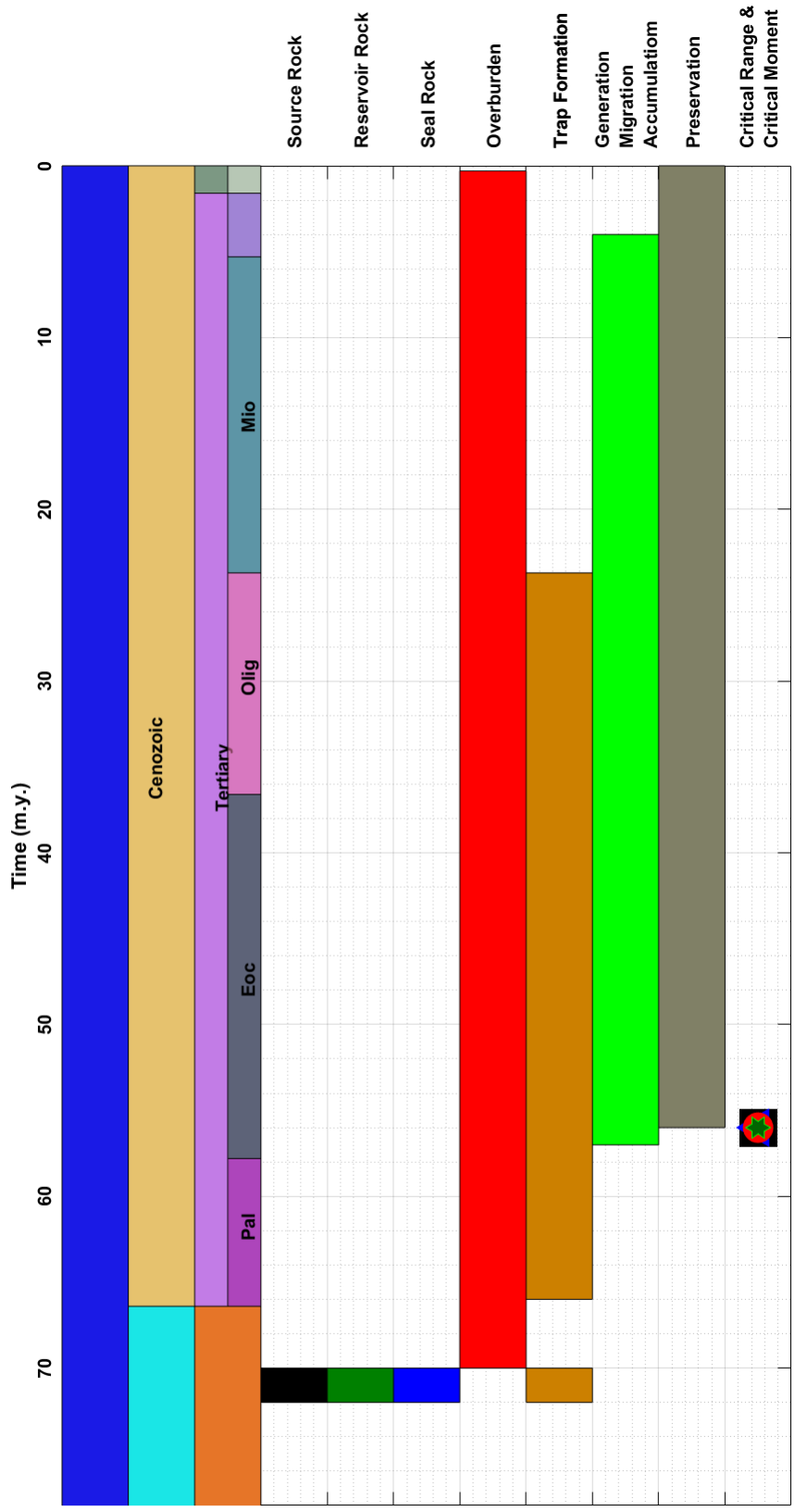

Figure 4.14: Events chart for the Lewis TPS.

4.4 Conclusion to Chapter 4

The critical moment of a petroleum system is best estimated using the burial history data and thermal history data such as vitrinite reflectance measurements. In the study of many petroleum systems these data are unavailable, unreliable or incomplete. This introduces uncertainty into the determination of the critical moment. The critical moment is important because the stratigraphic and geographic extents of a petroleum system are defined at the critical moment. The uncertainty of the critical moment can therefore translate to risk in exploration assessment, hence it is important to quantify the amount of uncertainty involved in the estimation of the critical moment. I develop a quantitative probability framework for estimating the critical moment and associated uncertainty. I calculate the best probabilistic estimate of the critical moment and define an early limit, an early bound and a late bound for the critical moment. I define the critical range as the absolute value of the difference between the early bound and the late bound and estimate the uncertainty associated with the critical moment as half the critical range. The quantitative probability framework introduces consistency in estimating the critical moment and the quantification of uncertainty helps reduce the risk associated with exploration assessment.

REFERENCES

1. Akaike, H., 1969, Fitting autoregressive models for prediction: Annals of the institute of Statistical Mathematics, 21, no. 1, 243-247.

2. Akaike, H., 1974, A new look at the statistical model identification: IEEE Transactions on Automatic Control, 19, no. 6, 716-723.

3. Alferov, Z., H. Kroemer, and J. Kilby. 2000, Nobel Prize in Physics 2000.

4. Amosu, A., and Y. Sun. 2017a, Fischerlab: An interactive program for generating dynamic Fischer plots from wireline logs and stratigraphic data. Paper read at AAPG Annual Convention and Exhibition.

5. Amosu, A., and Y. Sun, 2017b, WheelerLab: An interactive program for sequence stratigraphic analysis of seismic sections, outcrops and well sections and the generation of chronostratigraphic sections and dynamic chronostratigraphic sections: SoftwareX, 6, 19-24.

6. Amosu, A., and Y. Sun, 2019, A quantitative probabilistic framework for estimating the critical moment in a petroleum system: AAPG Bulletin, 103, no. 1, 177-187.

7. Bernoulli, D., 1738, Hydrodynamica: sive de viribus et motibus fluidorum commentarii.

8. Beylkin, G., 1987, Discrete radon transform: IEEE transactions on acoustics, speech, and signal processing, 35, no. 2, 162-172.

9. Bird, K. J., 1994, Ellesmerian (!) Petroleum System, North Slope of Alaska, USA: Chapter 21: Part V. Case Studies–Western Hemisphere.

10. Bradshaw, A., and M. Ng, 1987, Multiple attenuation by parabolic stack Radon transform: Geo-X Systems internal paper.

11. Broussard, M. 1975, Modern river deltas: Variability of processes and sand bodies. Houston Geological Society.

12. Brown, A. R., 2011, Interpretation of three-dimensional seismic data: Society of Exploration Geophysicists and American Association of Petroleum ....

13. Brown, R., 1827, Brownian motion: Unpublished experiment.

14. Buffon, G. 1777, Histoire naturelle, generale er particuliere, Supplément 4. Essai d'arithmetique morale. McGraw-Hill Book Company, Inc.

15. Bunsen, R. W., and H. E. Roscoe, 1863, III. Photochemical researches.—Part V. On the measurement of the chemical action of direct and diffuse sunlight: Proceedings of the Royal Society of London, no. 12, 306-312.

16. Burg, J. P., 1967, Maximum entropy spectral analysis, paper presented at the 37th Annual International Meeting, Soc. of Explor: Geophys., Oklahoma City, Okla.

17. Cary, P. 1999, The simplest discrete Radon transform: 68th Ann. Paper read at Internat. Mtg., Soc. Expl. Geophys., Expanded Abstracts.

18. Castagna, J. P., and S. Sun, 2006, Comparison of spectral decomposition methods: First break, 24, no. 3.

19. Castagna, J. P., S. Sun, and R. W. Siegfried, 2003, Instantaneous spectral analysis: Detection of low-frequency shadows associated with hydrocarbons: The leading edge, 22, no. 2, 120-127.

20. Cayley, A., 1846, Sur quelques propriétés des déterminants gauches: Journal für die reine und angewandte Mathematik, 1846, no. 32, 119-123.

21. Chabyshova, E., and G. Goloshubin, 2014, Seismic modeling of low-frequency "shadows" beneath gas reservoirs: Geophysics, 79, no. 6, D417-D423.

22. Chapman, C., 1981, Generalized Radon transforms and slant stacks: Geophysical Journal International, 66, no. 2, 445-453.

23. Chen, X., W. Zhong, Z. He, and W. Zou, 2016, Frequency-dependent attenuation of compressional wave and seismic effects in porous reservoirs saturated with multi-phase fluids: Journal of Petroleum Science and Engineering, 147, 371-380.

24. Cichostępski, K., A. Kwietniak, and J. Dec, 2019, Verification of bright spots in the presence of thin beds by AVO and spectral analysis in Miocene sediments of

25. Carpathian Foredeep: Acta Geophysica, 67, no. 6, 1731-1745.

26. Cooley, J. W., and J. W. Tukey, 1965, An algorithm for the machine calculation of complex Fourier series: Mathematics of computation, 19, no. 90, 297-301.

27. d'Alembert, J. l. R., 1747, Recherches sur la courbe que forme une corde tendue mise en vibration.

28. Dampier, W., 1961, A history of science and its relations with philosophy and religion: CUP Archive.

29. Daubechies, I., 1992, Ten lectures on wavelets: SIAM.

30. Deans, S. R., 1983, The Radon Transform and Some of Its Applications. JohnWiley & Sons: Inc. New York, USA.

31. Deng, J.-X., D.-H. Han, J. Liu, and Q. Yao, 2007, Application of spectral decomposition to detect deepwater gas reservoir, SEG Technical Program Expanded Abstracts 2007: Society of Exploration Geophysicists, 1427-1431.

32. Dilay, A., and J. Eastwood, 1995, Spectral analysis applied to seismic monitoring of thermal recovery: The leading edge, 14, no. 11, 1117-1122.

33. Dubiel, R. 2013, Geology, sequence stratigraphy, and oil and gas assessment of the Lewis Shale Total Petroleum System, San Juan Basin, New Mexico and Colorado: Chapter 5 in Total petroleum systems and geologic assessment of undiscovered oil and gas resources in the San Juan Basin Province, exclusive of Paleozoic rocks, New Mexico and Colorado. US Geological Survey

34. Duin, E., J. Doornenbal, R. Rijkers, J. Verbeek, and T. E. Wong, 2006, Subsurface structure of the Netherlands-results of recent onshore and offshore mapping: Netherlands Journal of Geosciences, 85, no. 4, 245.

35. Durrani, T., and D. Bisset, 1984, The Radon transform and its properties: Geophysics, 49, no. 8, 1180-1187.

36. Ebrom, D., 2004, The low-frequency gas shadow on seismic sections: The leading edge, 23, no. 8, 772-772.

37. Einstein, A., 1906, Zur theorie der brownschen bewegung: Annalen der physik, 324, no. 2, 371-381.

38. Euler, L., 1755, Institutiones calculi differentialis.

39. Euler, L., 1766, Eclaircissemens sur le mouvement des cordes vibrantes: Melanges de philosophie et de la mathematique de la societe royale de Turin, 1-26.

40. Foster, D. J., and C. C. Mosher, 1992, Suppression of multiple reflections using the Radon transform: Geophysics, 57, no. 3, 386-395.

41. Fourier, J., 1822, Theory analytique de la chaleur: Chez Firmin Didot, Paris.

42. Gridley, J., and G. Partyka, 1997, Processing and interpretational aspects of spectral decomposition, SEG Technical Program Expanded Abstracts 1997: Society of Exploration Geophysicists, 1055-1058.

43. Hampson, D., 1986, Inverse velocity stacking for multiple elimination, SEG Technical Program Expanded Abstracts 1986: Society of Exploration Geophysicists, 422-424.

44. Hart, Y., and L. Mahadevan, 2019, Geometric probability, psychophysics and invariance: bioRxiv, 531889.

45. Hartmann, D. J., E. A. Beaumont, and N. Foster, 1999, Predicting reservoir system quality and performance: Exploring for oil and gas traps: AAPG Treatise of Petroleum Geology, Handbook of Petroleum Geology, 9-1.

46. Heisenberg, W., 1930, Die selbstenergie des elektrons: Zeitschrift für Physik, 65, no. 1, 4-13.

47. Hill, D., C. Combee, and J. Bacon, 2006, Over/under acquisition and data processing: The next quantum leap in seismic technology?: First Break, 24, no. 6.

48. Hlawatsch, F., and G. F. Boudreaux-Bartels, 1992, Linear and quadratic time-frequency signal representations: IEEE signal processing magazine, 9, no. 2, 21-67.

49. Hugonnet, P., and G. Canadas, 1995, Aliasing in the parabolic Radon transform, SEG Technical Program Expanded Abstracts 1995: Society of Exploration Geophysicists, 1366-1369.

50. Itakura, F. 1968, Analysis synthesis telephony based on the maximum likelihood method. Paper read at The 6th international congress on acoustics, 1968.

51. Kelamis, P. G., E. F. Chiburis, and S. Shahryar, 1990, Radon multiple elimination, a practical methodology for land data, SEG Technical Program Expanded Abstracts 1990: Society of Exploration Geophysicists, 1611-1613.

52. Kilby, J. S. 1964, Miniaturized electronic circuits. Google Patents.

53. Klein, G. D., 2012, Sandstone depositional models for exploration for fossil fuels: Springer Science & Business Media.

54. Korneev, V. A., G. M. Goloshubin, T. M. Daley, and D. B. Silin, 2004, Seismic low-frequency effects in monitoring fluid-saturated reservoirs: Geophysics, 69, no. 2, 522-532.

55. Kostov, C., 1990, Toeplitz structure in slant-stack inversion, SEG Technical Program Expanded Abstracts 1990: Society of Exploration Geophysicists, 1618-1621. Lagrange, J.-L., 1759, Recherches sur la nature et la propagation du son: Miscellanea Taurinensia, 1, 39-148.

56. Levinson, N., 1947, The Wiener rms (root mean square) error criterion in filter design and prediction: J. of Math, and Phys., v. 25.

57. Li, Y., J. Li, and X. Zheng, 2010, Channel system characterization using wigner-ville distribution-based spectral decomposition, SEG Technical Program Expanded Abstracts 2010: Society of Exploration Geophysicists, 1418-1422.

58. Liouville, J., 1838, Premier Mémoire sur la Théorie des Équations différentielles linéaires et sur le développement des Fonctions en séries: Journal de Mathématiques Pures et Appliquées, 561-614.

59. Liu, G.-C., X.-H. Chen, J.-Y. Li, J. Du, and J.-W. Song, 2011, Seismic noise attenuation using nonstationary polynomial fitting: Applied Geophysics, 8, no. 1, 18-26.

60. Liu, J., and K. J. Marfurt, 2007, Instantaneous spectral attributes to detect channels: Geophysics, 72, no. 2, P23-P31.

61. Magoon, L., and J. W. Schmoker, 2000, The total petroleum system–The natural fluid network that constrains the assessment unit: US geological survey world petroleum assessment, 31.

62. Magoon, L. B. 1992, Petroleum system: Status of research and methods, 1992. Geological Survey, Alexandria, VA (United States).

63. Magoon, L. B., 1995, The play that complements the petroleum system–a new exploration equation: Oil and Gas Journal, 93, no. 40.

64. Magoon, L. B., and W. G. Dow, 1994, The petroleum system: chapter 1: Part I. Introduction.

65. Magoon, L. B., and E. A. Beaumont, 1999, Treatise of Petroleum Geology/Handbook of Petroleum Geology: Exploring for Oil and Gas Traps. Chapter 3: Petroleum Systems.

66. McFadden, P., J. Cook, and L. Forster, 1999, Decomposition of gear vibration signals by the generalised S transform: Mechanical systems and signal processing, 13, no. 5, 691-707.

67. Miao, X., and W. Moon, 1994, Application of the wavelet transform in seismic data processing, SEG Technical Program Expanded Abstracts 1994: Society of Exploration Geophysicists, 1461-1464.

68. Miao, X., and S. Cheadle, 1998, Noise attenuation with wavelet transforms, SEG Technical Program Expanded Abstracts 1998: Society of Exploration Geophysicists, 1072-1075.

69. Michelson, A. A., 1891, XXXVIII. On the application of interference-methods to spectroscopic measurements.—I: The London, Edinburgh, and Dublin Philosophical Magazine and Journal of Science, 31, no. 191, 338-346.

70. Mitchum Jr, R. M., P. R. Vail, and J. B. Sangree, 1977, Seismic stratigraphy and global changes of sea level: Part 6. Stratigraphic interpretation of seismic reflection patterns in depositional sequences: Section 2. Application of seismic reflection configuration to stratigraphic interpretation.

71. Moore, G. E. 1965, Cramming more components onto integrated circuits. McGraw-Hill New York, NY, USA:.

72. Moore, G. E. 1975, Progress in digital integrated electronics. Paper read at Electron devices meeting.

73. Neumann, J. v., 1929, Allgemeine Eigenwerttheorie Hermitescher Funktionaloperatoren. Math: Math. Ann, 102.

74. Newton, I., 1704, Opticks, or, a treatise of the reflections, refractions, inflections & colours of light: Courier Corporation.

75. Noyce, R. N., 1977, Microelectronics: Scientific American, 237, no. 3, 62-69.

76. Oppert, S. K., and R. J. Brown. 2002, Improved Radon transforms for filtering of coherent noise. CREWES Research Report, 14.

77. Ottolini, R., and J. F. Claerbout, 1984, The migration of common midpoint slant stacks: Geophysics, 49, no. 3, 237-249.

78. Partyka, G., J. Gridley, and J. Lopez, 1999, Interpretational applications of spectral decomposition in reservoir characterization: The leading edge, 18, no. 3, 353-360.

79. Parzen, E., 1974, Some recent advances in time series modeling: IEEE Transactions on Automatic Control, 19, no. 6, 723-730.

80. Peters, K., O. Schenk, and B. Wygrala, 2009, Exploration paradigm shift: The dynamic petroleum system concept: Bulletin fuer Angewandte Geologie, 14.

81. Peyton, L., R. Bottjer, and G. Partyka, 1998, Interpretation of incised valleys using new 3-D seismic techniques: A case history using spectral decomposition and coherency: The leading edge, 17, no. 9, 1294-1298.

82. Pinnegar, C. R., and L. Mansinha, 2003, The S-transform with windows of arbitrary and varying shape: Geophysics, 68, no. 1, 381-385.

83. Radon, J., 1917, On the determination of functions from their integrals along certain manifolds: Ber. Verh, Sachs Akad Wiss., 69, 262-277.

84. Ragazzini, J. R., and L. A. Zadeh, 1952, The analysis of sampled-data systems: Transactions of the American Institute of Electrical Engineers, Part II: Applications and Industry, 71, no. 5, 225-234.

85. Reine, C., M. van der Baan, and R. Clark, 2009, The robustness of seismic attenuation measurements using fixed-and variable-window time-frequency transforms: Geophysics, 74, no. 2, WA123-WA135.

86. Remmelts, G., 1996, Salt tectonics in the southern North Sea, the Netherlands, Geology of Gas and Oil under the Netherlands: Springer, 143-158.

87. Robinson, E. A., 1967, Multichannel time series analysis with digital computer programs.

88. Robinson, E. A., 1982, A historical perspective of spectrum estimation: Proceedings of the IEEE, 70, no. 9, 885-907.

89. Sacchi, M. D., and T. J. Ulrych, 1995, High-resolution velocity gathers and offset space reconstruction: Geophysics, 60, no. 4, 1169-1177.

90. Sacchi, M. D., and M. Porsani, 1999, Fast high resolution parabolic Radon transform, SEG Technical Program Expanded Abstracts 1999: Society of Exploration Geophysicists, 1477-1480.

91. Schrödinger, E., 1926, An undulatory theory of the mechanics of atoms and molecules: Physical review, 28, no. 6, 1049.

92. Schrödinger, E., 1928, Four lectures on wave mechanics: London.

93. Schroot, B., and R. Schüttenhelm, 2003, Expressions of shallow gas in the Netherlands North Sea: Netherlands Journal of Geosciences, 82, no. 1, 91-105.

94. Schroot, B. M., G. T. Klaver, and R. T. Schüttenhelm, 2005, Surface and subsurface expressions of gas seepage to the seabed—examples from the Southern North Sea: Marine and Petroleum Geology, 22, no. 4, 499-515.

95. Schuster, A., 1898, On the investigation of hidden periodicities with application to a supposed 26 day period of meteorological phenomena: Terrestrial Magnetism, 3, no. 1, 13-41.

96. Smoluchowski, M. v., 1914, Vortgage uber die Kinetische Theorie der materie und der Elektrizitat: M. Pla. nck et al.,(Teubner und Leipzig, Berlin 1914), 89-121.

97. Stockwell, R. G., 2007, A basis for efficient representation of the S-transform: Digital Signal Processing, 17, no. 1, 371-393.

98. Stockwell, R. G., L. Mansinha, and R. Lowe, 1996, Localization of the complex spectrum: the S transform: IEEE transactions on signal processing, 44, no. 4, 998-1001.

99. Sturm, C., 1836, Sur une classe d'equations a derivee partielle: Journal de Mathématiques Pures et Appliquées, 1, 373-444.

100. Taner, M. T., F. Koehler, and R. Sheriff, 1979, Complex seismic trace analysis: Geophysics, 44, no. 6, 1041-1063.

101. Taylor, B., 1715, Methodus incrementorum directa & inversa: typis Pearsonianis: prostant apud Gul. Innys.

102. Ten Kroode, F., S. Bergler, C. Corsten, J. W. de Maag, F. Strijbos, and H. Tijhof, 2013, Broadband seismic data—The importance of low frequencies: Geophysics, 78, no. 2, WA3-WA14.

103. Thorson, J., and J. Claerbout, 1985, Velocity-stack and slant-stack stochastic inversion: Geophysics.

104. Trad, D., M. D. Sacchi, and T. J. Ulrych, 2001, A hybrid linear-hyperbolic Radon transform: Journal of Seismic Exploration, 9, no. 4, 303-318.

105. Treitel, S., and L. Lines, 1982, Linear inverse theory and deconvolution: Geophysics, 47, no. 8, 1153-1159.

106. Tukey, J., 1949, The sampling theory of power spectrum estimates. Sym: Appl. Autocorrelation Analysis to Phys. Probl NAVEXOS-P-735Office of Naval Research, Washington, DC.

107. Van Adrichem Boogaert, H., and W. Kouwe, 1993, Stratigraphic nomenclature of the Netherlands, revision and update by RGD and NOGEPA.

108. Verma, A., M. Pereira, B. Bharali, A. Khanna, and R. Dasgupta, 2009, Use of spectral decomposition in seismic interpretation for finding out fluvial channel sand body: A case study from upper assam shelf basin, India, SEG Technical Program Expanded Abstracts 2009: Society of Exploration Geophysicists, 598-602.

109. Widess, M., 1973, How thin is a thin bed?: Geophysics, 38, no. 6, 1176-1180.

110. Wiener, N., 1923, Differential-Space: Journal of Mathematics and Physics, 2, no. 1-4, 131-174.

111. Wiener, N., 1930, Generalized harmonic analysis: Acta mathematica, 55, 117-258.

112. Wiener, N., 1949, Extrapolation, interpolation and smoothing of stationary: Time Series, with Engineering Applications.

113. Xiao, G.-j., C.-c. Yang, X.-b. Fan, Y. Leng, and Q. Wu, 2008, Application of spectral decomposition method in channel identifying at W area [J]: Progress in Geophysics, 2.

114. Yilmaz, ö., 1989, Velocity-Stack Processing: Geophysical Prospecting, 37, no. 4, 357-382.

115. Yilmaz, ö., 2001, Seismic data analysis: Processing, inversion, and interpretation of seismic data: Society of exploration geophysicists.

116. Yoon, W. J., and M. Farfour, 2012, Spectral decomposition aids AVO analysis in reservoir characterization: A case study of Blackfoot field, Alberta, Canada: Computers & Geosciences, 46, 60-65.

117. Yule, G. U., 1927, VII. On a method of investigating periodicities disturbed series, with special reference to Wolfer's sunspot numbers: Philosophical Transactions of the Royal Society of London. Series A, Containing Papers of a Mathematical or Physical Character, 226, no. 636-646, 267-298.

118. Zhang, K., K. J. Marfurt, R. M. Slatt, and Y. Guo, 2009, Spectral decomposition illumination of reservoir facies, SEG Technical Program Expanded Abstracts 2009: Society of Exploration Geophysicists, 3515-3519.

119. Zhou, B., and S. A. Greenhalgh, 1994, Linear and parabolic $\tau - p$ transforms revisited: Geophysics, 59, no. 7, 1133-1149.

120. Ziegler, P. A. 1990, Geological atlas of western and central Europe.

5. Appendix

5.1 Lemma 1: Proof that the Fourier transform of a Gaussian is a Gaussian.

The Gaussian is defined as:

$$w(t,\sigma) = \frac{1}{\sqrt{2\pi\sigma^2}} exp\left(\frac{-(\tau-t)^2}{2\sigma^2}\right) \tag{5.1}$$

Take the Fourier transform

$$W(\alpha,\sigma) = \int_{-\infty}^{\infty} w(t,\sigma) exp(-2\pi i\alpha t)dt = \int_{-\infty}^{\infty} \frac{1}{\sqrt{2\pi\sigma^2}} exp\left(\frac{-(\tau-t)^2}{2\sigma^2}\right) exp(-2\pi i\alpha t)dt \tag{5.2}$$

A shift doesn't change the shape of the integral:

$$W(\alpha,\sigma) = \int_{-\infty}^{\infty} \frac{1}{\sqrt{2\pi\sigma^2}} exp\left(\frac{-t^2}{2\sigma^2}\right) exp(-2\pi i\alpha t)dt \tag{5.3}$$

$$W(\alpha,\sigma) = \frac{1}{\sqrt{2\pi\sigma^2}} \int_{-\infty}^{\infty} exp\left(\frac{-t^2}{2\sigma^2} - 2\pi i\alpha t\right)dt \tag{5.4}$$

$$W(\alpha,\sigma) = \frac{1}{\sqrt{2\pi\sigma^2}} \int_{-\infty}^{\infty} exp\left[\frac{-1}{2\sigma^2}\left(t^2 + 4\pi i\alpha\sigma^2 t\right)\right]dt \tag{5.5}$$

Complete the square

$$W(\alpha,\sigma) = \frac{1}{\sqrt{2\pi\sigma^2}} \int_{-\infty}^{\infty} exp\left[\frac{-1}{2\sigma^2}\left(t^2 + 2(2\pi i\alpha\sigma^2)t\right) + (2\pi i\alpha\sigma^2)^2 - (2\pi i\alpha\sigma^2)^2\right]dt \tag{5.6}$$

$$W(\alpha,\sigma) = \frac{1}{\sqrt{2\pi\sigma^2}} exp\left(\frac{-1}{2\sigma^2}(-2\pi i\sigma\alpha^2)^2\right) \int_{-\infty}^{\infty} exp\left(\frac{-1}{2\sigma^2}(t + 2\pi i\alpha\sigma^2)^2\right)dt \tag{5.7}$$

$$W(\alpha,\sigma) = \frac{1}{\sqrt{2\pi\sigma^2}} exp\left(\frac{-1}{2\sigma^2}(-4\pi^2 i^2 \alpha^2 \sigma^4)\right)\left[\int_{-\infty}^{\infty} exp\left(\frac{t^2}{2\sigma^2}\right) dt\right] \tag{5.8}$$

$$W(\alpha,\sigma) = \frac{1}{\sqrt{2\pi\sigma^2}} exp(-2\pi^2\alpha^2\sigma^2)[\sqrt{2\pi\sigma^2}] \tag{5.9}$$

$$W(\alpha,\sigma) = exp\left(-2\pi^2\alpha^2\sigma^2\right) \tag{5.10}$$

$$W(\alpha,\sigma) = exp\left(\frac{-2\pi^2\alpha^2}{f^2}\right) \tag{5.11}$$

Which is a Gaussian window also.

5.2 Lemma 2: Proof of the Integral of a Gaussian

$$Let \quad I = \int_{-\infty}^{\infty} exp(-ax^2)dx \tag{5.12}$$

$$I^2 = \int_{-\infty}^{\infty} exp(-ax^2)dx \int_{-\infty}^{\infty} exp(-ay^2)dy \tag{5.13}$$

$$I^2 = \int_{-\infty}^{\infty}\int_{-\infty}^{\infty} exp(-a(x^2+y^2))dxdy \tag{5.14}$$

Transform to polar coordinates $x = rcos\theta$ and $y = rsin\theta$

$$dx = cos\theta dr - rsin\theta d\theta \tag{5.15}$$

$$dy = sin\theta dr + rcos\theta d\theta \tag{5.16}$$

Jacobian of the transformation

$$dxdy = \begin{bmatrix} cos\theta & rsin\theta \\ sin\theta & rcos\theta \end{bmatrix} drd\theta$$

$$dxdy = r(cos^2\theta + sin^2\theta)drd\theta \tag{5.17}$$

$$dxdy = drd\theta \tag{5.18}$$

$$I^2 = \int_0^{2\pi} \int_0^{\infty} exp(-ar^2)rdrd\theta \tag{5.19}$$

Integrate over θ

$$I^2 = 2\pi \int_0^{\infty} exp(-ar^2)rdr \tag{5.20}$$

Change of variables: $u = r^2$ $du = 2rdr$

$$I^2 = 2\pi \int_0^{\infty} exp(-au)\frac{1}{2}du \tag{5.21}$$

$$I^2 = \frac{\pi}{-a} exp(-au)|_0^{\infty}$$

$$I^2 = \frac{\pi}{-a}[0-1]$$

$$I^2 = \frac{\pi}{a}$$

$$I = \sqrt{\frac{\pi}{a}}$$

5.3 Matlab Code for the Auxiliary S-transform

```
%%%-------------------------------------------------------------------------
%%%---- AST DEMO FIG3_1
%%%-------------------------------------------------------------------------
%%---Requires seislab and cqi_plotmatrix; add to path before running
%%https://www.mathworks.com/matlabcentral/fileexchange/53109-seislab-3-02
%%https://www.mathworks.com/matlabcentral/fileexchange/51122-
    cqi_plotmatrixdata-varargin
%%-------------------------------------------------------------------------



clear all; clc; close all;
temp1=s_create_synthetic_gather(0:4:1000,{'times',200}, ...
        {'moveout','parabolic'},{'offsets',0:8:2000,'m'}, ...
        {'amplitudes',1},{'velocities', 900});

temp2=s_create_synthetic_gather(0:4:1000,{'times',300}, ...
        {'moveout','linear'},{'offsets',0:8:2000,'m'}, ...
        {'amplitudes',1},{'velocities', 1050});

temp3=s_create_synthetic_gather(0:4:1000,{'times',500}, ...
        {'moveout','linear'},{'offsets',0:8:2000,'m'}, ...
        {'amplitudes',1},{'velocities', 2500});


st1=temp1.traces;
st2=temp2.traces;
st3=temp3.traces;

hl=100;
st=st1+st2+st3;
```

```
stt=st(:,1:hl);
stt=padarray(stt,[100,10]);

seis2ev_par_lin=temp2;
seis2ev_par_lin.traces=stt;
[nt,nh]=size(seis2ev_par_lin.traces);
seis2ev_par_lin.headers=1:nh;
t=[0:nt-1]*4*10^-3;

seismic=s_filter(seis2ev_par_lin,{'ormsby',[0,20,40,100]});
seismic.step=0.004;seismic.last=1.8;
seis2ev_par_lin=seismic;
data=seis2ev_par_lin.traces;
h=seis2ev_par_lin.headers;

fntsz=10;
y1=t(80); y2=t(nt-80);
x1=10;x2=nh-10;
sc=0.0015;
scc=0.001;
%%%%%------------------------------------------------------------------------


pow=1; %change to 2 for parabolic


if pow ==1
nq=3000;q1=linspace(0, 1.3,nq);%linear  %%reduce nq to 1000 for speed
end
if pow==2
nq=1000;q1=linspace(0,60,nq);%parabolic
end

```

```
mode1=1; %inverse rad
mode2=-1; %forward rad
%%-------------------------------------------------------------------------

tic
slowstruct=radls(data,t,h,q1,pow,mode1);
slowdata=slowstruct.output;
datarad=slowdata;
toc

[nt,nh]=size(datarad);

tic
for kk=1: nh
trace1=datarad(:,kk);
factor=1;
samplingrate=.004;
[st,tt,f]=str1d(trace1,factor,samplingrate);
Rdatst(:,kk,:)=abs(st);
ist=invstr(st);
Ristinv(:,kk)=ist';
end
RistinvStruct.output=Ristinv;RistinvStruct.sc=slowstruct.sc;
DataRECstruct=radls(RistinvStruct,t,h,q1,pow,-1);
DataREC=DataRECstruct.output;
toc



%%%%----plot-----------------------------------------------------
figure('units','normalized','outerposition',[0 0 1/2 1])
subplot(321)
cqi_plotmatrix(data,'dt',.004,'t0',0,'scale',2,'skip',1,'fillco','k','
```

```
    linewidth',1,'unit','s');
set(gca,'fontsize',fntsz,'Xaxislocation','bottom')
ylim([y1 y2]);xlim([x1 x2]);
title('(a) Original Data')
box on;
xlabel('Trace');

tic
subplot(322)
slowdata(256:451,:)=0;
ind=find(q1 >=1.025 & q1 <=1.037);
slowdataV=slowdata(:,ind);
q1V=q1(ind);
cqi_plotmatrix(slowdataV,'traceIndex',q1V,'dt',.004,'t0',0,'scale',sc,'skip'
    ,0,'fillco','k','linewidth',1,'unit','s');
set(gca,'fontsize',fntsz,'Xaxislocation','bottom')
ylim([y1 y2]);
xlim([1.025 1.037])
xlabel('p (s/m)');
ylabel('Tau (s)');
box on;
title('(b) LRT')
toc

tic
subplot(3,2,3)
RdatstV=Rdatst(:,ind,:);
RdatstV=RdatstV./max(abs(RdatstV),[],'all');
szarray=size(RdatstV);
[y,x,z] = meshgrid(q1V,f,t);
slice(y, x, z,RdatstV,[],[10:10:50],[])
shading('interp');colormap('jet');
zlim([y1 y2]);
```

```
xlim([1.025 1.037])
set(gca,'fontsize',fntsz)
set(gca,'Zdir','reverse')
set(gca,'Ydir','reverse')
caxis([0.02 0.9])
[az,el] = view;
view([ -65 30])
title('(c) AST Volume')
box on;
ylabel('Frequency (Hz)');zlabel('\eta (s)');xlabel('p (s/m)');
toc

tic
subplot(324)
Ristinv(256:451,:)=0;
RistinvV=Ristinv(:,ind);
cqi_plotmatrix(RistinvV,'traceIndex',q1V,'dt',.004,'t0',0,'scale',sc,'skip',0,
    'fillco','k','linewidth',1,'unit','s');
set(gca,'fontsize',fntsz,'Xaxislocation','bottom')
ylim([y1 y2]);xlim([1.025 1.037])
title('(d) Inverse ST')
box on;
xlabel('Trace');
ylabel('Tau (s)');
toc

subplot(325)
cqi_plotmatrix(DataREC,'dt',.004,'t0',0,'scale',2,'skip',1,'fillco','k','
    linewidth',1,'unit','s');
set(gca,'fontsize',fntsz,'Xaxislocation','bottom')
ylim([y1 y2]);xlim([x1 x2]);
title('(e) Reconstructed Data')
box on;
```

```
xlabel('Trace');

subplot(326)
resid=data-DataREC;
scc=max(min(resid./data,[],'all'),scc);
cqi_plotmatrix(resid,'dt',.004,'t0',0,'scale',scc,'skip',2,'fillco','k','
    linewidth',1,'unit','s');
set(gca,'fontsize',fntsz,'Xaxislocation','bottom')
ylim([y1 y2]);xlim([x1 x2]);
title('(f) Residual')
box on;
xlabel('Trace');



%%%-------------------------------------------------------------------------
%%%---- AST DEMO FIG3_4
%%%-------------------------------------------------------------------------


clear all; clc;
temp1=s_create_synthetic_gather(0:4:1000,{'times',200}, ...
        {'moveout','parabolic'},{'offsets',0:8:2000,'m'}, ...
        {'amplitudes',1},{'velocities', 900});

temp2=s_create_synthetic_gather(0:4:1000,{'times',500}, ...
        {'moveout','parabolic'},{'offsets',0:8:2000,'m'}, ...
        {'amplitudes',1},{'velocities', 950});

temp3=s_create_synthetic_gather(0:4:1000,{'times',600}, ...
        {'moveout','linear'},{'offsets',0:8:2000,'m'}, ...
        {'amplitudes',1},{'velocities', 5500});

```

```
191
192 st1=temp1.traces;
193 st2=temp2.traces;
194 st3=temp3.traces;
195
196 hl=100;
197 st=st1+st2+st3;
198 stt=st(:,1:hl); %%stt(:,1:5)=0;stt(:,95:100)=0;
199 stt=padarray(stt,[100,10]);
200
201 seis2ev_par_lin=temp2;
202 seis2ev_par_lin.traces=stt;
203 [nt,nh]=size(seis2ev_par_lin.traces);
204 seis2ev_par_lin.headers=1:nh;
205 t=[0:nt-1]*4*10^-3;
206
207 seismic=s_filter(seis2ev_par_lin,{'ormsby',[0,20,40,100]});
208 seismic.step=0.004;seismic.last=1.8;
209 seis2ev_par_lin=seismic;
210
211
212
213 fntsz=10;
214 y1=t(80); y2=t(nt-80);
215 x1=10;x2=nh-10;
216 sc=.5;
217 scc=0.001;
218
219 data=seis2ev_par_lin.traces;
220 h=seis2ev_par_lin.headers;
221 %%%%s_wplot(seis2ev_par_lin);
222 %%-------------------------------------------------------------------------
223
```

```
224
225 pow=2;
226
227 if pow ==1
228 nq=1000;q1=linspace(-1, 1.3,nq);%linear  %%reduce nq to 1000 for quick run
229 end
230 if pow==2
231 nq=1000;q1=linspace(-10,50,nq);%linear
232 end
233
234 mode1=1; %inverse rad
235 mode2=-1; %forward rad
236 %%-------------------------------------------------------------------------
237
238 slowstruct=radls(data,t,h,q1,pow,mode1);
239 slowdata=slowstruct.output;
240 datarad=slowdata;
241
242 [nt,nh]=size(datarad);
243
244 for kk=1: nh
245 trace1=datarad(:,kk);
246 factor=1;
247 samplingrate=.004;
248 [st,tt,f]=str1d(trace1,factor,samplingrate);
249 Rdatst(:,kk,:)=abs(st);
250 ist=invstr(st);
251 Ristinv(:,kk)=ist';
252 end
253 RistinvStruct.output=Ristinv;RistinvStruct.sc=slowstruct.sc;
254 DataRECstruct=radls(RistinvStruct,t,h,q1,pow,-1);
255 DataREC=DataRECstruct.output;
256
```

```
257
258 % %%%--------------------------------------
259
260
261 %%%%----plot------------------------------------------------------------
262 figure('units','normalized','outerposition',[0 0 1/2 1])
263 subplot(321)
264 cqi_plotmatrix(data,'dt',.004,'t0',0,'scale',2,'skip',1,'fillco','k','
    linewidth',1,'unit','s');
265 set(gca,'fontsize',fntsz,'Xaxislocation','bottom')
266 ylim([y1 y2]);xlim([x1 x2]);
267 title('(a) Original Data')
268 box on;
269 xlabel('Trace');
270
271 subplot(322)
272 cqi_plotmatrix(slowdata,'traceIndex',q1,'dt',.004,'t0',0,'scale',sc,'skip',2,'
    fillco','k','linewidth',1,'unit','s');
273 set(gca,'fontsize',fntsz,'Xaxislocation','bottom')
274 ylim([y1 y2]);
275 xlim([-3 4])
276 xlabel('q (s/m^2)');ylabel('Tau (s)');
277 box on;
278 title('(b) PRT')
279
280 subplot(3,2,3)
281 RdatstV=Rdatst./max(abs(Rdatst),[],'all');
282 szarray=size(Rdatst);
283 [y,x,z] = meshgrid(q1,f,t);
284 slice(y, x, z,Rdatst,[],[10:10:50],[])
285 shading('interp');colormap('jet');
286 zlim([y1 y2]);
287 xlim([-3 4])
```

```
set(gca,'fontsize',fntsz)
set(gca,'Zdir','reverse')
set(gca,'Ydir','reverse')
%caxis([0.02 0.9])
[az,el] = view;
view([ -70 30])
title('(c) AST Volume')
box on;
ylabel('Frequency (Hz)');zlabel('\eta (s)');xlabel('q (s/m^2)');


subplot(324)
cqi_plotmatrix(Ristinv,'traceIndex',q1,'dt',.004,'t0',0,'scale',sc,'skip',2,'
    fillco','k','linewidth',1,'unit','s');
set(gca,'fontsize',fntsz,'Xaxislocation','bottom')
ylim([y1 y2]);xlim([-3 4])
title('(d) Inverse ST')
box on;
xlabel('q (s/m^2)');ylabel('Tau (s)');

subplot(325)
cqi_plotmatrix(DataREC,'dt',.004,'t0',0,'scale',2,'skip',1,'fillco','k','
    linewidth',1,'unit','s');
set(gca,'fontsize',fntsz,'Xaxislocation','bottom')
ylim([y1 y2]);xlim([x1 x2]);
title('(e) Reconstructed Data')
box on;
xlabel('Trace');

subplot(326)
resid=data-DataREC;
scc=max(min(resid./data,[],'all'),scc);
cqi_plotmatrix(resid,'dt',.004,'t0',0,'scale',scc,'skip',1,'fillco','k','
```

```
   linewidth',1,'unit','s');
set(gca,'fontsize',fntsz,'Xaxislocation','bottom')
ylim([y1 y2]);xlim([x1 x2]);
title('(f) Residual')
box on;
xlabel('Trace');




%%%-------------------------------------------------------------------------
function outstruct = radls(input,t,h,q,power,md)

dt   = t(2) - t(1);
nt   = length(t);
nh   = length(h);
nq   = length(q);
nfft = 2*(2^nextpow2(nt));


if md == 1  %%%%space to slowness
[sc,inputnorm]=tracenorm(input);
if power==2; h=h/max(abs(h));end
mu = 10^12;


 output = zeros(nfft,nq);
 D = fft(inputnorm,nfft,1)/sqrt(nfft);

 M = zeros(nfft,nq);
 i = sqrt(-1);

 Q = eye(nq)*nh;
```

```
351
352  for ifreq=2:floor(nfft/2)
353
354   f = 2.*pi*(ifreq-1)/nfft/dt;
355   L = exp(i*f*(h.^power)'*q);
356   y = D(ifreq,:)';
357   xa = L'*y;
358   A = L'*L + mu*Q;
359
360   x  =  A\xa;
361
362
363
364  M(ifreq,:) = x';
365  M(nfft+2-ifreq,:) = conj(x)';
366
367 end
368
369  M(nfft/2+1,:) = zeros(1,nq);
370  output = real(ifft(M,[],1)*sqrt(nfft));
371  output = output(1:nt,:);
372  outstruct.output=output;
373  outstruct.sc=sc;
374 return
375
376 %%-----------------------------------------------------------------
377 else %%slowness to space
378 %%-----------------------------------------------------------------
379  insub=input.output;
380  insc=input.sc;
381  output = zeros(nfft,nh);
382  M = fft(insub,nfft,1)/sqrt(nfft);
383  i = sqrt(-1);
```

```
if power==2; h=(h/max(abs(h))).^2; end

 for ifreq=2:floor(nfft/2)
  f = 2.*pi*(ifreq-1)/nfft/dt;
  L = exp(i*f*(h'*q  ));
  x = M(ifreq,:)';
  y = L * x;
  D(ifreq,:) = y';
  D(nfft+2-ifreq,:) = conj(y)';
 end

 D(nfft/2+1,:) = zeros(1,nh);
 output = real(ifft(D,[],1)*sqrt(nfft));
 output = output(1:nt,:);
[~,output2]=tracenorm(output);

 outstruct.output=output2.*insc;
 outstruct.sc=1;
return;

end
end


function out = invstr(S)
N=size(S,2);
for ii=1:size(S,1)
    ss(ii)=sum(S(ii,:));
end
ss_real=real(ss);
ss_imag=imag(ss);
ss_imag(1:round(N/2))=-1*ss_imag(1:round(N/2));
ss=ss_real+(1i*ss_imag);
```

```
ist=real(ifft(ss,N));
out=fliplr(ist);
end


function [m,out]=tracenorm(in)
m=max(in);
out=in./m;
out(isnan(out))=0;
end

function [str,t,f]=str1d(data,factor,smp)
tmsr=data;
minf = 0;
maxf = fix(length(tmsr)/2);
freqsmp=1;
t = (0:length(tmsr)-1)*smp;
nele =ceil((maxf - minf+1)/freqsmp) ;
f = (minf + [0:nele-1]*freqsmp)/(smp*....
length(tmsr));
n=length(tmsr);
vec=fft(tmsr);
vec=[vec,vec];
str=zeros(ceil((maxf - minf+1)/freqsmp),n);
if minf == 0
str(1,:) = mean(tmsr)*(1&[1:1:n]);
else
str(1,:)=ifft(vec(minf+1:minf+n).*...
gauss(n,minf,factor));
end
for i=freqsmp:freqsmp:(maxf-minf)
      str(i/freqsmp+1,:)=ifft(vec(minf+i+1:minf+i+n).*...
gauss(n,minf+i,factor));
```

```
end
end

function ga=gauss(len,freq,factor)
 vac(1,:)=[0:len-1];
 vac(2,:)=[-len:-1];
 vac=vac.^2;
 vac=vac*(-factor*2*pi^2/freq^2);
 ga=sum(exp(vac));
end
```

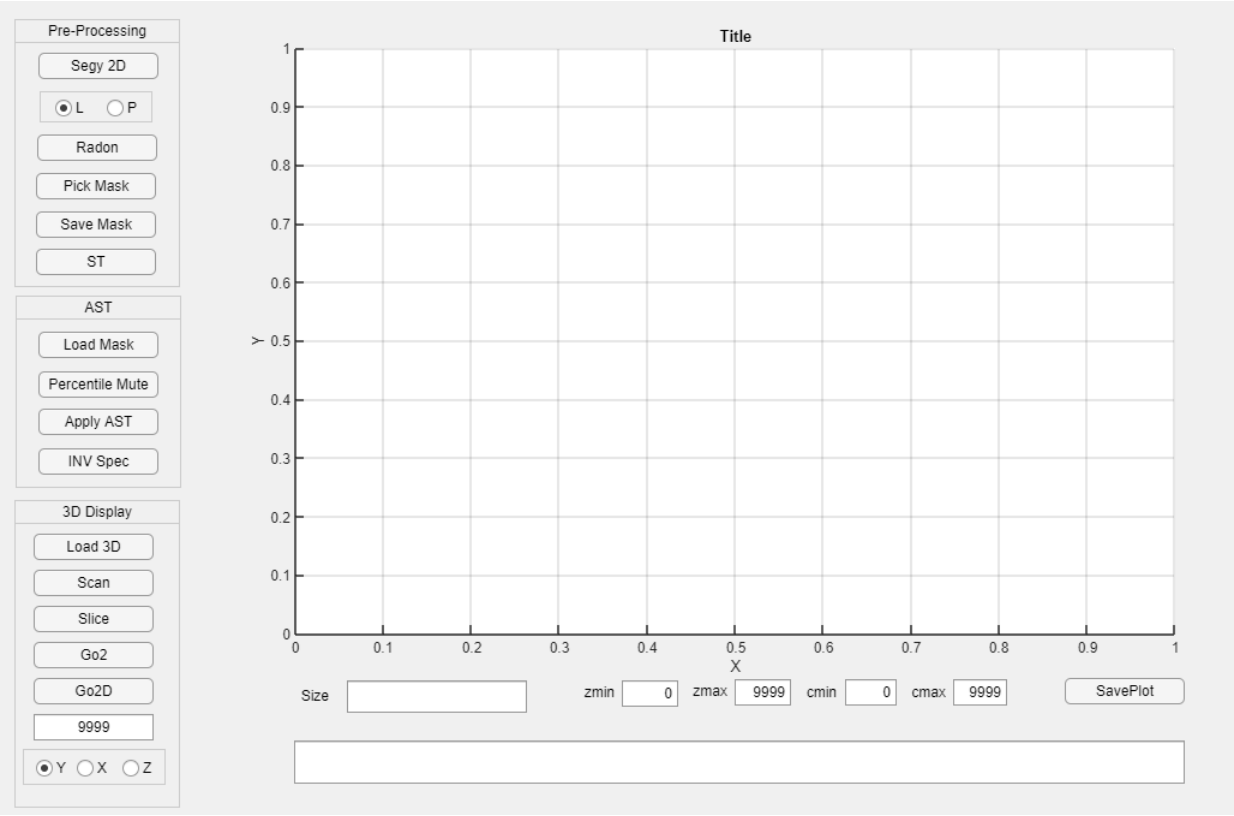

Figure 5.1: Matlab GUI for the Auxiliary S-transform.

5.4 Matlab Code for the Critical Moment Estimation

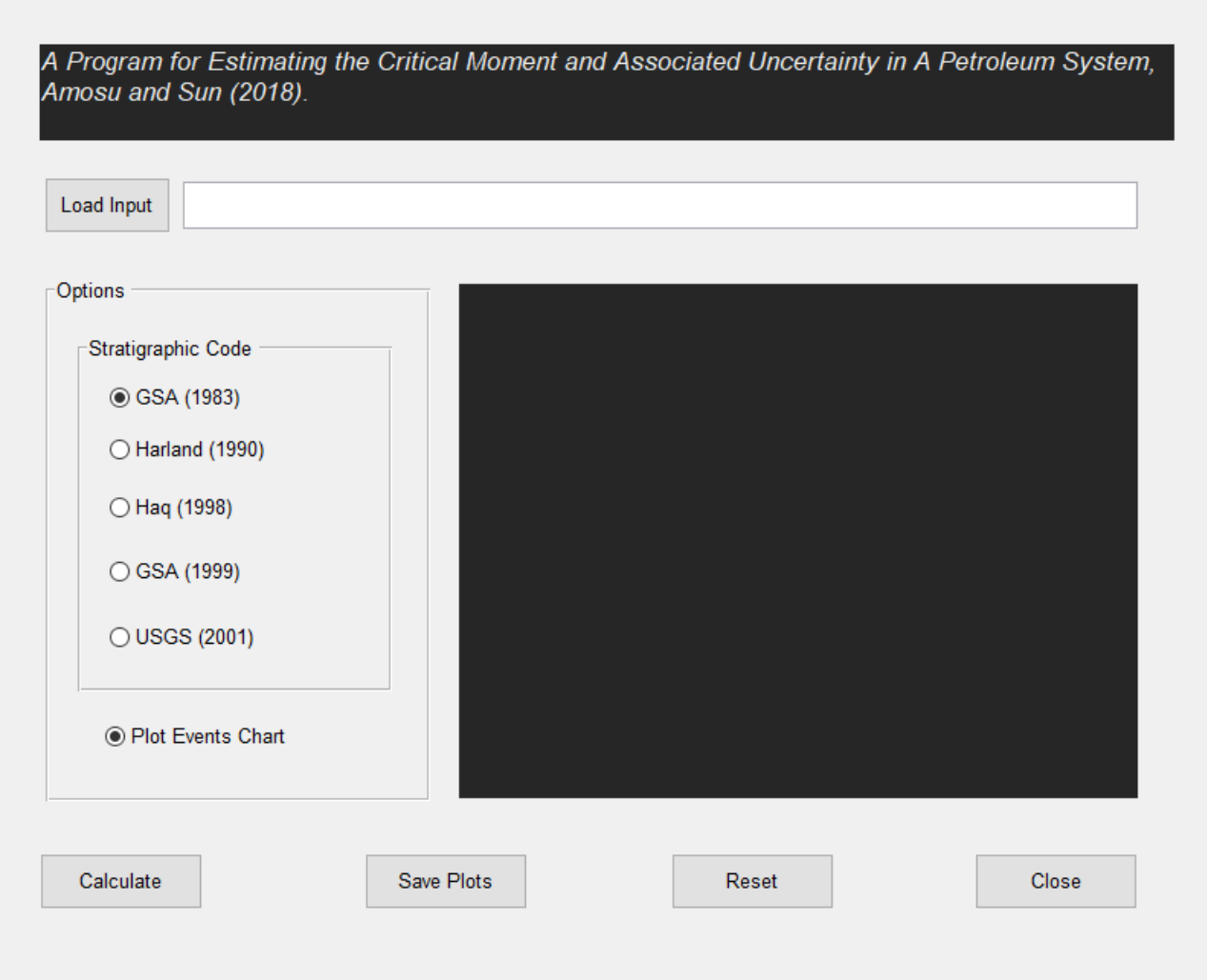

Figure 5.2: Matlab GUI for estimating the critical moment.

```
function varargout = QPFA(varargin)
% QPFA MATLAB code for QPFA.fig
%      QPFA, by itself, creates a new QPFA or raises the existing
%      singleto n*.
%
%      H = QPFA returns the handle to a new QPFA or the handle to
%      the existing singleton*.
%
%      QPFA('CALLBACK',hObject,eventData,handles,...) calls the local
%      function named CALLBACK in QPFA.M with the given input arguments.
%
%      QPFA('Property','Value',...) creates a new QPFA or raises the
%      existing singleton*.  Starting from the left, property value pairs are
%      applied to the GUI before QPFA_OpeningFcn gets called.  An
%      unrecognized property name or invalid value makes property application
%      stop.  All inputs are passed to QPFA_OpeningFcn via varargin.
%
%      *See GUI Options on GUIDE's Tools menu.  Choose "GUI allows only one
%      instance to run (singleton)".
%
% See also: GUIDE, GUIDATA, GUIHANDLES

% Edit the above text to modify the response to help QPFA

% Last Modified by GUIDE v2.5 12-Nov-2017 20:50:28
%------------------------------------------------------------------




% Begin initialization code - DO NOT EDIT
gui_Singleton = 1;
gui_State = struct('gui_Name',       mfilename, ...
```

```
34                    'gui_Singleton',  gui_Singleton, ...
35                    'gui_OpeningFcn', @QPFA_OpeningFcn, ...
36                    'gui_OutputFcn',  @QPFA_OutputFcn, ...
37                    'gui_LayoutFcn',  [] , ...
38                    'gui_Callback',   []);
39 if nargin && ischar(varargin{1})
40     gui_State.gui_Callback = str2func(varargin{1});
41 end
42
43 if nargout
44     [varargout{1:nargout}] = gui_mainfcn(gui_State, varargin{:});
45 else
46     gui_mainfcn(gui_State, varargin{:});
47 end
48 % End initialization code - DO NOT EDIT
49
50
51 % --- Executes just before QPFA is made visible.
52 function QPFA_OpeningFcn(hObject, eventdata, handles, varargin)
53 % This function has no output args, see OutputFcn.
54 % hObject    handle to figure
55 % eventdata  reserved - to be defined in a future version of MATLAB
56 % handles    structure with handles and user data (see GUIDATA)
57 % varargin   command line arguments to QPFA (see VARARGIN)
58
59 % Choose default command line output for QPFA
60 handles.output = hObject;
61
62 % Update handles structure
63 guidata(hObject, handles);
64
65 % UIWAIT makes QPFA wait for user response (see UIRESUME)
66 % uiwait(handles.figure1);
```

```
67
68
69 % --- Outputs from this function are returned to the command line.
70 function varargout = QPFA_OutputFcn(hObject, eventdata, handles)
71 % varargout  cell array for returning output args (see VARARGOUT);
72 % hObject    handle to figure
73 % eventdata  reserved - to be defined in a future version of MATLAB
74 % handles    structure with handles and user data (see GUIDATA)
75
76 % Get default command line output from handles structure
77 varargout{1} = handles.output;
78
79
80
81 function edit1_Callback(hObject, eventdata, handles)
82 % hObject    handle to edit1 (see GCBO)
83 % eventdata  reserved - to be defined in a future version of MATLAB
84 % handles    structure with handles and user data (see GUIDATA)
85
86 % Hints: get(hObject,'String') returns contents of edit1 as text
87 %        str2double(get(hObject,'String')) returns contents of edit1 as a
       double
88
89
90 % --- Executes during object creation, after setting all properties.
91 function edit1_CreateFcn(hObject, eventdata, handles)
92 % hObject    handle to edit1 (see GCBO)
93 % eventdata  reserved - to be defined in a future version of MATLAB
94 % handles    empty - handles not created until after all CreateFcns called
95
96 % Hint: edit controls usually have a white background on Windows.
97 %       See ISPC and COMPUTER.
98 if ispc && isequal(get(hObject,'BackgroundColor'),...
```

```
        get(0,'defaultUicontrolBackgroundColor'))
    set(hObject,'BackgroundColor','white');
end


% --- Executes on button press in pushbutton1.
function pushbutton1_Callback(hObject, eventdata, handles)
% hObject    handle to pushbutton1 (see GCBO)
% eventdata  reserved - to be defined in a future version of MATLAB
% handles    structure with handles and user data (see GUIDATA)
warning off;
[PathName,FileName] = uigetfile({'*.xlsx'},'Select the Data file');
if (FileName == 0)
set(handles.edit2,'String','Input file is not selected')
pause(1)
set(handles.edit2,'String','')
return;
end

filein=fullfile(FileName,PathName);
set(handles.edit2,'String',['Selected Input file: ' filein]) ;

%store data
[elems, petData]=getpetData(filein);
f = figure;
t = uitable(f,'Data',petData,'Position',[20 20 500 350]);
handles.elems=elems;

n_ys=find(~cellfun(@isempty,elems));
nsubp=(length(n_ys)+1);
n_no=find(cellfun(@isempty,elems));
nind(1:7)=1;nind(n_no)=0;

```

```
132 handles.nsubp=nsubp;
133 handles.nind=nind;
134 guidata(hObject,handles);
135
136
137 function edit2_Callback(hObject, eventdata, handles)
138 % hObject    handle to edit2 (see GCBO)
139 % eventdata  reserved - to be defined in a future version of MATLAB
140 % handles    structure with handles and user data (see GUIDATA)
141
142 % Hints: get(hObject,'String') returns contents of edit2 as text
143 %        str2double(get(hObject,'String')) returns contents of edit2 as a
    double
144
145
146 % --- Executes during object creation, after setting all properties.
147 function edit2_CreateFcn(hObject, eventdata, handles)
148 % hObject    handle to edit2 (see GCBO)
149 % eventdata  reserved - to be defined in a future version of MATLAB
150 % handles    empty - handles not created until after all CreateFcns called
151
152 % Hint: edit controls usually have a white background on Windows.
153 %       See ISPC and COMPUTER.
154 if ispc && isequal(get(hObject,'BackgroundColor'),...
155         get(0,'defaultUicontrolBackgroundColor'))
156     set(hObject,'BackgroundColor','white');
157 end
158
159
160 % --- Executes on button press in pushbutton2.
161 function pushbutton2_Callback(hObject, eventdata, handles)
162 % hObject    handle to pushbutton2 (see GCBO)
163 % eventdata  reserved - to be defined in a future version of MATLAB
```

```
% handles    structure with handles and user data (see GUIDATA)

%get strat code
u = get(get(handles.uibuttongroup1,'SelectedObject'), 'Tag');
if strcmp(u,'radiobutton1')
[levelss,ncol]=choose_time_scale('GSA1983');
elseif strcmp(u,'radiobutton2')
[levelss,ncol]=choose_time_scale('HARLAND1990');
elseif strcmp(u,'radiobutton3')
[levelss,ncol]=choose_time_scale('HAQ1998');
elseif strcmp(u,'radiobutton4')
[levelss,ncol]=choose_time_scale('GSA1999');
elseif strcmp(u,'radiobutton5')
[levelss,ncol]=choose_time_scale('USGS2001');
end
handles.levelss=levelss;
handles.ncol=ncol;

if ~isfield(handles,'elems')
  set(handles.edit2,'String',' Warning: First Load Data ')
  return
end

%close open figures
set(QPFA, 'HandleVisibility', 'off');
close all;
set(QPFA, 'HandleVisibility', 'on');

set(handles.edit2,'String',' Please Wait ...')
if isfield(handles,'saveFlag')
    saveFlag = handles.saveFlag;
else
    saveFlag = 0;
```

```
end
[minall, maxall,elemval,cricUL,cricUP,cricD,cricM,uncertainty]=rankSCAL(
    handles.elems,handles);
set(handles.edit2,'String','')
unt=' Ma';
result_str=[{'Results:'},{''},{[' Early Limit: ' num2str(cricUL) unt]},{['
    Early Bound: ' num2str(cricUP) unt]},...
     { [' Best Estimate Critical Moment: '  num2str(cricM) unt]},{['
    Uncertainty: ' num2str(uncertainty) unt]},...
     {[' Late Bound: ' num2str(cricD) unt]},{' Late Limit: Present day'},{''},{
    ' For Theory See: Amosu and Sun (2018), A Quantitative Probabilistic
    Framework for Estimating the Critical Moment in a Petroleum System, AAPG
    Bulletin'}];

set(handles.edit2,'String','')
set(handles.text4,'String',result_str)
guidata(hObject,handles);

u2=get(handles.radiobutton6,'Value');
if (u2 == 1)
plotEventChart(levelss,elemval,cricUL,cricUP,cricD,cricM,ncol,minall,maxall);
if (isfield(handles,'saveFlag') && handles.saveFlag==1)
saveas(gcf, handles.saveName5,'fig');
saveas(gcf, handles.saveName6,'png');
close(gcf);
end

end

guidata(hObject,handles);


```

```
% --- Executes on button press in pushbutton4.
function pushbutton4_Callback(hObject, eventdata, handles)
% hObject    handle to pushbutton4 (see GCBO)
% eventdata  reserved - to be defined in a future version of MATLAB
% handles    structure with handles and user data (see GUIDATA)
if ~isfield(handles,'elems')
  set(handles.edit2,'String',' Warning: First Load Data ')
  return
end
handles.saveFlag=1;
guidata(hObject,handles);

set(handles.edit2,'String','Please Wait...Saving Plots')
mkdir('./QPFA_Output');
PathName='./QPFA_Output';
datvarnam=datestr(now, 'dd_mmm_yyyy_HH_MM_SS');
FileName1a=['QPF1_',datvarnam,'.fig'];
FileName1b=['QPF1_',datvarnam,'.png'];
FileName1c=['QPF2_',datvarnam,'.fig'];
FileName1d=['QPF2_',datvarnam,'.png'];
FileName1e=['QPF3_',datvarnam,'.fig'];
FileName1f=['QPF3_',datvarnam,'.png'];
handles.saveName1 = fullfile(PathName,FileName1a);
handles.saveName2 = fullfile(PathName,FileName1b);
handles.saveName3 = fullfile(PathName,FileName1c);
handles.saveName4 = fullfile(PathName,FileName1d);
handles.saveName5 = fullfile(PathName,FileName1e);
handles.saveName6 = fullfile(PathName,FileName1f);

pushbutton2_Callback(hObject, eventdata, handles);
handles.saveFlag=0;
set(handles.edit2,'String','Done')
guidata(hObject,handles);
```

```
257
258
259 % --------------------------------------------------------------------
260 function [levelss,ncol]=choose_time_scale(tscal)
261 addpath('dependencies')
262   switch tscal
263     case 'GSA1983'
264         gsa1983=readtable('geol_time_lab.xlsx','Sheet','GSA1983');
265         level1=gsa1983(1:7,:);level2=gsa1983(9:21,:);
266         level3=gsa1983(23:32,:);level4=gsa1983(34:37,:);
267         levelss={level1;level2;level3;level4};
268         ncol=37;
269         clearvars gsa1983 leve11 level2 level3 level4;
270     case 'HARLAND1990'
271         harland1990=readtable('geol_time_lab.xlsx','Sheet','HARLAND1990');
272          level1=harland1990(1:7,:);level2=harland1990(9:21,:);
273          level3=harland1990(23:28,:);level4=harland1990(30:32,:);
274          levelss={level1;level2;level3;level4};
275          ncol=32;
276          clearvars harland1990 leve11 level2 level3 level4;
277     case 'HAQ1998'
278         haq1998=readtable('geol_time_lab.xlsx','Sheet','HAQ1998');
279         level1=haq1998(1:7,:);level2=haq1998(9:21,:);
280         level3=haq1998(23:32,:);level4=haq1998(34:37,:);
281         levelss={level1;level2;level3;level4};
282         ncol=37;
283         clearvars haq1998 leve11 level2 level3 level4;
284     case 'GSA1999'
285         gsa1999=readtable('geol_time_lab.xlsx','Sheet','GSA1999');
286         level1=gsa1999(1:7,:);level2=gsa1999(9:21,:);
287         level3=gsa1999(23:32,:);level4=gsa1999(34:37,:);
288         levelss={level1;level2;level3;level4};
289         ncol=37;
```

```
290         clearvars gsa1999 leve11 level2 level3 level4;
291     case 'USGS2001'
292         usgs2001=readtable('geol_time_lab.xlsx','Sheet','USGS2001');
293         level1=usgs2001(1:7,:);level2=usgs2001(9:21,:);
294         level3=usgs2001(23:26,:);level4=usgs2001(28:31,:);
295         levelss={level1;level2;level3;level4};
296         ncol=31;
297         clearvars usgs2001 leve11 level2 level3 level4;
298   end%%%endswitch
299
300
301 % ------------------------------------------------------------------------
302
303 function [elems, petData]=getpetData(filein)
304 [~, ~, petData]=xlsread(filein);
305 %%keywords have to match in file
306 SR = petData(strcmp(petData(:,1),'Source Rock'),:);
307 RR = petData(strcmp(petData(:,1),'Reservoir Rock'),:);
308 OV = petData(strcmp(petData(:,1),'Overburden'),:);
309 SL = petData(strcmp(petData(:,1),'Seal Rock'),:);
310 TF = petData(strcmp(petData(:,1),'Trap Formation'),:);
311 GMA= petData(strcmp(petData(:,1),'Generation Migration and Accumulation'),:);
312 PR = petData(strcmp(petData(:,1),'Preservation Time'),:);
313 elems={SR;RR;SL;OV;TF;GMA;PR};
314
315 % ------------------------------------------------------------------------
316
317 function hfig1=plotEventChart(levelss,elemval,cricUL,cricUP,cricD,cricM,ncol,
      minall,maxall)
318 hfig1=figure(4);
319 set(hfig1,'units','normalized','outerposition',[0 0 0.98 0.98]);
320 xr=[0 -100 -100 0];yr=[-100 -100 100 100];
321 %patch(xr,yr,[1 1 1])
```

```
322
323 col=plotscale(levelss,ncol,minall,maxall);
324 col2=flipud(col);
325 col2(1:7,:)=[0 0 0; 0 0.5 0; 0 0 1;1 0 0;0.8 0.5 0; 0 1 0; 0.5 0.5 0.4];
326
327
328 elestring={'Source Rock';'Reservoir Rock';'Seal Rock';'Overburden';...
329     'Trap Formation';{'Generation'; 'Migration'; 'Accumulatiom'};...
330     'Preservation';{'Critical Range &'; 'Critical Moment'}};
331 count=0;
332
333 for kk=1:length(elemval)
334 if ~isnan(elemval{kk});if ~isempty(elemval{kk})
335  val=elemval{kk};
336  for jj=1:2:length(val)
337  xx=[val(jj) val(jj+1) val(jj+1) val(jj)];
338  yy=[count-1 count-1 count count];
339  patch(xx,yy,col2((-count+1),:),'FaceAlpha',1);
340  text(minall-1,count-0.5,elestring{kk,:},'Fontsize',15,'Fontweight','bold','
       Color','k');
341  end
342  count=count-1;
343  clear val;
344 end;end
345 end
346 mksz=28;
347 for mm=kk+1:kk+1
348     plot(cricUL,count-0.5,'ks','Markersize',mksz+10,'MarkerFacecolor','k');
       hold on
349     line([ cricUP cricD],[count-0.5 count-0.5],'Linewidth',2,'Color','k');
       hold on;
350     plot(cricUP,count-0.5,'b^','Markersize',mksz-2,'MarkerFacecolor','b');hold
        on
```

```
351     %if (cricUP == cricD); mksz=mksz-8; end
352      plot(cricD,count-0.5,'ro','Markersize',mksz-4,'MarkerFacecolor','r');hold
         on;
353     % if (cricM == cricD); mksz=mksz-8; end
354      plot(cricM,count-0.5,'gh','Markersize',mksz-8,'MarkerFacecolor',[0
        0.3906         0]);hold on
355     %text(pos+2.5,count-0.5,'\uparrow','Fontsize',50,'Fontweight','bold','
        Color','r')%2.5 corrects for arrow head length
356     text(minall-1,count-0.5,elestring{8,:},'Fontsize',15,'Fontweight','bold','
        Color','k');
357     count=count-1;
358 end
359 grid on; grid minor;
360 xlabel('Time (m.y.)','Fontsize',35)
361 set(gca,'Fontweight','bold','Fontsize',30,'Yticklabel',[],'XColor','k','Ycolor
        ','k');
362 ylim([count 3]);
363 box on;
364
365
366
367 % ------------------------------------------------------------------------
368
369
370
371 function [minall, maxall,elemval,cricUL,cricUP,cricD,cricM,uncertainty]=
        rankSCAL(elems,handles)
372
373 %%sourcerock
374 sr=elems(1);sr=sr{1,1};[nsr,~]=size(sr);
375 srval=cell2mat(reshape(sr(1:nsr,2:3)',1,[]));
376
377 %%reservoir rock
```

```
rr=elems(2);rr=rr{1,1};[nrr,~]=size(rr);
rrval=cell2mat(reshape(rr(1:nrr,2:3)',1,[]));

%%seal rock
sl=elems(3);sl=sl{1,1};[nsl,~]=size(sl);
slval=cell2mat(reshape(sl(1:nsl,2:3)',1,[]));

%%overburden rock
ov=elems(4);ov=ov{1,1};[nov,~]=size(ov);
ovval=cell2mat(reshape(ov(1:nov,2:3)',1,[]));

%%%%trapformation
tf=elems(5);tf=tf{1,1};[ntf,~]=size(tf);
tfval=cell2mat(reshape(tf(1:ntf,2:3)',1,[]));

%%GMA
gma=elems(6);gma=gma{1,1};[ngma,~]=size(gma);
gmaval=cell2mat(reshape(gma(1:ngma,2:3)',1,[]));

%%Preservation time
pt=elems(7);pt=pt{1,1};[npt,~]=size(pt);
ptval=cell2mat(reshape(pt(1:npt,2:3)',1,[]));

%%%%%%%%%%%%%%%%%%%%%%%%%%%%%%%%%% CRITICAL UMD
xvec=1:5000;
%%%%%%%%%%%%%%%%%%%%%%%%%%%%%%%%%%upper limit
geolct3a=zeros(1,5000);geolct3b=zeros(1,5000);geolct3c=zeros(1,5000);
geolct3d=zeros(1,5000);geolct3e=zeros(1,5000);geolct3f=zeros(1,5000);
geolct3g=zeros(1,5000);

p=srval(1); geolct3a(xvec < p)=geolct3a(xvec < p)+1;
p=newp(rrval,p);geolct3b(xvec < p)=geolct3b(xvec < p)+1;
p=newp(slval,p);geolct3c(xvec < p)=geolct3c(xvec < p)+1;
```

```
411 p=newp(ovval,p);geolct3d(xvec < p)=geolct3d(xvec < p)+1;
412 p=newp(tfval,p);geolct3e(xvec < p)=geolct3e(xvec < p)+1;
413 if ~isempty(gmaval);p=newp(gmaval,p);geolct3f(xvec < p)=geolct3f(xvec < p)+1;
       end
414 if ~isempty(ptval);p=newp(ptval,p);geolct3g(xvec < p)=geolct3g(xvec < p)+1;end
415 geolct3=geolct3a;
416 if any(geolct3b>0);geolct3=geolct3.*geolct3b;end
417 if any(geolct3c>0);geolct3=geolct3.*geolct3c;end
418 if any(geolct3d>0);geolct3=geolct3.*geolct3d;end
419 if any(geolct3e>0);geolct3=geolct3.*geolct3e;end
420 if any(geolct3f>0);geolct3=geolct3.*geolct3f;end
421 if any(geolct3g>0);geolct3=geolct3.*geolct3g;end
422
423 geolct3=geolct3./max(geolct3);
424
425 maxall=max([srval rrval slval ovval tfval gmaval ptval]);
426 minall=min([srval rrval slval ovval tfval gmaval ptval]);
427 elemval={srval;rrval;slval;ovval; tfval; gmaval;ptval};
428 cricUL=round(p);
429
430
431 nsubp=handles.nsubp;
432 nind=handles.nind;
433
434 hfig4=figure(1);
435 set(hfig4,'units','normalized','outerposition',[0 0 0.5 1]);
436 plotsub=['a';' ';'b';' ';'c';' ';'d';' ';'e';' ';'f';' ';'g';' ';...
437     'h';' ';'i';' ';'j';' ';'k';' ';'l';' ';'m';' ';'n';' ';...
438     'o';' ';'p';' ';'q';' ';'r';' ';'s';' ';'t';' ';'u';' ';'v'];
439
440 plotcnt=1;
441 if (nind(1) ==1)
442 subplot(nsubp,2,plotcnt)
```

```
443 plotprob(geolct3a,minall,maxall,[ '(' plotsub(plotcnt,:) ') Source Rock: First
        Block']);
444 plotcnt=plotcnt+2;
445 end
446
447 if (nind(2) ==1)
448 subplot(nsubp,2,plotcnt)
449 plotprob(geolct3b,minall,maxall,[ '(' plotsub(plotcnt,:) ') Reservoir Rock:
       First Block']);
450 plotcnt=plotcnt+2;
451 end
452
453 if (nind(3) ==1)
454 subplot(nsubp,2,plotcnt)
455 plotprob(geolct3c,minall,maxall,[ '(' plotsub(plotcnt,:) ') Seal Rock: First
       Block']);
456 plotcnt=plotcnt+2;
457 end
458
459 if (nind(4) ==1)
460 subplot(nsubp,2,plotcnt)
461 plotprob(geolct3d,minall,maxall,[ '(' plotsub(plotcnt,:) ') Overburden: First
       Block']);
462 ylabel('Probability', 'Fontsize',25,'Color','k');
463 plotcnt=plotcnt+2;
464 end
465
466 if (nind(5) ==1)
467 subplot(nsubp,2,plotcnt)
468 plotprob(geolct3e,minall,maxall,[ '(' plotsub(plotcnt,:) ') Trap Formation:
       First Block']);
469 plotcnt=plotcnt+2;
470 end
```

```
471
472 if (nind(6) ==1)
473 subplot(nsubp,2,plotcnt)
474 plotprob(geolct3f,minall,maxall,[ '(' plotsub(plotcnt,:) ') GMA: First Block'
    ]);
475 plotcnt=plotcnt+2;
476 end
477
478 if (nind(7) ==1)
479 subplot(nsubp,2,plotcnt)
480 plotprob(geolct3g,minall,maxall, [ '(' plotsub(plotcnt,:) ') Preservation:
    First Block']);hold on;
481 plotcnt=plotcnt+2;
482 end
483
484
485 subplot(nsubp,2,plotcnt)
486 plotprob(geolct3,minall,maxall,[ '(' plotsub(plotcnt,:) ') Product of
    Probabilities: First Block']);hold on;
487 plot(cricUL,max(geolct3),'ks','Markersize',22,'MarkerFacecolor','k');
488 xlabel('Time (m.y.)', 'Fontsize',25,'Color','k');
489 set(gca,'Xaxislocation','bottom');grid on;grid minor;
490
491 box on;
492
493
494 %%%%%%%%%%%%%%%%%%%%%%lower limit
495
496 %%Best Estimate
497 %%%%%%%%%%%%%%%%%%%%%%%%%%%%criticalmoment
498 %%soucerock and overburden
499 geolct1=zeros(1,5000);
500 %find total length of overburden rock
```

```
lenov=0;for jj=1:2:nov*2;lenov=lenov +(ovval(jj)-ovval(jj+1)); end
%%find section length above source rock and divide
for kk=1:2:nsr*2
lenab=0;
for jj=1:2:nov*2
if (ovval(jj+1) < srval(kk)) && (ovval(jj) <= srval(kk+1))
lenab=lenab + ( ovval(jj)-ovval(jj+1) );
elseif (ovval(jj+1) < srval(kk)) && (ovval(jj) > srval(kk+1))
lenab=lenab + ( srval(kk+1)-ovval(jj+1) );
end
end
factr=lenab/lenov;
ind=(xvec < ovval(jj) & xvec < srval(kk) );
geolct1(ind)=geolct1(ind)+factr;
end

%%%ReservoirRock and Seal and Trap
geolct2=zeros(1,5000);
for jj=1:2:nrr*2
  for kk=1:2:nsl
   ind=(xvec <= slval(kk)  & xvec <= rrval(jj) & xvec <= cricUL );
   geolct2(ind)=geolct2(ind)+(1./nsl);
  end
  for kk=1:2:ntf
   ind=(xvec <= tfval(kk)  & xvec <= rrval(jj) & xvec <= cricUL );
   geolct2(ind)=geolct2(ind)+(1./ntf);
  end

end
geolct1=geolct1./max(geolct1);geolct2=geolct2./max(geolct2);
geolct=geolct1.*geolct2;
geolct=geolct./max(geolct);

```

```
pos=find(geolct==max(geolct),1,'last');
cricM=round(pos);

%%%%%%%%%%%%%%%%%%%%%%%%%%%%%%%%%%%%%%%%%%%%%%%%%%%%%%%%%%%%%%%%%%%%%%%%%%%%

%%source rock conditions
geoltimesr=zeros(1,5000);
%%Does time point fall after the initial source rock deposition.
%%Are there other younger source rock depositions?
%%assign score for time line after sr deposition
%%additional score for points after each new younger sr
if ~isnan(srval);if ~isempty(srval)
for jj=1:2:nsr*2
    ind=(xvec <= srval(jj));
geoltimesr(ind)=geoltimesr(ind)+1;
end
geoltimesr=geoltimesr./max(geoltimesr);
end;end


%%reservoir rock conditions
geoltimerr=zeros(1,5000);
%%Presence of reservoir rock
if ~isnan(rrval);if ~isempty(rrval)
for jj=1:2:nrr*2
    ind=(xvec <= rrval(jj));
geoltimerr(ind)=geoltimerr(ind)+1;
end
geoltimerr=geoltimerr./max(geoltimerr);
end;end

if isempty(srval) || isempty(rrval)
       disp('No Source Rock or No Reservoir Rock: No Petroleum System')
```

```
567 else
568
569
570 %%seal rock conditions
571 %%time younger than seal rock counts
572 geoltimesl=zeros(1,5000);
573 if ~isnan(slval);if ~isempty(slval)
574 for jj=1:2:nsl*2
575     ind=(xvec <= slval(jj));
576 geoltimesl(ind)=geoltimesl(ind)+1;
577 end
578 geoltimesl=geoltimesl./max(geoltimesl);
579 end;end
580
581
582 %%overburden rock conditions
583 geoltimeov=zeros(1,5000);
584 if ~isnan(ovval);if ~isempty(ovval)
585 for jj=1:2:nov*2
586 ind=(xvec <= ovval(jj));
587 geoltimeov(ind)=geoltimeov(ind)+1;
588 end
589 geoltimeov=geoltimeov./max(geoltimeov);
590 end;end
591
592
593
594 %%trap formation conditions
595 geoltimetf=zeros(1,5000);
596 if ~isnan(tfval);if ~isempty(tfval)
597 for jj=1:2:ntf*2
598 ind=(xvec <= tfval(jj));
599 geoltimetf(ind)=geoltimetf(ind)+1;
```

```
end
geoltimetf=geoltimetf./max(geoltimetf);
end;end


%%gma conditions
geoltimegma=zeros(1,5000);
if ~isnan(gmaval);if ~isempty(gmaval)
for jj=1:2:ngma*2
ind=(xvec <= gmaval(jj));
geoltimegma(ind)=geoltimegma(ind)+1;
end
geoltimegma=geoltimegma./max(geoltimegma);
end;end


%%preservation conditions
geoltimept=zeros(1,5000);
if ~isnan(ptval);if ~isempty(ptval)
for jj=1:2:npt*2
ind=(xvec <= ptval(jj));
geoltimept(ind)=geoltimept(ind)+1;
%begining of preservation time
ind=round(ptval(1));
geoltimept(ind)=geoltimept(ind)+1;
end
geoltimept=geoltimept./max(geoltimept);
end;end


%%%sum all together and normalize
%%%geoltime=geoltimesr+geoltimerr+geoltimesl+geoltimeov+geoltimetf+geoltimegma
   +geoltimept;
```

```
geoltime=geoltimesr;
if any(geoltimerr>0); geoltime=geoltime.*geoltimerr; end
if any(geoltimesl>0); geoltime=geoltime.*geoltimesl; end
if any(geoltimeov>0); geoltime=geoltime.*geoltimeov; end
if any(geoltimetf>0); geoltime=geoltime.*geoltimetf; end
if any(geoltimegma>0); geoltime=geoltime.*geoltimegma; end
if any(geoltimept>0); geoltime=geoltime.*geoltimept; end
geoltime=geoltime./max(geoltime);

pgeoltime=geoltimesr+geoltimerr+geoltimesl+geoltimeov+geoltimetf+geoltimegma+
    geoltimegma;
pgeoltime=pgeoltime./max(pgeoltime);
p=find(geoltime==max(geoltime),1,'last');
cricD=round(p);

geolnextlev=max(geoltime(xvec > cricM));
pUP=find(geoltime==geolnextlev,1,'last');
cricUP=round(pUP);if (cricUP > cricUL); cricUP=cricUL;end

geolnextlev=geoltime(xvec==cricUP);
%%%%%%%%%%
%%uncertainty
if (cricUP == cricD)
geolnextlev=max(pgeoltime(xvec > cricM));
uncUP=find(pgeoltime==geolnextlev,1,'last');
uncertainty=0.5*(uncUP-cricUP);
else
uncertainty=0.5*(cricUP-cricD);
end

hfig2=figure(1);
set(hfig2,'units','normalized','outerposition',[0 0 0.5 1]);
oldplotcnt=plotcnt;
```

```
plotcnt=2;
if (nind(1) ==1)
subplot(nsubp,2,plotcnt)
plotprob(geoltimesr,minall,maxall,[ '(' plotsub(oldplotcnt+plotcnt,:) ')
    Source Rock: All Blocks']);
plotcnt=plotcnt+2;
end

if (nind(2) ==1)
subplot(nsubp,2,plotcnt)
plotprob(geoltimerr,minall, maxall,[ '(' plotsub(oldplotcnt+plotcnt,:) ')
    Reservoir Rock: All Blocks']);
plotcnt=plotcnt+2;
end

if (nind(3) ==1)
subplot(nsubp,2,plotcnt)
plotprob(geoltimesl,minall,maxall,[ '(' plotsub(oldplotcnt+plotcnt,:) ') Seal
    Rock: All Blocks']);
plotcnt=plotcnt+2;
end

if (nind(4) ==1)
subplot(nsubp,2,plotcnt)
plotprob(geoltimeov,minall,maxall,[ '(' plotsub(oldplotcnt+plotcnt,:) ')
    Overburden: All Blocks']);
ylabel('Probability', 'Fontsize',25,'Color','k');
plotcnt=plotcnt+2;
end

if (nind(5) ==1)
subplot(nsubp,2,plotcnt)
plotprob(geoltimetf,minall,maxall,[ '(' plotsub(oldplotcnt+plotcnt,:) ') Trap
```

```
    Formation: All Blocks']);
plotcnt=plotcnt+2;
end

if (nind(6) ==1)
subplot(nsubp,2,plotcnt)
plotprob(geoltimegma,minall,maxall,[ '(' plotsub(oldplotcnt+plotcnt,:) ') GMA:
    All Blocks']);
plot(uncUP,1,'bv','Markersize',20,'MarkerFaceColor','b')
plotcnt=plotcnt+2;
end

if (nind(7) ==1)
subplot(nsubp,2,plotcnt)
plotprob(geoltimept,minall,maxall,[ '(' plotsub(oldplotcnt+plotcnt,:) ')
    Preservation: All Blocks']);
plotcnt=plotcnt+2;
end

subplot(nsubp,2,plotcnt)
plotprob(geoltime,minall,maxall,[ '(' plotsub(oldplotcnt+plotcnt,:) ') Product
    of Probabilities: All Blocks']);

hold on;
plot(cricUP,geolnextlev,'b^','Markersize',20,'MarkerFacecolor','b');
 plot(cricD,max(geoltime),'ro','Markersize',14,'MarkerFacecolor','r');
xlabel('Time (m.y.)', 'Fontsize',25,'Color','k');
set(gca,'Xaxislocation','bottom');grid on;
 end
box on;

if (isfield(handles,'saveFlag') && handles.saveFlag==1)
saveas(hfig2, handles.saveName1,'fig');
```

```
722 saveas(hfig2, handles.saveName2,'png');
723 close(hfig2);
724 end
725
726 hfig3=figure(3);
727 set(hfig3,'units','normalized','outerposition',[0 0 0.5 1]);
728 subplot(3,1,1)
729 plotprob(geolct1,minall,maxall,'(a) Probability of Generation and Migration');
730 subplot(3,1,2)
731 plotprob(geolct2,minall, maxall,'(b) Probability of Accumulation')
732 ylabel('Probability', 'Fontsize',25,'Color','k')
733 subplot(3,1,3)
734 plotprob(geolct,minall, maxall,'(c) Product of Probabilities')
735 hold on;
736  plot(cricM,max(geolct),'gh','Markersize',18,'MarkerFacecolor',[0    0.3906
          0]);
737  xlabel('Time (m.y.)', 'Fontsize',25,'Color','k');
738  set(gca,'Xaxislocation','bottom');grid on;
739  box on;
740
741 if (isfield(handles,'saveFlag') && handles.saveFlag==1)
742 saveas(hfig3, handles.saveName3,'fig');
743 saveas(hfig3, handles.saveName4,'png');
744 close(hfig3);
745 end
746
747
748 % --------------------------------------------------------------------
749
750 function p=newp(new,p)
751 nn=length(new);
752 fp_new=[];
753 for jj=2:2:nn
```

```
754 if ( new(jj) <= p  ); fp_new=[ new(jj-1) new(jj) ];break; end
755 %%%%first_participating influence from higher block
756
757 end
758 if (~isempty(fp_new) );  p=fp_new(1); end  %%influence from upper block
759 %%%if (~isempty(fp_new) && fp_new(1) < p);  p=fp_new(1); end
760
761 % ------------------------------------------------------------------------
762
763 function col=plotscale(levelss,ncol,minall,maxall)
764 col=simple_separate_colors(ncol*2);count=1;
765 for kk=4:-1:1
766 levelcell=table2cell(levelss{kk});[n,~]=size(levelcell);
767 st=min([ levelcell{:,3}]);
768 for jj=1:n
769     len=levelcell{jj,4}-levelcell{jj,3};
770     if (kk ==1)
771     yst=kk-2;
772      xx=[st st+len st+len st];yy=[yst+1 yst+1 yst+1+0.5 yst+1+0.5 ];
773      hpat=patch(xx,yy,col(count,:),'FaceAlpha',0.6);
774     txpos=st+len/1.8;
775     if (txpos <= maxall && txpos > (minall+5))
776     h=text(txpos,(yst+1.2),levelcell{jj,2},'Fontsize',20,'Fontweight','bold','
    Color','k');
777     %set(h,'Rotation',270);
778     end
779     else
780     yst=kk-2;
781     xx=[st st+len st+len st];yy=[yst yst yst+1 yst+1];
782     hpat=patch(xx,yy,col(count,:),'FaceAlpha',1);
783     txpos=st+len/1.8;
784     if (txpos <= maxall && txpos > (minall+10) )
785     h=text(txpos,(yst+0.6),levelcell{jj,1},'Fontsize',20,'Fontweight','bold','
```

```
    Color','k');
786     %set(h,'Rotation',270);
787     end
788     end
789     count=count+1;
790     hold on
791
792     st=st+len;
793
794 end
795 clear levelcell;
796 end
797 ylim([-10 3]);xlim([minall maxall+5]);
798 set(gca,'Xdir','reverse','Xaxislocation','top','XColor','k','YColor','k','
    Fontsize',35);
799
800
801 % ------------------------------------------------------------------------
802
803
804 function col=simple_separate_colors(n)
805   col = zeros(n,3);
806 x=linspace(0.1,0.9,30);[X,Y,Z]=meshgrid(x,x,x);col_large_rgb=[X(:),Y(:),Z(:)];
807 C = makecform('srgb2lab');col_large_lab = applycform(col_large_rgb,C);
808 benchmarkcol = applycform([1 0 0],C);prevcol = benchmarkcol(end,:); gap = inf(
    size(col_large_rgb,1),1);
809 for k = 1:n
810     eulerd=sqrt(sum((col_large_lab-repmat(prevcol,[size(col_large_lab,1) 1]))
    .^2,2));
811     gap = min(eulerd,gap);[~,ind] = max(gap);
812     prevcol = col_large_lab(ind,:); col(k,:) = col_large_rgb(ind,:);
813 end
814
```

```
% --------------------------------------------------------------------

function plotprob(geoltm,minall,maxall,titl)
plot(geoltm,'Linewidth',3);xlim([minall maxall]);
set(gca,'Xdir','reverse','Xaxislocation','top');grid on;grid minor;
set(gca,'Fontsize',18,'XColor','k','YColor','k')
t=title(titl,'Color','k');

%right align
% set(t, 'horizontalAlignment', 'right');
% set(t, 'units', 'normalized')
% h1 = get(t, 'position');
% set(t, 'position', [1 h1(2) h1(3)])
hold on
% --------------------------------------------------------------------


% --- Executes during object creation, after setting all properties.
function uipanel1_CreateFcn(hObject, eventdata, handles)
% hObject    handle to uipanel1 (see GCBO)
% eventdata  reserved - to be defined in a future version of MATLAB
% handles    empty - handles not created until after all CreateFcns called


% --- Executes during object creation, after setting all properties.
function uibuttongroup1_CreateFcn(hObject, eventdata, handles)
% hObject    handle to uibuttongroup1 (see GCBO)
% eventdata  reserved - to be defined in a future version of MATLAB
% handles    empty - handles not created until after all CreateFcns called


% --- Executes on button press in radiobutton6.
function radiobutton6_Callback(hObject, eventdata, handles)
```

```
% hObject    handle to radiobutton6 (see GCBO)
% eventdata  reserved - to be defined in a future version of MATLAB
% handles    structure with handles and user data (see GUIDATA)

% Hint: get(hObject,'Value') returns toggle state of radiobutton6

% --- Executes on button press in pushbutton5.
function pushbutton5_Callback(hObject, eventdata, handles)
% hObject    handle to pushbutton5 (see GCBO)
% eventdata  reserved - to be defined in a future version of MATLAB
% handles    structure with handles and user data (see GUIDATA)
close(gcbf);
close all;
QPFA;
clear all; clc;

% --- Executes on button press in pushbutton6.
function pushbutton6_Callback(hObject, eventdata, handles)
% hObject    handle to pushbutton6 (see GCBO)
% eventdata  reserved - to be defined in a future version of MATLAB
% handles    structure with handles and user data (see GUIDATA)
close(gcbf);

% --- Executes during object creation, after setting all properties.
function text4_CreateFcn(hObject, eventdata, handles)
% hObject    handle to text4 (see GCBO)
% eventdata  reserved - to be defined in a future version of MATLAB
% handles    empty - handles not created until after all CreateFcns called
```